UAB
Universitat Autònoma de Barcelona

UNIVERSITAT AUTÒNOMA DE BARCELONA
DEPARTAMENT DE FÍSICA

UAB
Universitat Autònoma de Barcelona

DOCTORAL THESIS

Search for transient events and pulsars in multi-frequency data

---

Author:
Abubakr Y. A. Ibrahim

Advisors:
Prof. Nanda Rea
Dr. Francesco Coti Zelati

Tutor:
Prof. Lluís Font Guiteras

A thesis submitted for the degree of
Doctor of Philosophy in Physics

Barcelona, September 2024

Declaration of Authorship

I, Abubakr Y. A. Ibrahim, declare that this thesis titled, "Search for transient events and pulsars in multi-frequency data" and the work presented in it are my own. I confirm that:

Abstract

The study of neutron stars, particularly magnetars, is crucial for understanding the extreme conditions in the Universe. This thesis focuses on multi-wavelength observations of these highly magnetized neutron stars, examining both their outburst activities and the search for pulsars and transient events across various bands, including X-ray and radio.

This thesis includes an analysis of the first outburst of the young magnetar Swift J1818.0-1607, using data from XMM-Newton, NuSTAR, and Swift. The results shows a decreasing trend in the emitting region size and significant torque variability over time. Additionally, we identify diffuse X-ray and radio emissions suggesting possible associations with a dust-scattering halo and a supernova remnant, respectively.

We also studied the 2022 reactivation of the magnetar SGR J1935+2154 using X-ray observations from the XMM-Newton and NuSTAR telescopes. Our findings show consistent thermal properties with small variations in the non-thermal component, along with an increased spin-period rate, suggesting possible changes in the magnetosphere or the relativistic wind during the outburst. These studies contribute to our understanding of the thermal emission on the stellar surface and the role of magnetospheric processes during magnetar outbursts events.

In addition, we analyzed radio archival observations of the magnetic isolated white dwarf ZTF J1901+1458, in search for possible dipolar emission and pair acceleration from this source. We derived deep upper limits that will help somehow constraining the nature of the recently discovered long-period transients.

Moreover, we developed the eBANDERAS pipeline, an automated and systematic tool aimed at detecting and analysing X-ray transients and periodic or aperiodic sources in X-ray surveys. The pipeline is mission-independent, allowing for adaptability across different X-ray missions, including the recent eROSITA mission. In this work, we focused in the development of the transient search component, which includes studying the EXTraS transient tools and updating the X-ray transients events using the most recent XMM-Newton catalog.

This work not only contributes to our understanding of neutron star outbursts but also lays a solid foundation by building tools for detecting new transient sources in current and future X-ray surveys, significantly advancing the field of high-energy astrophysics.

0.1 List of Publication

- Ibrahim et al. (2023)
  "Deep X-Ray and Radio Observations of the First Outburst of the Young Magnetar Swift J1818.0-1607"
  Published In: ApJ 943.1, 20, p. 20. DOI:10.3847/1538-4357/aca528. arXiv: 2211.12391 [astro-ph.HE].

- Ibrahim et al. (2024)
  "An X-Ray and Radio View of the 2022 Reactivation of the Magnetar SGR J1935+2154"
  Published In: ApJ 965.1, 87, p. 87. DOI: 10.3847/1538-4357/ad293b. arXiv: 2402.08596 [astro-ph.HE].

- "Searching for an isolated magnetic white dwarf pulsar ZTF J1901+1458"
  Work in Progress
  Contributors:
  A. Y. Ibrahim⊙, Natasha Hurley-Walker⊙, N. Rea⊙, P. A. Woudt⊙

- "eBANDERAS: Pulsar and Transient Search Pipeline"
  Contributors:
  A. Marino⊙, A. Y. Ibrahim⊙, E. Parent⊙, F. Coti Zelati⊙, G. L. Israel⊙, M. Imbrogno⊙, N. Rea⊙

Acknowledgements

First and foremost, I want to express my deepest thanks to my supervisors, Nanda and Francesco. Nanda, your unwavering support, positivity, and understanding have meant the world to me. Your ability to make me feel comfortable while keeping me motivated has been truly invaluable. You've created an environment where I could thrive, both personally and professionally, allowing me to contribute to this amazing project. Francesco, your smooth guidance and expertise have been the backbone of this thesis. I couldn't have asked for better mentors—or for more last-minute deadlines.

I also want to extend a very special thanks to Alice Borghese, who, in every sense but officially, has been my supervisor. Alice, your guidance throughout my phd journey has been invaluable. You've been a constant source of knowledge and support. I truly consider you an essential part of this thesis, and I am deeply grateful for all the time and effort you've invested in my work.

To the entire MAGNESIA group, you've been my second family. A special mention goes to my subgroup, "The observers"—Rajath, Alessio, and Emilie (our master of pulsar timing)—thank you for your great contribution and endless efforts for being by my side through it all. Clara, my Arabic-speaking One to have a lovely chat with, thank you for hosting countless events and for making Ramadan and Eid feel like home. Daniele, I'll never forget you were the first to welcome me to Barcelona (truly time flies so fast). Stefano, our chats about deep concepts in open topics have been some of the best parts of this journey. Davide, for your kindness and nice accompany. Vanessa, your professionalism and kindness have been inspiring, in all aspects. Celsa, our Spanish queen, you've added a regal touch to the group. Michele, my golden companion, officemate, apartment mate, covid-mate! I can't imagine this journey without you. You've been my go-to One for everything, and you always available, thank you for making it all a little less daunting. I would also like to extend my thanks to Konstantinos and Thomas for sharing the good moments.

Now, to the honorable members of the CHAIR next to my desk, occupied by some truly remarkable individuals: Christine, Arianna, Anna, Giulia, and Simona (even if only for a couple of days). I'm still wondering why I didn't draft contracts to keep you all from leaving! This list also include Matteo (although you were not far from that chair), thank you for all the good times, both in Rome and Barcelona (and more other places), and for being an amazing collaborator on the eROSITA project. To all my PhD colleagues, you've shared in the challenges, joys, Seminars, and the coffee/pizza breaks. Thank you for being an integral part of this experience. Arghavan, I'll sorely miss our Iranian tea sessions, but rest assured, you'll always have a special place in my memories (and my pantry). To all my flatmates, past and present—Simran, your support on the radio project and your kind, beautiful spirit have meant so much to me. A heartfelt thanks to my PhD defense committee for their time, effort, and insightful feedback. I'm honored to have you evaluate my work. Lastly, to my family—your unconditional love and support have been my anchor through it all. I owe everything to you.

Here's to the end of one chapter and the beginning of the next. Thank you all for being a part of this journey.

Contents

Physical Constants

Speed of light in a vacuum	$c = 2.99792458 \times 10^{10}\ \mathrm{cm\,s^{-1}}$
Gravitational constant	$G = 6.67259 \times 10^{-8}\ \mathrm{cm^3\,g^{-1}\,s^{-2}}$
Planck constant	$h = 6.6260755 \times 10^{-27}\ \mathrm{erg\,s}$
Electron charge	$e = 4.8032068 \times 10^{-10}\ \mathrm{esu}$
Electron mass	$m_e = 9.1093897 \times 10^{-28}\ \mathrm{g}$
Proton mass	$m_p = 1.6726231 \times 10^{-24}\ \mathrm{g}$
Neutron mass	$m_n = 1.6749286 \times 10^{-24}\ \mathrm{g}$
Boltzmann constant	$k_{\mathrm{B}} = 1.380658 \times 10^{-16}\ \mathrm{erg\,K^{-1}}$
Solar mass	$M_\odot = 1.989 \times 10^{33}\ \mathrm{g}$
Parsec	$pc = 3.0856 \times 10^{18}\ \mathrm{cm}$
Jansky	$Jy = 1.0 \times 10^{-23}\ \mathrm{erg\,cm^{-2}\,s^{-1}Hz^{-1}}$
Year	$yr = 3.1557 \times 10^{7}\ \mathrm{s}$

1 Neutron stars and their properties

1.1 Historical context and discovery of the first pulsar

The concept of neutron stars, dense remnants of a supernova explosion, was theoretically predicted before their observational confirmation. The groundwork was laid by Chandrasekhar in 1930, who established a maximum mass limit for white dwarfs, now known as the Chandrasekhar limit ($\sim 1.4\ M_\odot$, Chandrasekhar, 1931). This concept suggested that stars exceeding this limit might collapse into an even denser objects, pointing towards the existence of neutron stars.

The neutron's discovery in 1932, Chadwick, 1932 further supports the theoretical framework required for the concept of neutron stars. However, the actual existence of neutron stars was first proposed by astronomers Walter Baade and Fritz Zwicky in 1934 (Baade and Zwicky, 1934), who theorised that these could be the end product of supernova explosions.

Despite these early theoretical insights, the first observational evidence of neutron stars came with the discovery of pulsars in 1967 by Ph.D. student Jocelyn Bell Burnell at Mullard Radio Astronomy Observatory, which was initially designed to study quasars. During her observation, she detected unusually regular periodic signals emitting a pulse every 1.33 seconds. The initial interpretation suggested that these periodic signals likely resulted from oscillating compact objects, particularly white dwarfs or neutron stars within our Galaxy (Hewish et al., 1968). Further analysis, including measurements of spin period and spin-down, determined that these pulses originated from a rapidly rotating neutron star. The spin-down was consistent with what is expected from a rotating object losing rotational kinetic energy, rather than what would be expected from a vibrating object, marking the first-ever observation of a pulsar. This discovery was significant as it provided the first evidence of neutron stars' existence and opened new avenues in high-energy astrophysics and the study of cosmic phenomena. Following the discovery of pulsars, Pacini, 1968 and Gold, 1968 independently proposed models that connected newly discovered pulsating sources to neutron stars. Their studies suggested that the potential for rotating neutron stars to emit observable coherent emission is due to their strong magnetic fields. These fields accelerate charged particles to relativistic speeds, thereby emitting radiation detectable as pulses. These sources are referred to as pulsars, an acronym for pulsating stars. In late 1968, around 20 sources with similar properties were identified including pulsating radio source in the Crab nebula, the famous supernova remnant observed by the Chinese in AD 1054 (Staelin and Reifenstein, 1968; Comella et al., 1969); and one with a period of 89 ms in the Vela supernova remnant (Large, Vaughan, and Mills, 1968).

In the landmark study by Richards and Comella, 1969, the identification of pulsars as rotating neutron stars was convincingly supported by the measured spin-down phenomenon observed in the Crab pulsar, validating the theoretical models

proposed by Pacini and Gold, identifying pulsars as rotating neutron stars undergoing dynamic evolutionary processes. Additionally, the identification of the Vela and Crab pulsars within supernova remnants supported the initial hypothesis proposed by Baade and Zwicky.

Since the first detection of pulsars, approximately 3500 pulsars have been discovered, spanning a wide range of wavelengths from radio to gamma-rays, and including sources either isolated or in binary systems (Manchester et al., 2005). With the current and future advanced instruments such as the Square Kilometre Array (SKA[1]) in the radio band and the extended ROentgen Survey with an Image Telescope Array (*eROSITA*) and Cherenkov Telescope Array (CTA[2]) in X-ray and gamma-ray, respectively, the number of known neutron stars is expected to grow considerably.

In this chapter, we will cover the following key areas: (highlight the different Sections of this chapter)

1.1.1   The Neutron Star Zoo

In recent decades, progresses in telescope capabilities and multiwavelength observing campaigns have revealed a remarkable diversity in the evolution and properties of neutron stars, often referred to as the "neutron stars zoo". These diverse characteristics have led to the classification of neutron stars into various groups based on their primary energy sources. These are:

- *Rotation:* Energy emission in rotation-powered neutron stars arises from the rotation of their electromagnetic dipole, which causes the neutron star to gradually slow down. These neutron stars can be detected as pulsars or through the radiation generated by the interaction of a relativistic particle wind from the neutron star with a surrounding nebula. Additionally, they can exist both as isolated objects or within binary systems.

- *Accretion:* Emission from accretion-powered neutron stars results from the release of gravitational binding energy as material from a companion star impacts the neutron star's surface. All accretion-powered neutron stars are found in binary systems.

- *Magnetic Energy:* Magnetic-powered neutron stars exhibit X-ray luminosities that generally exceed what could be powered by rotational energy alone, and no evidence of accretion is observed. Based on the magnetar model, their emission is driven by the instability and decay of their extraordinary strong magnetic field ($B \gtrsim 10^{14}$ G). Magnetars are bright X-ray sources, and are characterized by transient activities such as outbursts and short bursts due to their magnetic field evolution (more details in Sec 1.2).

- *Cooling:* Thermally-powered neutron stars store their energy as internal heat, which can either be resulted to either residual heat from the neutron star formation (observable for the first $\sim 10^5$ years) or to surface reheating by an external source such as returning currents in the magnetosphere. Additionally, strong magnetic field can also provide a source of heat via Joule dissipation of the electrical currents circulating in the neutron star crust, thereby powering thermal emission.

---

[1]SKAO:
https://www.skao.int/en
[2]CTA:
https://www.ctao.org/

The different mechanisms of energy emission give rise to various categories of neutron stars, with rotation and accretion power, as well as magnetic and thermal emission, being the primary channels that make these otherwise faint objects observable. These include not only rotation-/accretion-powered neutron stars, but also magnetars and thermally-emitting X-ray Dim Isolated Neutron Stars (XDINSs). For a recent review on different classes of isolated neutron stars, see Borghese and Esposito ([2023]).

A valuable tool for understanding the diversity of neutron star is the $P\dot{P}$ diagram, which shows the spin period (P, the time taken for neutron star to complete one rotation) against its derivative ($\dot{P}$, the rate at which the spin period changes over time, indicating the rate of slow down). This diagram helps classify neutron stars based on their spin properties and provides estimates of their surface dipole magnetic-field strengths.

Figure [1.1] shows the observed population of non-accreting neutron stars in the $P\dot{P}$ diagram. This figure includes the latest data (as of July 2024) from the Australia Telescope National Facility (ATNF) pulsar catalogue (VERSION: 2.2.0; Manchester et al., [2005]) and McGill[3] for pulsars and magnetars, respectively. The overlaid lines represent the spin-down luminosity (dotted line), magnetic fields (solid line), and characteristic age (dashed line) as derived from Equations [1.2], [1.4] and [1.6], respectively.

All rotation-powered neutron stars in the Galaxy are observed to spin down. Due to the loss of their rotational kinetic energy, they release energy at a rate given by:

$$|\dot{E}| = I\omega|\dot{\omega}| = 4\pi^2 I\dot{P}P^{-3}, \tag{1.1}$$

where $I = 0.4MR^2$ is the moment of inertia, $\omega = 2\pi/P$ is the angular frequency, P is the spin period, and $\dot{P} = dP/dt$ is its time derivative.

For neutron stars, we adopt the standard parameters: mass $M = 1.4M_\odot$ and radius $R = 10\,\text{km}$. Given measurements of P and $\dot{P}$, the energy budget available to power the emission, known as the spin-down luminosity, can be evaluated as:

$$|\dot{E}| = 4\pi^2 I\dot{P}P^{-3} \approx 4 \times 10^{33}\dot{P}_{13}P^{-3}\,\text{erg s}^{-1}, \tag{1.2}$$

where P is expressed in seconds and $\dot{P}_{13}$ is the spin period derivative in units of $10^{-13}\,\text{s s}^{-1}$.

According to the magnetic dipole model (Pacini, [1967]), a neutron star rotates in vacuum at an angular frequency ω and possesses a magnetic dipole moment μ oriented at an angle α with respect to the rotation axis. The magnetic dipole moment μ can be parameterized in terms of the dipole magnetic field at the equator B_{dip} as $|\mu| = B_{dip}R^3$. Due to the misalignment between the magnetic and rotational axes, this rotating magnetic dipole radiates energy at a rate given by the Larmor formula:

$$\dot{E}_{\text{dip}} = -\frac{2}{3c^3}|\ddot{\mu}|^2 = -\frac{2}{3c^3}\mu^2\omega^4(\sin\alpha)^2 = -\frac{1}{6c^3}B_{\text{dip}}^2R^6\omega^4(\sin\alpha)^2, \tag{1.3}$$

where $\ddot{\mu} = d^2\mu/dt^2$.

By assuming the rotational and magnetic axes are orthogonal ($\alpha = 90°$) and that magnetic dipole radiation is the dominant mechanism behind energy losses, the strength of the dipolar magnetic field at the magnetic equator can be estimated by

---

[3]See McGill Magnetar Catalog, Olausen and Kaspi ([2014])
https://www.physics.mcgill.ca/~pulsar/magnetar/main.html

equating the spin-down luminosity Eq. 1.2 and the magnetic dipole radiation Eq. 1.3:

$$B_{\mathrm{dip}} \approx \left(\frac{3c^3 I}{8\pi^2 R^6} \right)^{1/2} (P\dot{P})^{1/2} \approx 3.2 \times 10^{19} (P\dot{P})^{1/2}\,\mathrm{G}. \tag{1.4}$$

Assuming the initial spin period P_0 is much shorter than the current spin period and that the spin-down is primarily due to magnetic dipole radiation, we start with the general spin-down formula for a power-law deceleration model:

$$\dot{\nu} \propto \nu^n,$$

where $\nu = P^{-1}$ is the spin frequency and $n \propto \nu \ddot{\nu} \dot{\nu}^{-2}$ is the breaking index. By integrating the spin-down formula, we obtain the age of the neutron star:

$$\tau = \frac{P}{(n-1)\dot{P}} \left[1 - \left(\frac{P_0}{P} \right)^{n-1} \right]. \tag{1.5}$$

If we assume that the initial spin period P_0 is much shorter than the current spin period ($P_0 \ll P$), the term $\left(\frac{P_0}{P} \right)^{n-1}$ becomes negligible, and the age simplifies to:

$$\tau \approx \frac{P}{(n-1)\dot{P}}.$$

For pure magnetic dipole radiation, $n = 3$, the characteristic age τ_c is given by:

$$\tau_c = \frac{P}{2\dot{P}}. \tag{1.6}$$

It is important to note that τ_c generally represents an upper limit estimation and might not necessarily provide an accurate estimate of the true age of the neutron star due to various assumptions and simplifications.

In the following, I will briefly summarise the main observational properties of some of these classes:

Rotation Powered Pulsars (RPPs): located at the center of the $P\dot{P}$ diagram and represented by grey dots in Figure 1.1, these pulsars emit energy through the loss of rotational kinetic energy. This energy is converted into particle acceleration, producing broadband electromagnetic emission from radio to gamma-rays. RPPs can be both isolated or in binary systems. Young neutron stars, often associated with Supernova Remnants (SNRs, red stars) and detected as high-energy gamma-ray pulsars (purple squares), populate the upper part of the diagram. As they spin down and their magnetic fields decay over time, they move towards the bottom right region of the diagram. There are two main populations: "standard" pulsars with spin periods $P \gtrsim 0.1$ s and characteristic ages $\tau \lesssim 100$ Myr in the central region, and millisecond pulsars (MSPs) with spin periods down to a few milliseconds and higher characteristic ages $\tau \gtrsim 100$ Myr towards the bottom left. MSPs are older, often recycled neutron stars i.e., accelerated to fast spin periods following a prolonged phase of mass transfer from a companion star in a binary system. Additionally, Rotating Radio Transients (RRATs[4], cyan diamonds) are a

---

[4]RRATs:
https://rratalog.github.io/rratalog/

subpopulation characterized by sporadic, powerful radio bursts, suggesting they are standard pulsars with irregular emission (McLaughlin et al., 2006).

Central Compact Objects (CCOs[5]): shown as yellow triangles in the $P\dot{P}$ diagram (see; Figure 1.1), they are located near the centers of supernova remnants. They are characterized by their thermal X-ray emission and relatively low magnetic fields. CCOs are young neutron stars, with ages typically less than a few thousand years. Despite their youth, they exhibit low spin-down rates ($\sim \dot{P} = 10^{-18} - 10^{-17} s\, s^{-1}$). Three CCOs have measured $\dot{P}$ values: PSR J1852+0040 in Kes 79, PSR J0821$-$4300 in Puppis A, and 1E 1207.4$-$5209 in G296.5+10.0, leading to low inferred dipolar magnetic fields of order of 10^{10} to 10^{11} G under the dipole braking scenario. One explanation for this could be magnetic field burial during a fallback accretion episode post-supernova explosion. Notably, some CCOs exhibit X-ray pulsations at rotational periods of $\sim$ 100–400 ms, faster than those of XDINSs and magnetars. However, they generally do not exhibit significant variability. No radio emission has yet been observed from CCOs. The exact emission mechanisms of CCOs remain not fully understood, but they provide critical insights into early neutron star evolution and the aftermath of supernova explosions (De Luca, 2017).

X-ray Dim Isolated Neutron Stars (XDINSs): represented by orange triangles in the $P\dot{P}$ diagram (Figure 1.1), also known as the "Magnificent Seven" which are: RX J0420.0$-$5022, RX J0720.4$-$3125, RX J0806.4$-$4123, RX J1308.6+2127, RX J1605.3+3249, RX J1856.5$-$3754, and RX J2143.0+0654. These stars are isolated, meaning they lack a binary companion, and their thermal X-ray emission is thought to originate directly from the surface of the neutron star and is attributed to the residual internal heat since its formation. XDINSs have relatively long spin periods $\sim$ 3–11 s, and strong magnetic fields of the order of $\sim 10^{13}$ G, falling in the "high tail" of the magnetic-field values of typical pulsars. However, they are not detected in the radio band, which distinguish them from RPPs. They exhibit soft X-ray spectra well characterised by a blackbody model with a luminosity $L_X \lesssim 10^{31}$ erg s^{-1}. XDINSs are middle-aged neutron stars, with characteristic ages around 10^5 to 10^6 years, offering valuable insights into the cooling processes and internal composition of neutron stars (see; Turolla, 2009; Bogdanov and Ho, 2024).

1.2 Magnetars and their outbursts

Magnetars are a distinct class of young and isolated neutron stars characterised by their ultra-high magnetic fields of $B \approx 10^{14} - 10^{15}$ G. These magnetic fields are several order of magnitude stronger than those found in other classes of neutron stars, placing magnetars among the most magnetic objects in the Universe. This Section explores briefly the history of magnetars, the properties of their persistent emissions, and their transient activities, which include giant flares, short bursts, and outbursts. These phenomena provide critical insights into the extreme physical processes such as crustal deformations and magnetospheric interactions, which are responsible for their diverse spectra and timing properties.

---

[5]CCOs:
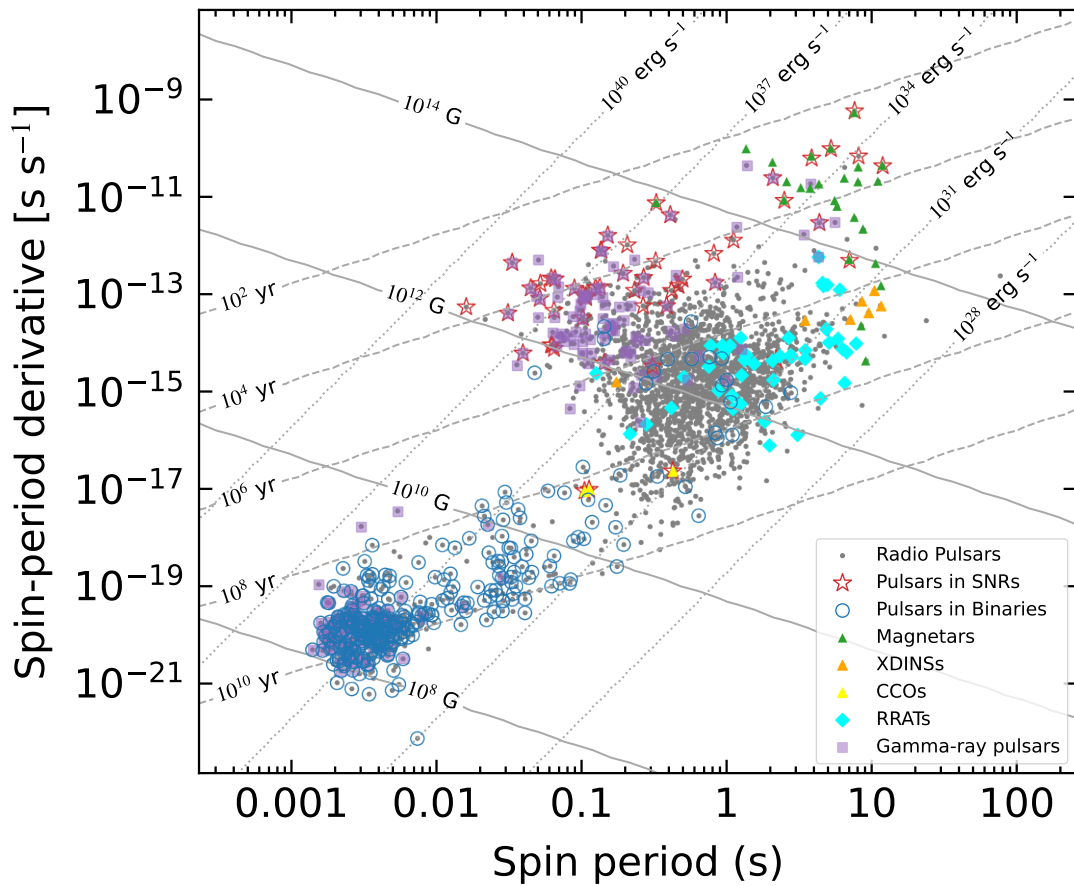https://www.iasf-milano.inaf.it/~deluca/cco/main.htm

FIGURE 1.1: $P\dot{P}$ diagram, showing known non-accreting pulsars. The diagram includes radio pulsars (grey dots), Rotating Radio Transients (RRATs, cyan diamonds), and gamma-ray pulsars (purple squares). The green, orange and yellow triangles represent magnetars, X-ray dim isolated neutron stars (XDINSs) and central compact objects (CCOs), respectively. Additional symbols indicate associations with supernova remnants (SNRs, red stars) and binary systems (blue circles). Overlaid lines represent characteristic age (dashed line), magnetic fields (solid line), and the spin-down luminosity (dotted line). This figure is adapted from (with permission; Ronchi, 2024), with modification to include updated data from the Australia Telescope National Facility (ATNF) pulsar catalogue (version: 2.2.0; Manchester et al., 2005), McGill magnetar catalogue, as well as additional plotting adjustments.

1.2.1 Introduction: a short history

The term "magnetar" was first introduced by Duncan and Thompson (1992), who suggested that the decay of extremely strong magnetic fields could be the primary energy source for the observed emission from these sources. Since the discovery of the first magnetar, SGR 0526−66, in 1979 (Mazets et al., 1979), the known magnetar population has grown to consist of about 30 confirmed sources (as of July 2024; Olausen and Kaspi, 2014). The study of magnetars has been extensively reviewed in the literature, with notable reviews by Turolla, Zane, and Watts (2015), Kaspi and Beloborodov (2017), Mereghetti, Pons, and Melatos (2015), Esposito, Rea, and Israel (2021), and Borghese and Esposito (2023).

Magnetars were initially classified into two different classes: Soft Gamma-ray Repeaters (SGRs) and Anomalous X-ray Pulsars (AXPs). The separation into these two classes reflects how these sources were originally discovered. SGRs were recognized via the detection of intense/repeated bursts in the hard X-rays and soft gamma-rays energy ranges (Mazets et al., 1979; Mazets et al., 1982). They were initially linked with GRBs, however, repeated bursts emission from SGRs led to distinguish them from GRBs. On the other hand, AXPs were discovered as persistent X-ray pulsars within the soft X-ray band i.e. bellow 10 keV (Mereghetti and Stella, 1995; van Paradijs, Taam, and van den Heuvel, 1995). The first discovery of AXPs was made by Fahlman and Gregory (1981), who identified 1E 2259+586 a 7 s X-ray pulsar in the supernova remnant G109.1−1.0. This source, along with other similar sources like 1E 1048.1−5937 and 4U 0142+614, were initially thought to be a subclass of low-mass X-ray binaries. However, the high X-ray luminosities exceeding the spin-down energy loss rate and the soft X-ray spectrum led to their classification as AXPs.

The theoretical framework for magnetars was strengthened by Thompson and Duncan, 1995; Thompson and Duncan, 1996, who demonstrated that the decay of a very strong magnetic field could explain the transient bursts, outbursts and the persistent emission seen in theses sources. This prediction was confirmed by the measurement of spin-down rates from the SGR sources 1806−20 and 1900+14 (Kouveliotou et al., 1998; Kouveliotou et al., 1999). These measurements provided strong confirmation of the magnetar model, with inferred magnetic field strengths of the order 10^{14}–10^{15} G.

1.2.2 Persistent Emission

Magnetars exhibit persistent emission predominantly in the X-ray band, characterised by distinct pulsation properties and pulse profile. All confirmed magnetars display pulsations in the soft X-ray band (below 10 keV), and with spin period of $\sim$ 1–12 s. A number of magnetars have also been detected in hard X-rays, with emission extending up to $\sim$100–200 keV. The pulse profile of magnetars can be modeled with one or multiple sinusoidal functions. These profiles are often energy-dependent and can change over time, particularly during periods of increased activity such as outbursts or strong bursting episodes (more details in Section 1.2.3).

The soft X-ray spectra (0.5–10 keV) of the persistent emission are typically composed of a thermal component that is well described by an absorbed blackbody with a temperature of $kT \sim$ 0.3–1 keV, often accompanied by a second component that can be either a blackbody with a higher temperature of $kT \sim$ 1–2 keV or a non-thermal power-law component with a photon index in the range of $\Gamma \sim 2-4$. At higher

energies, the non-thermal component tends to dominate the spectrum. The thermal component is believed to originate from the hot neutron star surface, while the non-thermal power-law tail likely arises from the magnetospheric processes such as resonant cyclotron scattering. In this model, soft seed photons emitted from the neutron star surface are boosted to higher energies through multiple scatterings with charged particles within a twisted magnetosphere, resulting in the formation of the aforementioned power-law tail (for more details see Turolla, Zane, and Watts, 2015, and reference therein). Observations have revealed that in addition to emitting soft X-rays, some magnetars can also emit hard X-rays up to $\sim$ 150–200 keV. This hard X-ray component, first observed with *INTEGRAL* and later confirmed with *Suzaku* and *NuSTAR*, is typically modeled by a power-law spectrum that is flatter than the soft X-ray component, with photon indices in the range of $\Gamma \sim 0.5 - 2$ (for a recent study, see Enoto et al., 2017).

Various mechanisms have been proposed for this hard X-ray emission, including bremsstrahlung emission, where photons are produced by the deceleration of charged particles in the neutron star's surface layers heated by returning currents; or synchrotron emission from pairs produced at a height of about 100 km above the neutron star surface (Thompson and Beloborodov, 2005). Additionally, a prominent model suggests that the hard X-ray emission is produced through the resonant Compton up-scattering of thermal seed photons by highly relativistic electrons in the magnetosphere. This process involves soft X-ray photons gaining energy through repeated interactions with these energetic particles, resulting in a harder spectral component (Baring and Harding, 2007; Wadiasingh et al., 2018).

Magnetars are predominantly observed in X-rays, but they also emit across other wavelengths, including optical, infrared (IR) and radio bands. Despite their faintness at optical and IR wavelengths and their location in heavily absorbed regions of the Galactic plane, counterparts have been identified for about two-third of known magnetars. These associations are particularly evident for sources exhibiting optical pulsations at the same period as their X-ray counterparts, such as 4U 0142+61, 1E 1048.1−5937 and SGR 0501+4516 (e.g. Dhillon et al., 2011).

Up to the time of writing this thesis, pulse radio emission has been detected from 6 out of total population of magnetars, typically following high-energy outbursts (Camilo et al., 2006; Camilo et al., 2007; CHIME/FRB Collaboration et al., 2020). Their radio emission is characterised by variability in both flux density and pulse profile shape, flat spectrum and high polarization, differing significantly from the typical radio emission of standard pulsars (more details about radio emission in the following Section 1.2.3).

1.2.3   Transient Activity

Magnetars show various types of transient activities observable from X-rays up to soft gamma-rays, primarily categorised into short bursts, giant flares and outbursts. These events can vary significantly in intensity, spectral evolution and duration, from brief milliseconds-long bursts to long-lived outbursts lasting weeks or even months/years.

1.2.3.1   Giant Flares

Giant flares are among the most energetic and rare phenomena associated with magnetars, only three events have been observed. In 1979 March 5, from SGR 0526−66 in the Large Magellanic Cloud (LMC, Mazets et al., 1979), on 1998 Augest 27 from

SGR 1900+14 Hurley et al., 1999 and on 2004 December 27 from SGR 1806−20 (Hurley et al., 2005; Palmer et al., 2005). These events are characterized by an initial short ($\sim$ 0.1–0.2 s) spike of soft gamma-rays, with emission extending up to a few MeVs. The peak luminosity of this events reaches up to $\gtrsim 10^{44}$–10^{45} erg s^{-1} ($\gtrsim 10^{47}$ erg s^{-1} for SGR 1806−20). Following the spike, the hard X-ray tails lasts for several minutes, showing a decay characterised by pulsations at the magnetar's rotational period. Despite the vast difference in peak luminosity, the total energy released from the aforementioned tail is remarkably similar for the three events ($\sim 10^{44}$ erg), indicating magnetic fields of the same order of magnitude for the three magnetars. The spectrum of the giant flare from SGR 1806−20 is well described by a blackbody with an initial average temperature of $\sim$ 200 keV. However, immediately after the initial spike, the emission softens rapidly, with the temperature dropping to around 10 keV (top panel "b" of Figure. 1.2). The subsequent few-second decay was non-thermal, described by a power law with an index of $\Gamma \sim 1.4$. Following the spike, there were a few seconds of further softening and a series of pulsations at the 7.5 s spin period, with spectra consisting of a combination of blackbody and power-law components (see top panel "a" in Figure. 1.2).

1.2.3.2 Short Bursts

Short bursts are the most common type of magnetar transient activities, often serving as the primary method for discovering new magnetars. These bursts typically signify the onset of a new outburst and can occur sporadically or in clusters over time. Due to their unpredictable nature, it is challenging to anticipate when or which source will emit these bursts. The peak luminosity of these bursts falls within the range of 10^{36} to 10^{43} erg s^{-1}, with duration ranging from a few milliseconds to a few seconds. The light curves of these bursts can be single or multi-peaked, with rise times generally faster than decay times. The spectra of short bursts are harder than those of the persistent X-ray emission. They are detectable below 10 keV but peak above this energy. Various models have been proposed to describe the bursts' broadband spectra (up to $\sim$ 200 keV), including single and double blackbody models, optically thin thermal bremsstrahlung models, and Comptonized models (i.e., a power law with an exponential cutoff at higher energies of the spectrum). Often, more than one model can satisfactorily describe the spectra, though a single blackbody model (with $kT_{BB} \sim$ 2–12 keV) or a sum of two blackbody models (with a second thermal component with kT_{BB} up to 15 keV) is frequently preferred.

Recently, a clear link between magnetars and fast radio bursts (FRBs) has emerged, thanks to the detection of magnetar short bursts with radio counterparts from SGR J1935+2154. On April 28, 2020, this magnetar emitted a bright, millisecond-duration radio burst that was temporally coincident with a hard X-ray bursts (see, Figure. 1.3, detailed review about this event is provided in Chapter 3; CHIME/FRB Collaboration et al., 2020; Bochenek et al., 2020; Mereghetti et al., 2020). Additionally, Israel et al. (2021) presented simultaneous X-ray and radio observations of 1E 1547−5408 performed in 2009 during its brightest outburst. They reported the detection of two radio bursts from 1E 1547−5408 reminiscent of FRBs (see Figure. 1.3). One of the radio bursts was anticipated by about 1 s ($\sim$ half a rotation period of the source) by a bright short X-ray burst, resulting in a radio-to-X-ray flux ratio of $F_{radio}/F_X \sim 10^{-9}$. These two events provided strong evidence that magnetars could be the source of at least some FRBs.
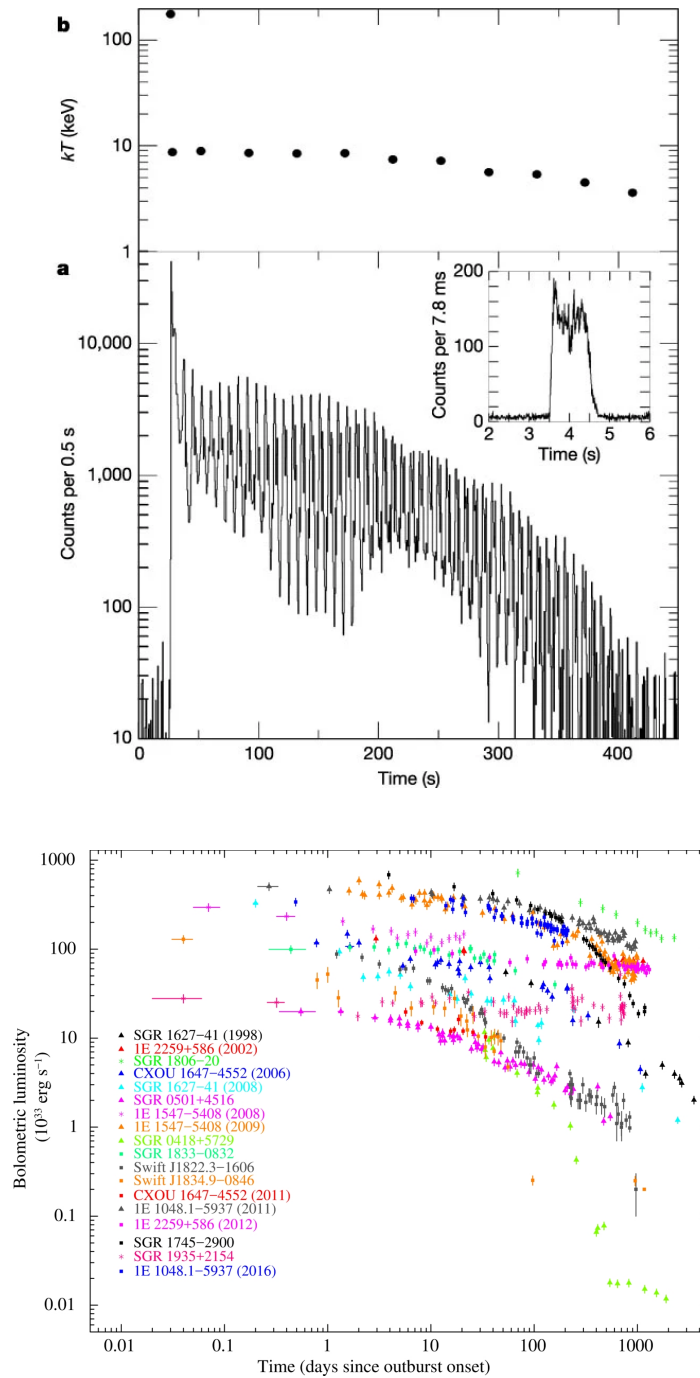
FIGURE 1.2: Top: Profiles of the 27 December 2004 giant flare from SGR 1806−20. Panel (a): The 20–100 keV light curve plotted with 0.5 s resolution, showing the flare's onset with a spike that saturated the *HESSI* detector within 1 ms at ∼26 s. The inset shows the precursor event with 8 ms resolution. Panel (b): The temporal evolution of the blackbody temperatures. Figure from (Hurley et al., 2005). Bottom: Temporal evolution of the bolometric (0.01-100 keV) luminosities for the major outbursts that occurred up to the end of 2016, featuring extensive and prolonged coverage. From (Coti Zelati et al., 2018)
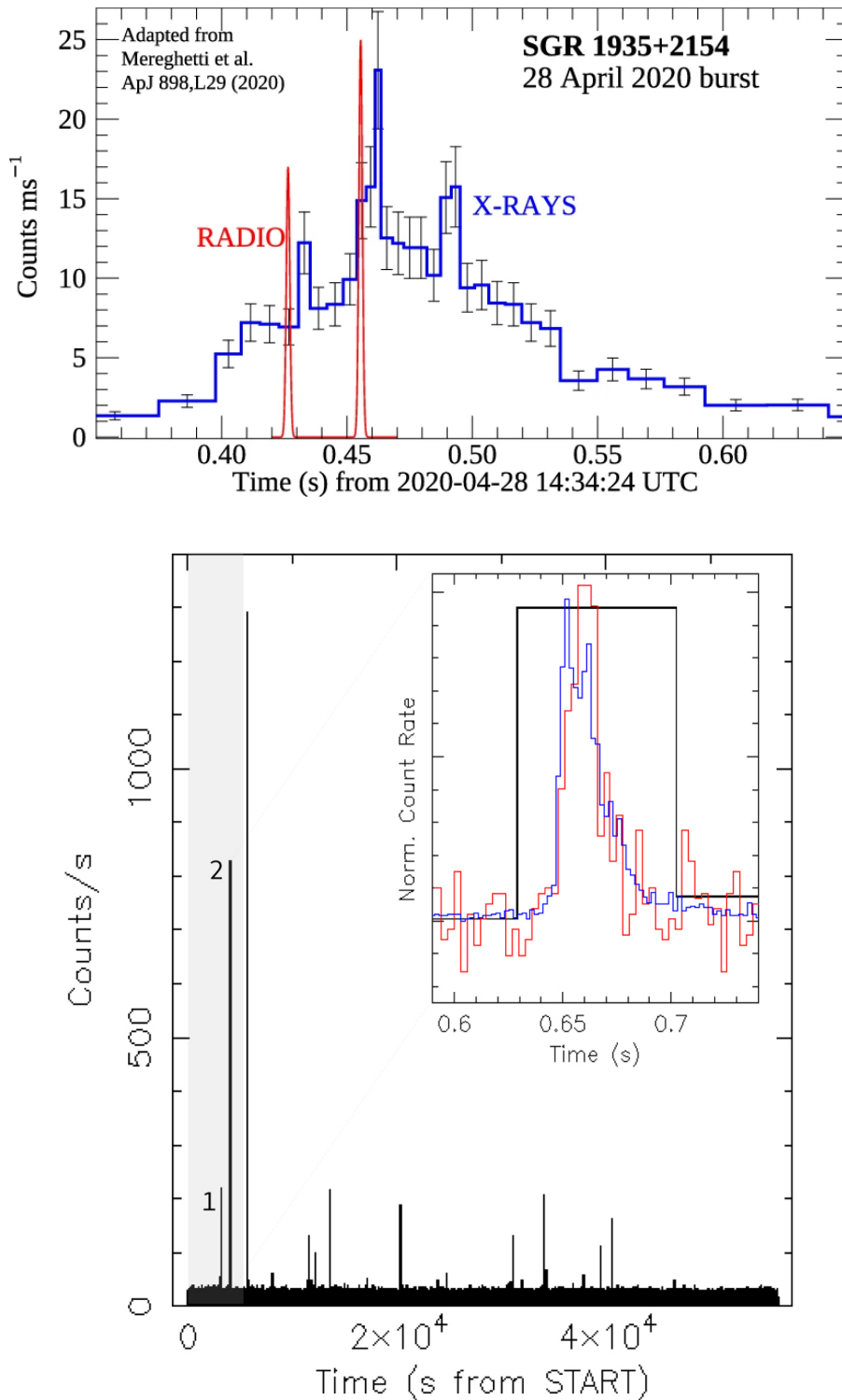
FIGURE 1.3: Top panel: hard X-ray burst (blue) detected from SGR J1935+2154 using *INTE-GRAL* instrument. Peaks 1 and 2 roughly align with the two radio peaks (red) seen from the *CHIME* detection. Adapted from Mereghetti et al. (2020). Bottom panel: *XMM–Newton* light curve (black) binned at 0.5 s. The gray area marks the time interval covered by *Parkes* observations, with detected X-ray bursts within this interval marked as 1 and 2. The inset shows burst 2 as observed by EPIC-pn (2–10 keV, black), *Swift* (15–100 keV, red) and *Konus-Wind* (20–1400 keV, blue). From Israel et al. (2021).

1.2.3.3   Outbursts

Magnetar outbursts are sudden increases of the persistent X-ray flux by a factor of
10-1000, followed by a gradual decay over a period of weeks to months/years. This
process often starts with a very rapid decay within minutes to hours, followed by a
slower fading phase described by a power law or exponential function. Figure 1.2
(bottom panel) displays the long-term light curves of all the outbursts discovered up
to the end of 2016 (see e.g. the Magnetar Outburst Online Catalog[6]; Coti Zelati et al.,
2018). The peak luminosity during outbursts can reach up to 10^{36} erg s^{-1}.
The spectra of magnetars undergo significant changes during outbursts, generally
hardening initially and then softening as the flux returns to the quiescent value over
weeks to months/years. During an outburst, the soft X-ray spectra can be described
by an absorbed blackbody plus a power law model. Typically, the blackbody tem-
perature (kT) increases by a factor of 2-3 while the photon index decreases. As the
outburst progresses, these parameters gradually revert to their quiescent values on
the same timescale as the flux decay. Outbursts are usually accompanied by changes
in timing properties. The morphology of the pulse profile, for instance, can vary dra-
matically during an outburst, both in shape and in pulse fraction. For example, the
pulse profile of magnetar SGR J1935+2154 evolved from a simple quasi-sinusoidal
structure during the first recorded outburst of the source (see, Israel et al., 2016b)
to a multi-peaked configuration during the recent outbursts (see, Figure. 1.4; and
Borghese et al., 2020; Borghese et al., 2022; Ibrahim et al., 2024). Moreover, outbursts
are often associated with glitches, which are sudden spin-ups in the range $\Delta\nu/\nu \sim$
$10^{-9} - 10^{-5}$ (Dib, Kaspi, and Gavriil, 2008).

Magnetar outbursts are believed to be triggered by heat deposition in a lo-
calised area of the magnetar's surface, however the exact heating mechanism re-
mains poorly understood. Magnetic stresses in a localised region of the neutron
star's crust deform part of the crust plastically, converting magnetic energy into heat.
This heat is then conducted up to the surface layers and radiated as a thermal emis-
sion (e.g., Gourgouliatos and Lander, 2021). Additionally, the plastic flows within
the crust can generate thermoplastic waves, leading to crustal displacements that
implant a strong twist in the magnetic field lines in the magnetosphere, typically in
a confined region (Li, Shao, and Li, 2016). The currents flowing in this twisted bun-
dle of field lines produce additional heating as they hit the neutron star's surface
(Beloborodov, 2009; De Grandis et al., 2021).

Transient pulsed radio emission is another activity linked to X-ray outbursts in
magnetars. To date, 6 magnetars have shown such emission; XTE J1810−197 is the
first radio-loud magnetar to be discovered (Camilo et al., 2006). Interestingly, dur-
ing its radio activation, XTE J1810−197 became the brightest pulsar in the radio sky,
with individual pulses reaching flux densities of 10 Jy or more. Subsequent discov-
eries include: 1E 1547−5408 (with a spin period of ~ 2.1 s, it is the second fastest
rotating magnetar up to date, Camilo et al., 2007); PSR J1622−4950 (the only mag-
netar discovered in the radio band, Levin et al., 2010); and PSR J1745−2900 (located
near the Galactic center, Eatough et al., 2013). More recently, Swift J1818.0−1607 and
SGR J1935+2154 have been added to this list of magnetars.

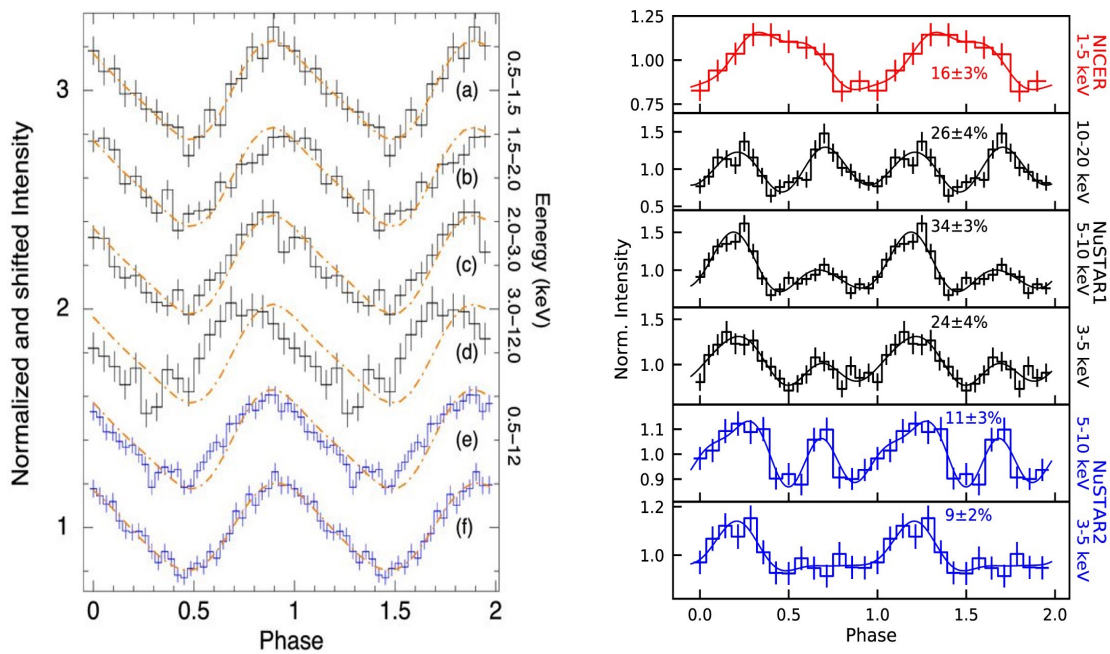
[6]MOOC: http://magnetars.ice.csic.es/

FIGURE 1.4: Energy-resolved, background-subtracted pulse profiles of SGR J1935+2154: Left, from Israel et al., 2016b, using *Chandra* and *XMM–Newton* data. From top to bottom, the profiles (a) to (e) correspond to increasing energy levels as specified. The dashed orange curve shows the best fit for profile (a) with two sinusoids, revealing a shift towards earlier phases with increasing energy. Profile (f) is obtained by aligning profiles (a) to (d). Right, from Borghese et al., 2020 using *NICER* and *NuSTAR* data. Solid lines represent the best-fitting models, using two sinusoidal components (fundamental plus harmonics) for *NICER* and three for *NuSTAR*. The corresponding pulsed fractions are indicated in each panel.

1.3 X-ray instruments

The study of neutron stars and other high-energy astrophysical phenomena has greatly advanced with the development of X-ray instruments with excellent observation capabilities. Since the launch of the first X-ray satellite *Uhuru*[7] in 1970 (Giacconi et al., 1971), and over the subsequent decades, a variety of space-based X-ray observatories have been launched. Key instruments include the *Chandra* X-ray Observatory (Weisskopf et al., 2000), known for its high-resolution imaging capabilities, and the *INTEGRAL* satellite (Winkler et al., 2003), which provides valuable insights through its broad energy range. Recently launched missions like *Einstein Probe (EP)* (excellent for high energy transients and variable object monitoring; Yuan et al., 2022) and future mission such as *NewAthena*[8] aim to continue this legacy, offering advanced technologies for exploring the X-ray sky. This Section discusses the primary X-ray instruments used in this thesis, focusing on their technical specifications, operational modes, and contributions to our research on neutron stars.

1.3.1 XMM-Newton

Launched by the European Space Agency in 1999, the X-ray Multi-mirror Mission Newton (*XMM–Newton*) represents a cornerstone in study of the Universe at X-ray wavelengths (Jansen et al., 2001). Equipped with mirrors that have a large collecting area, *XMM–Newton* hosts three X-ray instruments, each feeding into the European Photon Imaging Camera (EPIC) and an Optical Monitor (OM) that extends capabilities into the UV/optical bands. The EPIC is integral to *XMM–Newton*'s observational prowess and comprises two Metal Oxide Semiconductor (MOS) cameras and one pn CCD camera. The *XMM–Newton* EPIC cameras operate across a broad energy range of 0.15–12 keV and provide a field of view of $\sim 30'$. They offer extremely sensitive imaging observations with an angular resolution of $6''$ full width at half maximum (FWHM) and $\sim 15''$ half energy width (HEW). The spectral resolution is moderate, with $E/\Delta E \sim$ 20–50. The EPIC-pn camera (Strüder et al., 2001) is particularly notable for its substantial effective area of $\sim 1400 \, cm^2$ at 1.5 keV, significantly larger than the $500 \, cm^2$ for each MOS camera at the same energy (Turner et al., 2001).

The EPIC-pn camera, equipped with 12 CCDs and the MOS cameras, each with 7 CCDs, feature multiple modes to optimize the data collection. In the Full Frame mode, the entire field of view is covered as all the pixels of all CCDs are read out, providing a time resolution of 73.4 ms for pn and 2.6 s for MOS. In the Partial Window (PW) mode, the pn camera can switch to Large Window mode to read only half the area of all CCDs, enhancing the time resolution to 47.7 ms, or to Small Window mode focusing on just a segment of one CCD (i.e., CCD 4), which sharpens the time resolution further to 5.7 ms. For the Partial Window mode of the MOS cameras, only part of the central CCD chip is read out, and it can be operated in different modes, including Small and Large Window modes with time resolution of 0.3 s and 0.9 s, respectively. The Timing mode is available for both pn ans MOS cameras with resolution of 0.03 ms and 1.75 ms respectively. Furthermore, the pn camera's exclusive Burst mode offers an extremely high time resolution of 7 μs. For both Burst and Timing modes, spatial information is returned only along X axis while it is lost on

---

[7]Uhuru:
https://heasarc.gsfc.nasa.gov/docs/uhuru/uhuru.html
[8]NewAthena:
https://www.the-athena-x-ray-observatory.eu/en/athena-mission

the Y axis due to the continuous shifting and collapsing of rows (for detailed review, *XMM-Newton Users Handbook* 2023).

To facilitate data analysis for these diverse operational modes, the Science Analysis Software (SAS[9], Gabriel et al. 2004) is extensively used. SAS is designed for processing and analysing *XMM–Newton* data, featuring reduction pipelines that calibrate science files and produce event lists and calibrated images. Additionally, SAS offers software tools for extracting spectra, light curves, and generating source lists and instruments response matrices.

In this thesis, our primary focus lies on the data taken with the EPIC-pn camera due to its higher counting statistics owing to its larger effective area compared to the MOS cameras. However, the MOS cameras are invaluable for verifying the consistency of our results. Additionally, we utilized the EPIC-MOS1 to extract radial profiles to investigate potential diffuse emission surrounding the magnetar SGR J1935+2154, thus complementing the detailed data provided by the EPIC-pn camera.

1.3.2 *Swift*

The Neil Gehrels Swift Observatory (*Swift*, Gehrels et al., 2004) is a multi-wavelength space observatory, launched in 2004 and dedicated to the study of gamma-ray bursts (GRBs) and their afterglows across different wavelengths, from gamma rays to optical light. *Swift* carries three primary instruments, which together enable rapid detection and follow-up of transients astronomical events: the Burst Alert Telescope (BAT, Barthelmy et al., 2005), which operates in the 15–350 keV energy band; the X-ray Telescope (XRT, Burrows et al., 2005a), sensitive to the 0.3–10 keV band; and the UV/Optical Telescope (UVOT; wavelengths range 170-600 nm, Roming et al., 2005).

Swift's BAT, with its wide field of view of ~ 2 steradians, is designed for the initial detection of high-energy bursts. It spends most of its operational time in scan-survey mode, continuously monitoring the sky for burst events. Upon detecting a burst, BAT swiftly transitions into burst mode, capturing and recording high-time resolution data specific to the burst event. This rapid switch between the two modes facilitates the quick localisation of the source position to an accuracy of $\sim 1' - 4'$ within just 20 s of detection. Following the trigger, BAT can prompt the spacecraft to reorient within 20-70 s, enabling rapid follow-up observations by the XRT and the UVOT telescopes.

The *Swift*'s XRT has a field of view of $23' \times 23'$ and effective area of $110 \, \mathrm{cm}^2$ at 1.5 keV. It features two operational modes: Photon Counting (PC) mode, where the entire CCD is read every 2.5 s, providing high-resolution imaging and spectroscopy; Windowed Timing (WT) mode, which operates by utilising a window of 200 columns that cover the central $8'$ of the field of view. This mode maintains imaging information along one spatial dimension. As a result, spatial imaging data is sacrificed to enhance temporal resolution up to $\sim$1.8 ms. In this thesis, the data obtained from *Swift* particularly using XRT in both PC and WT modes were crucial for monitoring the evolution of the X-ray emission properties from the magnetar Swift J1818.0−1607 from the onset of its outburst.

---

[9]SAS: https://www.cosmos.esa.int/web/xmm-newton/sas

1.3.3   *NuSTAR*

The Nuclear Spectroscopic Telescope Array (*NuSTAR*), launched in 2012, represents a significant advancement in the field of of high-energy astrophysics as the first space telescope to focus high-energy X-rays in the 3 – 79 keV range (Harrison et al., 2013). *NuSTAR* is equipped with two co-aligned hard X-ray telescopes that focus onto two focal plane modules, refereed to as FPMA and FPMB. The instruments are designed to be nearly identical, enhancing the ability to merge images and maximise sensitivity. *NuSTAR*'s architecture offers a compact field of view of $\sim 12' \times 12'$ and a peak effective area of about $900\,cm^2$ at 10 keV, considering both modules. Additionally, *NuSTAR* has a angular resolution of about $18''$ FWHM and a good spectral energy resolution of 400 eV at 10 keV, increasing to 900 eV at 68 keV. The high-resolution capabilities are crucial for studying the non-thermal emission from young supernova remnants and hard X-ray emitting compact objects within our Galaxy, such as magnetars during outburst phases. Moreover, *NuSTAR*'s precise timing accuracy, of the order of a few milliseconds, allows for detailed timing analysis of these celestial objects. The precision enabled us to detect bursts in both Swift J1818.0−1607 and SGR J1935+2154. For the spectra analysis, we typically utilize only the spectra from FPMA, and verify that FPMB gives consistent results.

NuSTAR's Data Analysis Software (NUSTARDAS[10]) is essential for processing *NuSTAR* observations. The software facilitates calibration and standard data processing of event files, generating high-quality scientific products such as cleaned event lists, images, spectra and light curves.

1.3.4   *NICER*

The Neutron star Interior Composition Explorer (*NICER*) is an X-ray astrophysics mission launched aboard the International Space Station (ISS) in June 2017. It is designed to observe X-ray emission from neutron stars (NSs) with a primary objective of studying the extreme gravitational, electromagnetic, and nuclear-physics environment in and around NSs (Gendreau et al., 2016). *NICER*'s X-ray Timing Instrument (XTI) consists of a co-aligned array of 56 X-ray concentrator (XRC) optics and associated silicon drift detector (SDDs). Each XRC collects photons, within energy range of 0.2–12 keV over an effective area of $\sim 1900\,cm^2$ at 1.5 keV and focus them onto a small SDD. This setup allows *NICER* to achieve an excellent timing resolution of < 300 ns, combined with a moderate spectral resolution of $\sim 3\,\%$ at 1 keV (85 eV at 1 keV).

Data collected by *NICER* is processed using the *NICER* Data Analysis Software (NICERDAS)[11], which calibrates and cleans the event files to produce high-quality scientific products such as spectra, light curves and cleaned event files. In this thesis, *NICER* data were crucial for the long-term study of the 2020 magnetar -like outburst of the young pulsar PSR J1846−0258.

---

[10]NUSTARDAS:
https://heasarc.gsfc.nasa.gov/docs/nustar/analysis/
[11]NICER- DAS:
https://heasarc.gsfc.nasa.gov/docs/nicer/data_analysis/nicer_analysis_guide.html

1.3.5 *eROSITA*

Launched on July 13, 2019, the extended ROentgen Survey with an Image Telescope Array (*eROSITA*, Predehl et al., 2021) is the primary instrument on the Spectrum-Roentgen-Gamma (SRG; Sunyaev et al., 2021) mission. Developed under the leadership of the Max Planck Institute for Extraterrestrial Physics (MPE) in Germany, *eROSITA* is designed to conduct deep surveys of the entire X-ray sky. In the soft X-ray band (0.2–2.3 keV), the *eROSITA* survey is about 25 times more sensitive than the *ROSAT* all-sky survey, and in the hard band (2.3–8 keV), it provides the first ever true imaging survey of the sky at those energies. Complementing *eROSITA*'s capabilities, ART-XC (Astronomical Roentgen Telescope X-ray Concentrator, Pavlinsky et al., 2022), developed under the lead of the Russian Space Research Institute (IKI). It extends the energy up to the hard X-ray range of 4–30 keV, making SRG a highly competitive observatory and enhancing its overall scientific output.

eROSITA consists of seven identical and co-aligned X-ray mirror assemblies (MAs) housed in a common optical bench. Each of the mirror uses a Wolter-I geometry with 54 paraboloid/hyperboloid mirror shells. Each of the MAs has a corresponding CCD camera, forming camera assemblies (CAs). These CCDs have 384×384 pixels and cover a circular field of view with a a diameter of ~ 1 degrees. The nominal integration time for the CCDs is 50 ms. *eROSITA* operates in three main observing modes: survey, the primary mode during the all-sky survey phase; pointing, a single target is observed at a given time; and field scan, sky region of 12.5×12.5 degrees is scanned.

Data from *eROSITA* are processed using the *eROSITA* Science Analysis Software System (eSASS[12]), which produces event lists, images, exposure maps, and source catalogs and supports all the observing modes. The first data release DR1[13] from *eROSITA* makes public the data from the first six months of the SGR/sROSITA all-sky survey (eRASS1). The proprietary rights to this data belong to the German *eROSITA*, consortium (eROSITA-DE). This public data release provides an extensive set of calibrated data products. It demonstrate the instrument's capability to fulfill its scientific objectives and offering invaluable resources for a wide range of the astrophysical studies.

1.4 Thesis outlines

The discovery of pulsars in 1967 marked a significant milestone in astrophysics, revolutionising our understanding of compact stellar remnants and the extreme environment in which they exist. Since then, extensive research has focused on exploring the diverse population of neutron stars and their emission mechanisms.

The primary aim of this thesis is to enhance our understanding of neutron stars, particularly magnetars, by investigating their transient activities such as outbursts and bursts through multi-wavelength observations, specifically in X-ray and radio data. Additionally, the thesis includes ongoing search for new pulsars and the development of a pipeline for the detection and analysis of X-ray transient sources.

The thesis is organised into six main chapters. In Chapter 2 and Chapter 3, we focus on the study of spectral and temporal properties during the outburst events of magnetars Swift J1818.0−1607 and SGR J1935+2154, respectively.

---

[12]Updated version for eSASS DR1:
https://erosita.mpe.mpg.de/dr1/eSASS4DR1/
[13]eROSITA-DE Data Release 1(DR1):
https://erosita.mpe.mpg.de/dr1/

We study the first outburst of the young magnetar Swift J1818.0−1607 using extensive X-ray observations from *XMM–Newton*, *NuSTAR*, and *Swift*. The analysis of the data shows a decreasing trend in time of the magnetar's emitting region size from ∼0.6 to ∼0.2 km, and notable torque variability over time. Additionally, diffuse X-ray and radio emission is detected from *VLA* data around Swift J1818.0−1607, suggesting possible associations with a dust-scattering halo and a supernova remnant, respectively.

We study the galactic magnetar SGR J1935+2154, following its 2022 outburst, using X-ray data from *XMM–Newton* and *NuSTAR*, observed (quasi-)simultaneously during two epochs separated by ∼5 days. The analysis of the persistent X-ray emission reveals consistent blackbody properties with a radius of R_{BB} ∼1.9 km and temperature of kT_{BB} ∼0.4 keV, alongside slight changes in the powerlaw parameters. The timing analysis shows an increased spin-period derivative, i.e. approximately 4 times the value of the first detected outburst, indicating changes in the magnetospheric geometry and/or the relativistic wind of SGR J1935+2154 during each outburst event.

Chapter 4, focuses on the search for an isolated magnetic white dwarf pulsar, ZTF J190132.9+145808.7 (here, ZTF J1901+1458). This chapter present the results of a search through archival radio data from the Australian Square Kilometer Array Pathfinder (*ASKAP*) and the *VLA*. We did not detect any radio emission from ZTF J1901+1458 down to sensitivity limits of 0.4 mJy and 0.8 mJy for *ASKAP* and *VLA*, respectively. The analysis also included a search for variability in the radio emission, with no evidence of emission in 10-second timestep images.

Chapter 5, provides a short overview of ongoing efforts of the *eBANDERAS* project, a pipeline aimed at characterising variability in X-ray data. Particularly, the chapter focuses on the transients search module, discussing the current status and the future plans to integrate and optimise the search for X-ray transients within *eBANDERAS*.

TABLE 1.1: Comparison of X-ray Instruments. This table summarizes the key parameters of various X-ray instruments used in high-energy astrophysics, arranged by their launch dates from oldest to newest. The comparison includes the energy range, field of view, angular resolution, effective area, timing resolution, and the specific camera/detector used in each instrument.

Instrument's Parameter	XMM-Newton	Swift	NuSTAR	NICER	eROSITA
Energy Range	0.1–12 keV	0.3–10 keV (XRT) 15.–350 keV (BAT)	3–79 keV	0.2–12 keV	0.2–8 keV
Field of View	~30′	~23′ × 23′ (XRT) ~2 steradian (BAT)	~12′ ×12′	30′ (ISS mounted)	1° diameter
Angular Resolution	6″ FWHM	~18″ (XRT)	18″ FWHM	~3% at 1 keV	16.1″ HEW (at 1.5 keV)
Effective Area	1400 cm^2 (pn) 500 cm^2 (MOS)	110 cm^2 (XRT)	900 cm^2 (at 10 keV)	1900 cm^2 (at 1.5 keV)	~1200 cm^2 at 1 keV
Timing Resolution	0.03 ms (pn) 1.75 ms (MOS)	~1.8 ms (WT mode)	Few ms	<300 ns	50 ms
Camera/Detector	EPIC-pn, MOS1-2	XRT, BAT, UVOT	FPMA, FPMB	XTI	7 CCDs (7 MAs)

Unique Features:
XMM-Newton: High sensitivity, multiple operational modes
Swift: Rapid response to GRBs, multi-wavelength capabilities
NuSTAR: High-energy focus, precise timing accuracy
NICER: Excellent timing resolution, moderate spectral resolution
eROSITA: Wide-field imaging, high sensitivity all-sky survey

2 Deep X-ray and Radio Observations of the First Outburst of the Young Magnetar Swift J1818.0−1607

2.1 The Young Magnetar Swift J1818.0−1607

Swift J1818.0−1607 is the sixth[1] and the most recent magnetar to be observed with pulsed radio emission. It was discovered on 2020 March 12, when the Burst Alert Telescope (BAT) on board the *Neil Gehrels Swift Observatory* (Gehrels et al., 2004) triggered on a short burst of ∼ 0.1 second, which led to the discovery of a new magnetar (Evans et al., 2020). Following this trigger, 64.2 seconds later, the *Swift* X-ray Telescope (XRT) started observing the field and reported a new X-ray source, Swift J1818.0−1607 (hereafter, Swift J1818.0−1607). Four hours after the *Swift*/BAT alert, the Neutron star Interior Composition Explorer (*NICER*) started a series of observations of the source which revealed a coherent periodicity of 0.733417(4) Hz (Enoto et al., 2020). The *NICER* periodicity and the magnetar-like burst detected by *Swift*/BAT suggested that Swift J1818.0−1607 is a new fast-spinning magnetar with a spin period of 1.36 s.

Follow-up radio observations performed by the 100-m Effelsberg radio telescope and the 76-m Lovell Telescope detected radio pulsations at a frequency of 0.7334110(2) Hz, confirming Swift J1818.0−1607 as a radio-loud magnetar (Karuppusamy et al., 2020). The radio monitoring campaign provided a measurement of the spin-period derivative of $\dot{P} = 8.16(2) \times 10^{-11}\,\mathrm{s\,s^{-1}}$, resulting in a first estimate of the dipolar surface magnetic field at the equator of $B \sim 3.4 \times 10^{14}$ G and a characteristic age of ∼ 265 yr (Karuppusamy et al., 2020; Champion et al., 2020a; Esposito et al., 2020). Even from these early estimates of the timing parameters, it was clear that this new magnetar is very young compared to the rest of the magnetar population. Additionally, the dispersion measure DM = 706(4) $\mathrm{cm^{-3}}$ pc suggested a source distance of 4.8 or 8.1 kpc, depending on the model used for the Galactic free electron density (Karuppusamy et al., 2020; Champion et al., 2020a).

Since its discovery, several X-ray (Esposito et al., 2020; Hu et al., 2020; Blumer and Safi-Harb, 2020) and radio telescopes (Karuppusamy et al., 2020; Champion et al., 2020b; Lower et al., 2020a; Lower and Shannon, 2020; Huang et al., 2021; Rajwade et al., 2022) have monitored this young magnetar during the evolution of its outburst, confirming its noisy spin-period evolution and X-ray outburst decay. Here we report on follow-up observations with *XMM–Newton*, *NuSTAR*, *Swift* and INTEGRAL to study the X-ray spectral and timing evolution of Swift J1818.0−1607 along the decay

---

[1]We include SGR J1935+2154 in the sub-group of radio loud magnetars. For this source, the detection of a periodic radio emission by FAST was claimed in the aftermath of a radio bursting period in 2020 October (Zhu et al., 2020).
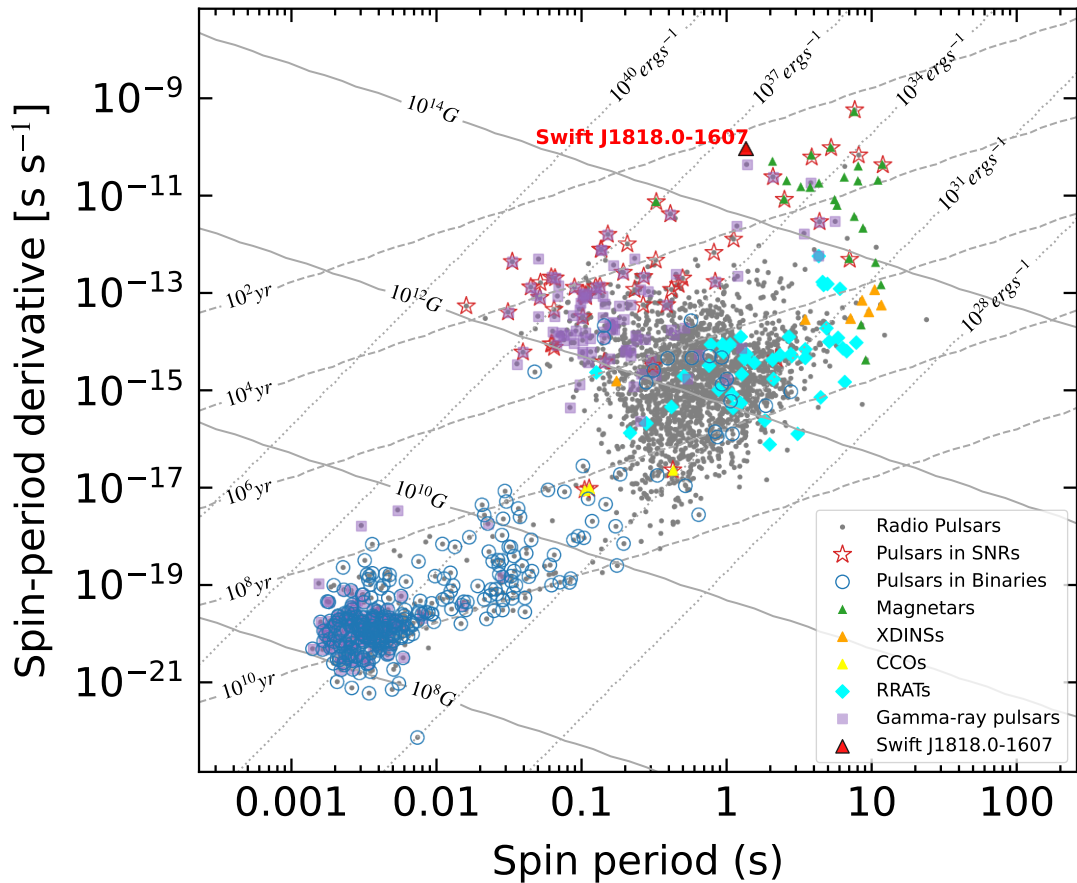
FIGURE 2.1: The $P\dot{P}$ diagram highlights the Swift J1818.0-1607 magnetar, marked in red, among various pulsars. It also features radio pulsars (grey dots), RRATs (cyan diamonds), gamma-ray pulsars (purple squares), XDINSs, CCOs, and shows lines for characteristic age, magnetic fields, and spin-down luminosity. Adapted from (with permission; Ronchi, 2024) and updated with data from the ATNF pulsar catalogue (version: 2.2.0; Manchester et al., 2005).

of its first outburst, covering ∼19 months since the outburst onset. Furthermore, we report on radio continuum observations performed with the VLA, that allowed us to search for the supernova remnant around this young pulsar, leftover of the ejected materials after the supernova explosion (see full review by Vink, 2012).

We describe the observations and data reduction in Section 2.2. In Section 2.3, we introduce the X-ray spectral analysis for the diffuse emission observed around the magnetar (Sec. 2.3.1) and for the magnetar itself (Section. 2.3.2), a burst search (Section. 2.3.3), the X-ray timing analysis (Section. 2.3.4) and the analysis of radio continuum data (Section. 2.3.5). Finally, we discuss the results in Section 2.4.

2.2 X-ray Observations and data reduction

We report the log of the observations used in this work in Table (A.1, in Appendix A). We performed the data reduction using the HEASOFT[2] package (v.6.29c; NASA High Energy Astrophysics Science Archive Research Center - HEASARC, 2014). All uncertainties in the text are reported at 1σ confidence level, unless otherwise specified. Throughout this work, we adopt a distance of 4.8 kpc (Karuppusamy et al., 2020).

2.2.1 XMM-Newton

Swift J1818.0−1607 was monitored four times with the European Photon Imaging Camera (EPIC) on board the *XMM–Newton* satellite between 2020 March 15 and October 8 for a total exposure time of ∼137 ks. The exposures ranged from 22 ks to 49 ks (Table A.1). The EPIC-pn (Strüder et al., 2001) was set in large window mode (LW; timing resolution of 47.7 ms) for the first observation and in full frame mode (FF, timing resolution of 73.4 ms) for the remaining observations, while both Metal Oxide Semi-conductor cameras (MOS; Turner et al., 2001) were operating in small window mode (SW; timing resolution of 0.3 s). Raw data were analyzed with the SAS[3] software package (v.19.1.0; Gabriel et al., 2004). We cleaned the observations from periods of high background activity. This resulted in a net exposure time of 11.2, 9.5, 16.4 and 19.6 ks for the four observations ordered chronologically. No pileup was detected. We selected the source photon counts from a circle of 30″ radius, while the background level was estimated from a circle of 100″ radius, on the same CCD away from the source. For the diffuse emission, we extracted the spectrum by selecting source photon counts from an annulus of radii 50″ – 110 ″, centered on the source, and used the same background region as adopted for the point-like source (more details in Subsection 2.3.1). We focused this study on the EPIC-pn data, but checked that MOS data gave consistent results.

2.2.2 NuSTAR

The Nuclear Spectroscopic Telescope ARray (*NuSTAR*; Harrison et al., 2013) observed Swift J1818.0−1607 six times starting on 2020 March 3 and ending on 2020 September 7 for a total exposure time of ∼180 ks (see Table A.1). The longest exposure was 59 ks taken under Obs.ID 80402308004, while the shortest exposure was 12 ks for Obs.ID 80402308010. The source photon counts were extracted from a circle

---

[2]heasoft:
https://heasarc.gsfc.nasa.gov/docs/software/heasoft/
[3]SAS:
ttps://www.cosmos.esa.int/web/xmm-newton/sas

of radius 100″ in the first three observations and from a smaller circle in the following three observations (the adopted radii varied in the range 50″– 80″ mainly depending on the presence of significant stray light contamination near the source position). The background level was estimated from a circle of radius 100″ located near the source position in all cases.

2.2.3 Swift

Swift/XRT (Burrows et al., 2005b) extensively monitored Swift J1818.0−1607 since the outburst onset until the end of October 2021. The observations were carried out either in photon counting mode (PC, time resolution of 2.51 s) or in windowed timing mode (WT, time resolution of 1.7 ms). Data were reprocessed using standard prescriptions and software packages such as XRTPIPELINE[4]. Source counts were accumulated within a circular region of radius of 20 pixels (i.e. 1-XRT pixel corresponds to 2″.36), while the background photons were extracted from an annulus with radii of 100–150 pixels and from a 20-pixel-radius circle for PC-mode and WT-mode observations, respectively.

2.2.4 INTEGRAL

INTEGRAL (Winkler et al., 2003) observed Swift J1818.0−1607 between 2020 March 13 at 21:22:56 UT and 2020 March 16 at 03:47:32 UT as part of our approved magnetar ToO program, for a total exposure time of about 105 ks. Unfortunately, its soft X-ray spectrum did not allow detection in the hard X-ray band. We derived 3σ upper limits on the observed flux with ISGRI (Lebrun et al., 2003) at the level of 1.8×10^{-11} erg s^{-1}cm^{-2} (28–40 keV) and 3.5×10^{-11} erg s^{-1}cm^{-2} (40–80 keV).

2.3 Analysis and results

2.3.1 Diffuse Emission

The diffuse emission around Swift J1818.0−1607 has been investigated in a number of previous studies. Using an *XMM–Newton* observation performed a few days after the outburst onset, Esposito et al. (2020) reported the detection of diffuse emission extending between 50″– 110″ around Swift J1818.0−1607. Another study by Blumer and Safi-Harb (2020) showed the presence of diffuse emission also on smaller angular scales, up to 10″ using *Chandra* observations.

To constrain the spatial extent of the large-scale diffuse emission, we extracted the radial profile of the observed surface brightness up to a distance of 300″ away from the source for all four *XMM–Newton* observations. We fit it using a King function reproducing the EPIC-pn point-spread function (PSF; Ghizzardi 2002) with the addition of a constant term to model the background level. We found a photon excess associated with the diffuse emission at radial distances within $\sim 50''$ – 110″ in all four pointings (see Figure 2.2, top panel).

To further investigate the energy dependency of the diffuse structure, we built surface brightness profiles in two different energy bands, 0.3–7 keV and 7–10 keV (see

---

[4]xrtpipeline:
https://www.swift.ac.uk/analysis/xrt/xrtpipeline.php
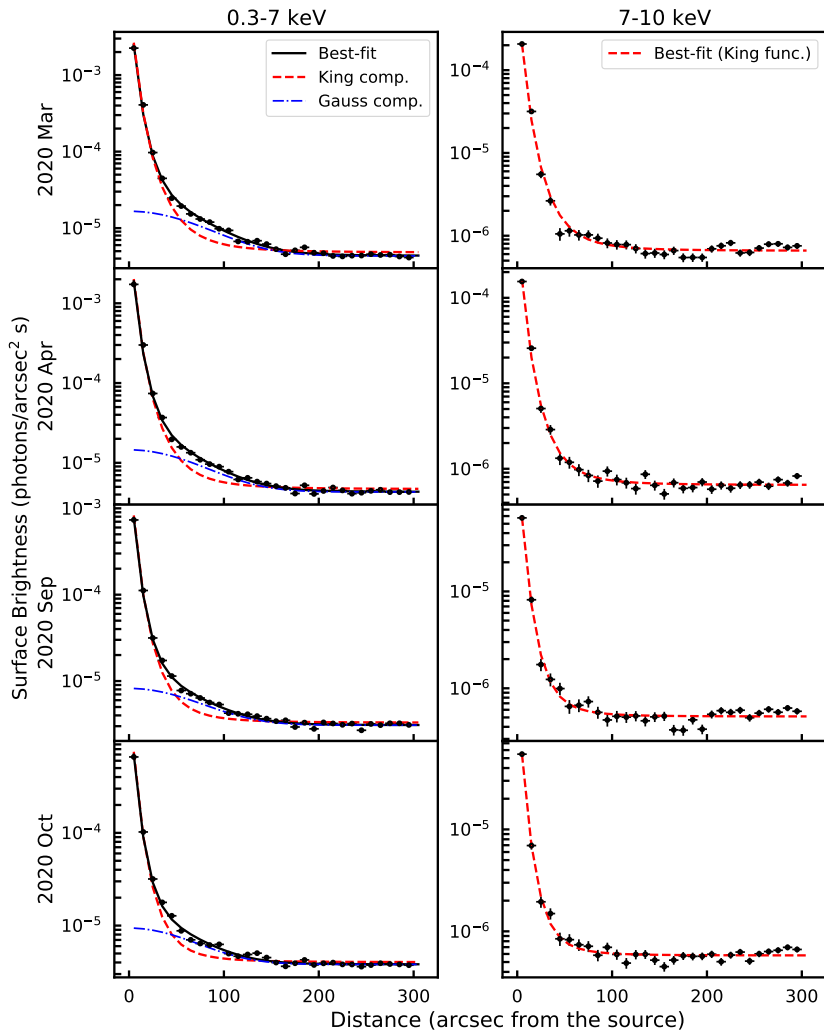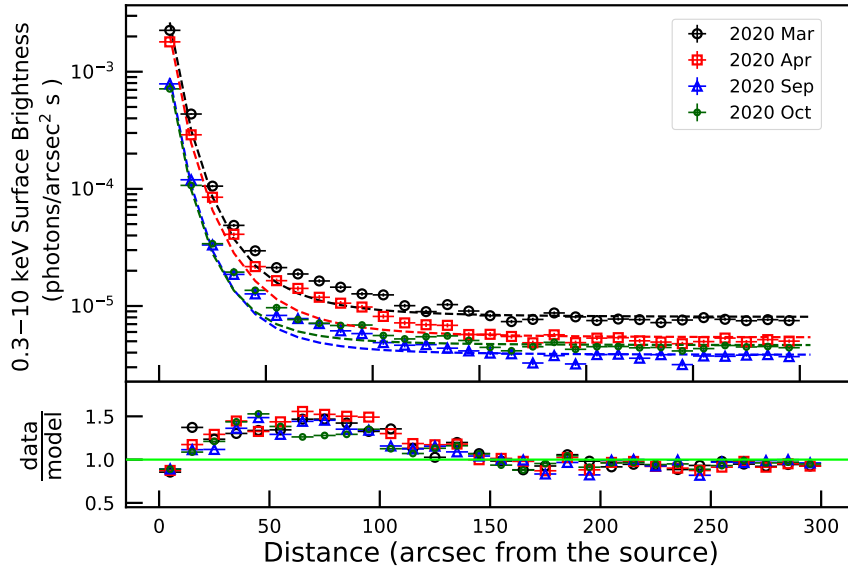
FIGURE 2.2: *Top*: Observed X-ray surface brightness up to a radial distance of 300″ in the 0.3–10 keV energy range extracted from the four *XMM–Newton* observations (the error bars are smaller than the size of the markers). The dashed lines represent the best-fit PSF model. The ratio between the data and the best-fit model is plotted in the bottom panel. *Bottom*: Observed X-ray surface brightness up to a radial distance of 300″ in two different energy bands, 0.3–7 keV (left) and 7–10 keV (right). The best-fitting models are superimposed.
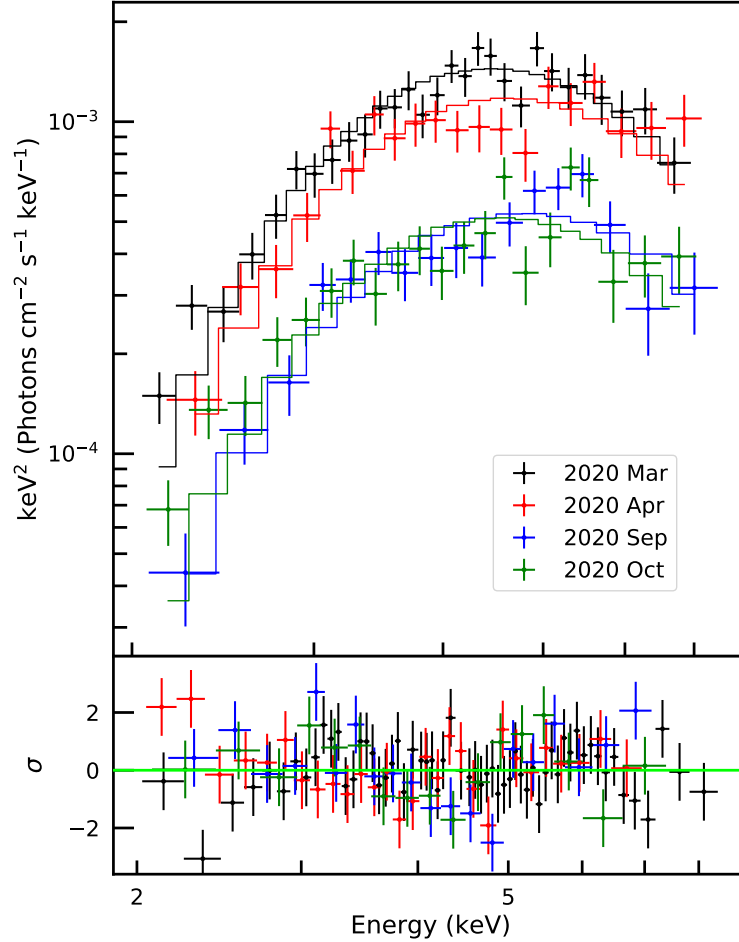
FIGURE 2.3: $E^2 f(E)$ unfolded spectra of the diffuse emission extracted from the four *XMM–Newton* observations. The solid lines mark the absorbed blackbody model. Post-fit residuals in units of standard deviations are shown in the bottom panel.

Figure 2.2, bottom panel). In the soft energy interval, we included a Gaussian function in the above-mentioned model in order to properly describe the observed photon excess, while this component is not required in the hard band (*F*-test probability >0.001 for its inclusion).

We extracted the 0.2–7.5 keV spectra associated with the diffuse emission by selecting photons within an annulus centered on Swift J1818.0−1607 with radii of 50″ and 110″ respectively, and grouped them using the SPECGROUP tool to have a minimum bin size of 100 counts per bin. The ancillary response files for the diffuse emission spectra were generated using the ARFGEN tool with the extendedsource parameter set to yes, while the redistribution matrix files were created via the RMF-GEN script.

To study the spectral behavior of the diffuse component, we performed a simultaneous fit of the source and diffuse emission spectra obtained from the four EPIC-pn observations. The former were described by an absorbed two-blackbody model, while for the latter we adopted a single absorbed blackbody. The hydrogen column density N_H was quantified with the TBABS model with the abundance of the interstellar medium taken from Wilms, Allen, and McCray (2000) and the photoionization cross-section model from Verner et al. (1996). In the fits, the N_H was forced to be the same among all the data sets. At each epoch, the diffuse emission temperature and normalization were tied up between the source and diffuse
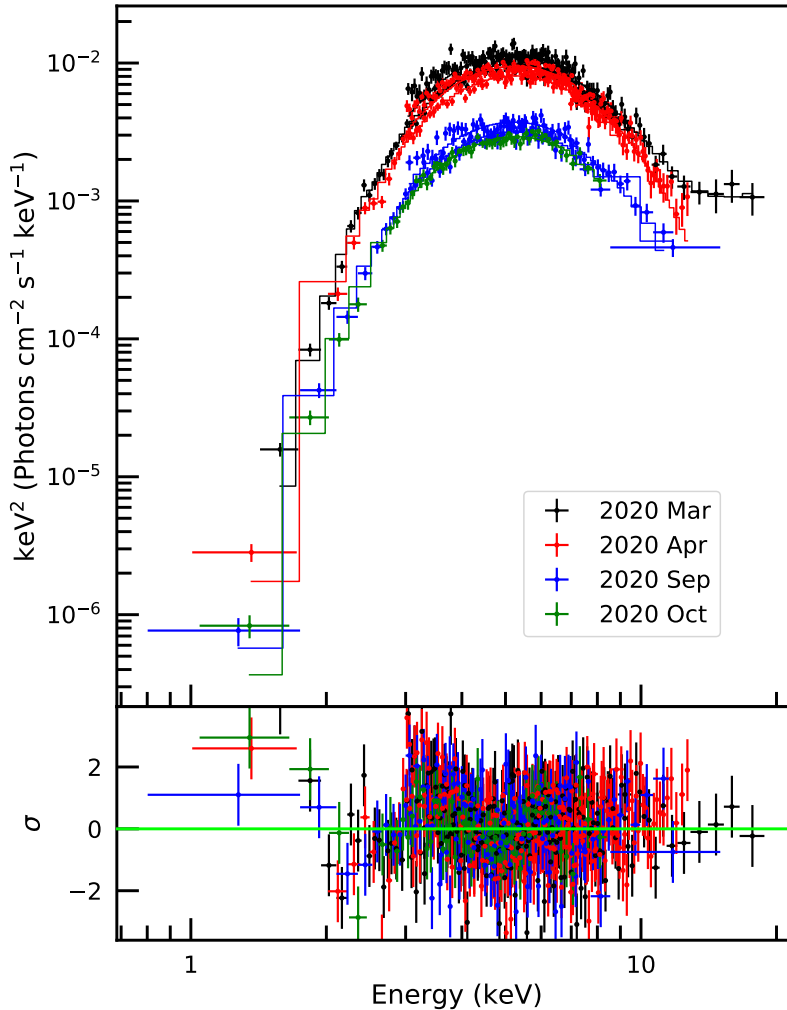
FIGURE 2.4: $E^2 f(E)$ unfolded spectra of Swift J1818.0−1607 from *XMM–Newton* and *NuS-TAR* observations. In the fit we adopted a model consisting of two blackbodies, except for the 2020 March spectra where we included a power law (χ_ν^2 = 1.41 for 607 d.o.f.). Post-fit residuals in units of standard deviations are shown in the bottom panel.

emission spectra. Overall, the fit gave a satisfactory description of the data with $N_{\rm H} = (1.23\pm0.02)\times10^{23}\,{\rm cm}^{-2}$ and a reduced chi-squared χ_ν^2=1.2 for 332 degrees of freedom (d.o.f.). The best-fitting values for the temperature $kT_{\rm diff}$ and the observed 0.3–10 keV flux $F_{\rm X.diff}$ for the diffusion emission are listed in Table 2.1. Figure 2.3 shows the unfolded spectra of the diffuse emission at the four different epochs with the best-fitting model, marked by a solid line, and the residuals with respect to this model.

We detected a flux reduction of the diffuse X-ray emission of about 35% (decreasing from 1.9 to 0.6 $\times10^{-11}\,{\rm erg\,s}^{-1}{\rm cm}^{-2}$) between 2020 March and October. The large flux variability and the soft X-ray spectrum suggest a dust scattering-halo as the source of this diffuse emission.

2.3.2 Spectral Analysis

We used the *XMM–Newton* and *NuSTAR* data to study the X-ray emission of Swift J1818.0−1607 from soft to hard X-rays. For the *XMM–Newton*/EPIC-pn observations, we grouped the X-ray spectra using the SPECGROUP tool to have a minimum

bin size of 100 counts per bin. For the *NuSTAR*/FPMA observations, the spectra were grouped with GRPPHA to have a minimum bin size of 50 counts per bin.

The spectral fitting was performed using XSPEC (v12.11.1; Arnaud, 1996). To model the spectra, we selected the 3–13 keV energy range for all *NuSTAR* spectra, except for the first spectrum (Obs.ID 80402308002) which was modeled in the 3–20 keV energy range. We restricted the energy range of the EPIC-pn spectra to 1–10 keV due to the domination of the background below 1 keV for this highly absorbed source. To quantify the hydrogen column density $N_{\rm H}$, we adopted the TBABS model with the interstellar-radiation abundance from Wilms, Allen, and McCray, 2000, and the photoionization cross-section model from Verner et al. (1996).

We modeled the EPIC-pn and FPMA spectra of Swift J1818.0−1607 simultaneously with two blackbodies plus a power-law component. We fixed the temperature and normalization of the first blackbody component to the aforementioned values derived from the diffuse emission fit (see Section 2.3.1 and Table 2.1). We also added a constant term between the two instruments to account for cross-calibration uncertainties. The constant was fixed to one for the *XMM–Newton*/EPIC-pn spectra and left free to vary for the *NuSTAR*/FPMA spectra. We linked the hydrogen column density between all the spectra and obtained $N_{\rm H}= (1.24 \pm 0.02) \times 10^{23}\,{\rm cm^{-2}}$. We found that the model fits the data with χ^2_ν=1.41 for 607 d.o.f. (see Figure 2.4). We note that the power-law component is required only for the spectrum at the outburst peak, i.e, the 2020 March 15 epoch, thus we did not include this component in the model for the remaining spectra. We obtained a power-law photon index of $\Gamma = 1.0 \pm 0.6$, which is consistent with the result reported by Esposito et al. (2020), $\Gamma = 0.0 \pm 1.3$. In Table 2.1, we list the best-fit parameters for the blackbody temperatures $kT_{\rm BB}$ and radii $R_{\rm BB}$, as well as the observed $F_{\rm X.obs}$ and unabsorbed $F_{\rm X.unabs}$ fluxes estimated in the 0.3–10 keV energy interval.

To supplement the *XMM–Newton* and *NuSTAR* observations, we initiated a *Swift*/XRT monitoring campaign of Swift J1818.0−1607. These pointings were used to sample the flux and spectral evolution of the magnetar over a longer time-span. We fit all the *Swift* spectra simultaneously with an absorbed blackbody model fixing $N_{\rm H}$ to the value obtained from the broad-band fit with *XMM–Newton* and *NuSTAR* data. Figure 2.5 shows the temporal evolution of the blackbody temperature and radius, and the 0.3–10 keV observed flux from the outburst onset on 2020 March 12 until 2021 October 24. The 0.3–10 keV observed flux of Swift J1818.0−1607 has shown a rapid decay since the outburst peak, from $\sim$1.4 $\times$ $10^{-11}\,{\rm erg\,s^{-1}cm^{-2}}$ to $\sim$6.6 $\times$ $10^{-13}\,{\rm erg\,s^{-1}cm^{-2}}$ after about 19 months (see Figure 2.5, bottom panel). Similarly, the blackbody radius decreased from $\sim$0.6 km to $\sim$0.3 km during the first seven months and then settled at an average value of $\sim$0.2 km (middle panel). We did not observe significant variability in the blackbody temperature, which attained a constant value of $\sim$1.1 keV over the whole monitoring campaign (top panel).

2.3.3 Burst Search

The sky region of Swift J1818.0−1607 has been extensively observed every year by the *INTEGRAL* satellite, starting from March 2003. We have carried out a search for bursts from Swift J1818.0−1607 using the data of IBIS/ISGRI, a coded mask imaging instrument with angular resolution of $\sim$12' and field of view of 29° $\times$ 29° (Ubertini et al., 2003). We selected all the public data with Swift J1818.0−1607 in the field of view obtained until April 2021. After removal of time intervals with high and variable background, this amounted to an exposure time of about 43 Ms. Most of the considered data (41 Ms) were obtained before the discovery outburst.

TABLE 2.1: Results of the joint fit of the *XMM–Newton* and *NuSTAR* spectra of Swift J1818.0−1607.

Instrument	Obs.ID	$F_{X,obs}$[a] ($\times 10^{-11}$ erg s^{-1}cm^{-2})	$F_{X,unabs}$[a] ($\times 10^{-11}$ erg s^{-1}cm^{-2})	kT_{BB} (keV)	R_{BB}[b] (km)	kT_{diff}[c] (keV)	$F_{X,diff}$[a] ($\times 10^{-12}$ erg s^{-1}cm^{-2})
XMM/EPIC-pn	0823591801[d1]	1.414 ± 0.003	3.036 ± 0.005	1.13 ± 0.01	0.56 ± 0.01	0.86 ± 0.02	1.93 ± 0.01
NuSTAR/FPMA	80402308002[d1]	-	-	-	-	-	-
XMM/EPIC-pn	0823593901[d2]	1.142 ± 0.003	2.417 ± 0.005	1.149 ± 0.007	0.501 ± 0.009	0.91 ± 0.03	1.59 ± 0.02
NuSTAR/FPMA	80402308004[d2]	-	-	-	-	-	-
NuSTAR/FPMA	80402308006	1.098 ± 0.005	2.264 ± 0.007	1.19 ± 0.01	0.44 ± 0.01	-	-
NuSTAR/FPMA	80402308008	0.652 ± 0.008	1.43 ± 0.01	1.14 ± 0.02	0.35 ± 0.02	-	-
NuSTAR/FPMA	80402308010	0.70 ± 0.01	1.42 ± 0.01	1.19 ± 0.03	0.36 ± 0.02	-	-
XMM/EPIC-pn	0823594001[d3]	0.448 ± 0.004	0.951 ± 0.007	1.13 ± 0.01	0.320 ± 0.008	0.96 ± 0.04	0.72 ± 0.02
NuSTAR/FPMA	80402308012[d3]	-	-	-	-	-	-
XMM/EPIC-pn	0823594201	0.416 ± 0.006	0.876 ± 0.007	1.17 ± 0.02	0.28 ± 0.01	0.89 ± 0.03	0.68 ± 0.02

[a] The fluxes are measured in the 0.3–10 keV energy range.
[b] The blackbody radius is derived assuming a source distance of 4.8 kpc.
[c] The fit of the diffuse emission is performed in the 2–7.5 keV energy range.
[d] These observations were fitted simultaneously.
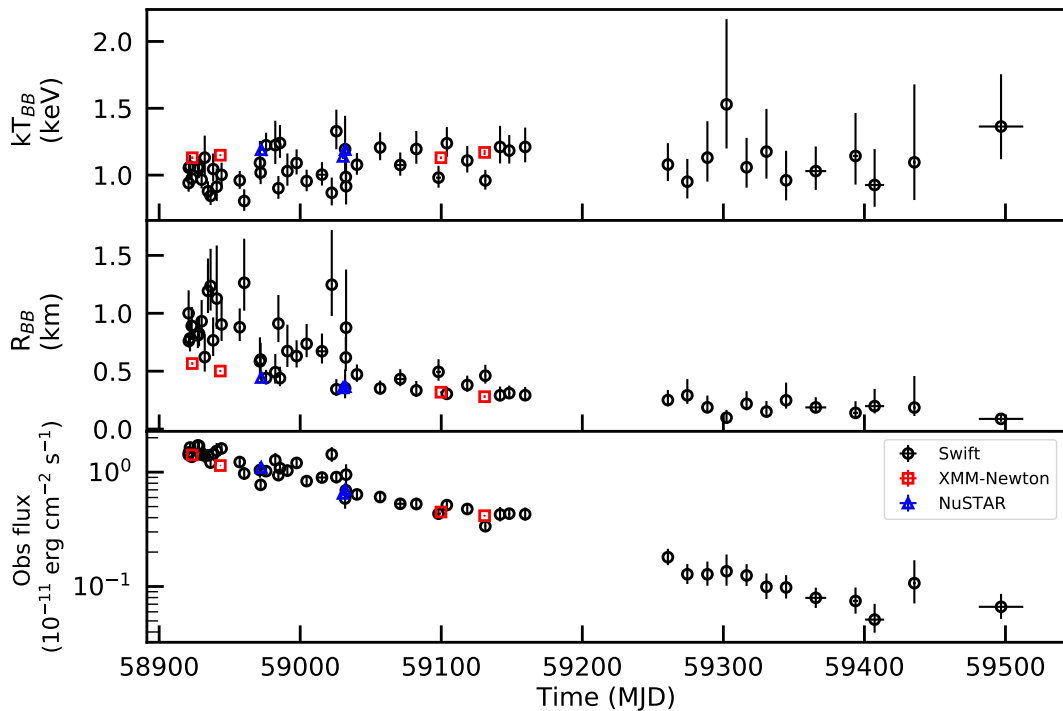
FIGURE 2.5: Temporal evolution of the blackbody temperature (top) and radius (middle). The latter is evaluated for a distance of 4.8 kpc (see Section. 2.3.2 for more details). The bottom panel shows the temporal evolution of the observed flux in the 0.3–10 keV energy range.

The burst search was done with the procedure described by Mereghetti et al. (2021). Briefly, this consists in a first screening of the light curves binned at eight logarithmically spaced timescales from 0.01 s to 1.28 s to select excesses with respect to the locally measured background count rate. The search is carried out in the nominal 20-100 keV, 30-100 keV and 30-200 keV energy ranges. In this first step, a threshold corresponding to $\sim$0.001 false positives per Science Window and time scale is adopted (*INTEGRAL* data are divided in Science Windows of a few ks duration). All these excesses are then examined through an imaging analysis, in order to reject the events caused by instrumental background or by bright sources located outside the field of view. This procedure led to the (re)-discovery of several bursts from other sources in the field of view, most of which originating from the magnetar SGR 1806-20 (Götz et al., 2006), located at about 5 degrees from Swift J1818.0−1607. However, no significant bursts were found from Swift J1818.0−1607, with a 3σ upper limit on the 20–200 keV fluence of about 10^{-8} erg cm^{-2}.

We also performed a burst search on *XMM–Newton* and *NuSTAR* data, using the method described by Borghese et al. (2020); (see also, e.g., Gavriil, Kaspi, and Woods 2004). We built the source barycentered light curves with time resolutions of 1/16, 1/32 and 1/64 s. We tagged as bursts the bins with a probability $<10^{-4}(NN_{\text{trials}})^{-1}$, where N is the total number of time bins in a given light curve and N_{trials} corresponds to the number of timing resolutions used in the search. No bursts were detected in the *XMM–Newton*/EPIC-pn light curves, while we list the epochs of the bursts found in the *NuSTAR* datasets in Table 2.2. Due to the low photon statistics, we were unable to model the corresponding spectra.
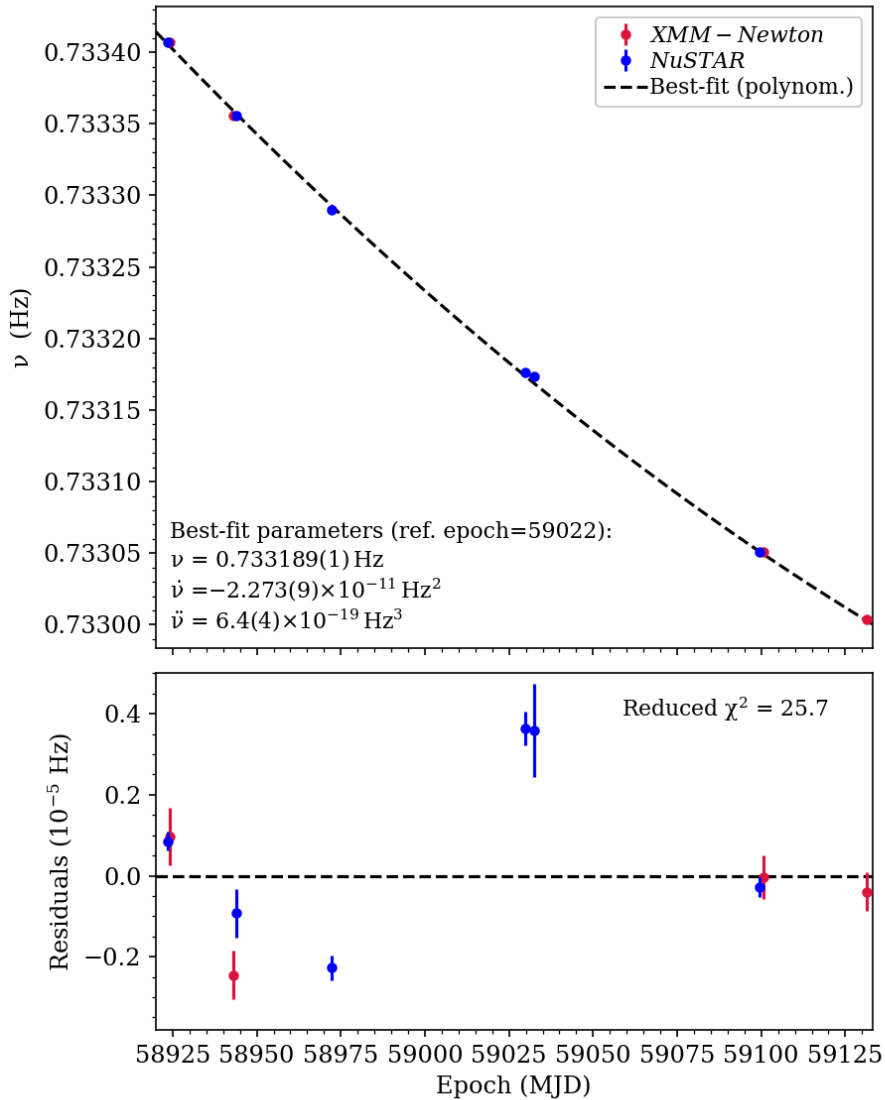
FIGURE 2.6: `TEMPO`-derived values of the spin frequency, ν, in each observations. The epochs of *XMM–Newton* and *NuSTAR* observations are shown as red and blue points. Error bars correspond to the 1-σ uncertainties reported by `TEMPO`. Black dashed/dotted lines are the best-fit models for $\nu(t)$ (see text in Section 2.3.4). As evidenced by the large reduced χ^2 values we measured (provided in the top-right corner of the bottom panels), the $\nu(t)$ solutions poorly fit the data. This is explained by the large timing noise present in Swift J1818.0−1607 and the simplicity of our models.

TABLE 2.2: Log of X-ray bursts detected in the *NuSTAR* light curves.

| Obs.ID | Burst epoch | | Fluence |
	YYYY-MM-DD hh:mm:ss (TDB)		(counts)
80402308002	2020-03-15	05:25:59	10
		05:45:51	8
80402308002	2020-04-05	04:12:22	7
80402308002	2020-05-03	18:05:07	22

In Table 2.2, we report the properties for the bursts detected in the *NuSTAR* light curves. In the table, the epochs are referred to the Solar system barycenter, the fluence refers to the 3–79 keV range and the duration has to be considered as an approximate value. We estimated it by summing the 15.625-ms time bins showing enhanced emission for the structured bursts, and by setting it equal to the coarser time resolution at which the burst is detected in all the other cases. Therefore, it has to be considered as an approximate value. Except for burst 1 on 2020 May 3 (125 ms), all the remaining bursts have a duration of 62.5 ms.

2.3.4 Timing Analysis

For the timing analysis of Swift J1818.0−1607, we used the *XMM–Newton* and *NuSTAR* data sets as shown in Table A.1. For *NuSTAR*, we applied the clock corrections with up-to-date clock files and combined the FPMA and FPMB events files for each observation. For both *XMM–Newton* and *NuSTAR* data sets, we referred the photon arrival times to the Solar system barycentre adopting the source coordinates by Esposito et al. (2020), i.e., R.A.= 18^h 18^m 00^s.16, Dec.= −16°07′53.2″ (J2000.0), and the JPL planetary ephemeris DE200.

In an attempt to derive a phase-coherent timing solution, we first used a provisional ephemeris to assign the rotational phase of each photon in the data sets through an unbinned maximum likelihood method (Livingstone et al., 2009; Ray et al., 2011). This was done with the PHOTONPHASE tool of the PINT[5] pulsar timing package (Luo et al., 2021a). To account for the different energy bandpass, we created two separate template profiles for the *XMM–Newton* and *NuSTAR* observations by folding the strongest detection in their respective dataset. Two-component Gaussian models were fitted to the binned profiles to construct smoothed standard templates. Times of arrival (TOAs) and associated errors were then computed for a number of sub-integrations from the predicted photon-phase information, using the smoothed profile templates to define the fiducial point in pulse phase.

Using the TEMPO timing software (Nice et al., 2015a), we then tried to obtain a coherent timing solution that simultaneously fits the *XMM–Newton* and *NuSTAR* TOAs. Similar to the post-outburst spin evolution seen in other magnetars (see review by Kaspi and Beloborodov 2017), we also observed significant variability in the spin-down behaviour of Swift J1818.0−1607, particularly a large jump in spin frequency between MJDs 58972 and 59030. This could be an evidence for the presence of discrete timing events and/or strong timing noise, which is consistent with the erratic timing behavior reported by Champion et al. (2020a), Hu et al. (2020) and Rajwade et al. (2022). To account for the large spin variability of Swift J1818.0−1607 we included up to four spin frequency derivatives in our timing model. However,

---

[5]PINT:
https://github.com/nanograv/PINT

due to the sparsity of our observations, we encountered phase-count ambiguity during the phase-connection procedure which could not be resolved even with the aid of automated algorithms such as Dracula[6] (Freire and Ridolfi, 2018).

Nevertheless, we examined the rotational evolution of Swift J1818.0−1607 by measuring the spin frequency ν of the magnetar in each observation using the computed TOAs and TEMPO. The resulting ν values are listed in Table 2.3, and shown in Figure 2.6. We modeled long-term average spin evolution $\nu(t)$ with a second-order polynomial function (dashed line in Figure 2.6) and the resulting best-fit spin-down rate on MJD 59022 is $\dot{\nu} = -2.273(9) \times 10^{-11}\,\mathrm{Hz}^2$. However, this simple model poorly fits the data (χ_ν^2 of 25.7), and because of the large time gaps between our observations, we cannot determine whether the large residuals are caused by an unmodeled timing anomaly (glitch) or timing noise.

TABLE 2.3: Best-fit spin frequencies calculated with TEMPO in individual *XMM–Newton* and *NuSTAR* observations. Numbers in parentheses are the 1σ uncertainties on the last digit reported by TEMPO.

Instrument/Obs.ID	Ref. Epoch (MJD)	ν (Hz)
XMM/0823591801	58923.40	0.7334073(7)
NuSTAR/80402308002	58923.40	0.7334068(2)
XMM/0823593901	58943.30	0.733356(6)
NuSTAR/80402308004	58944.00	0.7333558(6)
NuSTAR/80402308006	58972.40	0.73329(3)
NuSTAR/80402308008	59030.40	0.7331763(4)
NuSTAR/80402308010	59031.90	0.733173(1)
NuSTAR/80402308012	59099.50	0.7330509(3)
XMM/0823594001	59099.80	0.7330506(5)
XMM/0823594201	59130.60	0.7330035(5)

We also note that we attempted to fold the *XMM–Newton* and *NuSTAR* data using the timing ephemerides provided by Champion et al. (2020a), Hu et al. (2020) and Rajwade et al. (2022). These ephemerides fail to predict the rotational phase of the source during our *XMM–Newton* and *NuSTAR* observations, with one exception: the solution from Rajwade et al. (2022) extrapolates well the rotation of Swift J1818.0−1607 during our last *XMM–Newton* observation in 2020 September (MJD 59130). This is not surprising considering that large variations in spin down are reported by Champion et al. (2020a), Hu et al. (2020) and Rajwade et al. (2022) for MJDs before ∼59100, after which the spin down appears to stabilize around a mean value of $\dot{\nu} \sim -1.37 \times 10^{-11}\,\mathrm{Hz}^2$ (Rajwade et al., 2022).

Considering our limited and sparse dataset, as well as the poorly-understood impact of magnetospheric processes on spin behaviour associated with magnetar outbursts, we do not attempt to further model, quantify and/or interpret the timing properties of Swift J1818.0−1607 in the *XMM–Newton* and *NuSTAR* data.

To study possible changes in the shape and amplitude of the X-ray pulse profile with photon energy, we extracted energy-resolved pulse profiles from the EPIC-pn data sets in three energy bands: 0.3–3, 3–5 and 5–10 keV (see Figure 2.7). This is performed by folding the time series on the spin periods reported in Table 2.3. The rows in Figure 2.7 show the evolution of the pulse profile in time, while the columns show their evolution in energy. For each panel, we also reported the corresponding values of the pulsed fraction (PF) that is defined as:

---

[6]Dracula:
https://github.com/pfreire163/Dracula
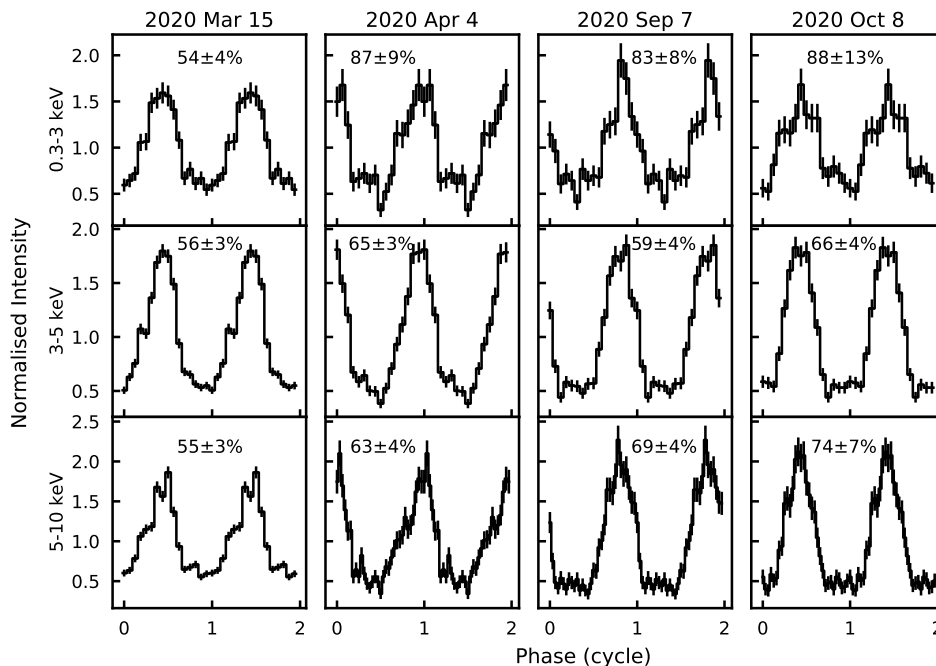
FIGURE 2.7: Energy-resolved pulse profiles of Swift J1818.0−1607 extracted from the four *XMM–Newton* data sets presented in this work. The profiles were obtained by folding the light curves using the frequencies reported in Table 2.3. The corresponding pulsed fraction values are reported in each panel. Two cycles are shown for clarity.

$$PF = \frac{(CR_{\max} - CR_{\min})}{(CR_{\max} + CR_{\min})}, \tag{2.1}$$

where $CR_{\max}$ and $CR_{\min}$ are the count rates at the maximum and minimum of the pulse profile. For a given energy band the PF increased in time from March to October 2020 epochs. Additionally, we also estimated the PF for the 0.3–10 keV energy interval: it increased with time, from $(53\pm2)\%$ to $(64\pm3)\%$ between March and October 2020.

2.3.5 Radio observations

We observed Swift J1818.0−1607 with the *VLA* under project code 21A-111, with the aim to detect the radio counterpart of Swift J1818.0−1607 as well as the presence of any diffuse radio emission around the source. The *VLA* observation was performed on 2021 March 22 (MJD 59295) with the telescope on source between 14:58 and 15:38 UT. The data were carried out in the *S*-band, at the central frequency of 3 GHz and a total bandwidth of 2 GHz (comprised of sixteen 128-MHz sub-bands made up of sixty-four 2-MHz channels). 3C 286 was used for bandpass and flux calibration, while the nearby (6.5° away) source J1822−0938 was used for phase calibration.

Raw data were flagged for radio frequency interference (RFI), calibrated, and imaged following standard procedures with the Common Astronomy Software Application CASA (v.5.1.2; THE CASA TEAM et al., 2022). We first imaged the field with a Briggs robust parameter of zero to balance sensitivity and resolution, and reduce image side-lobes. We detected the radio counterpart of Swift J1818.0−1607 as a
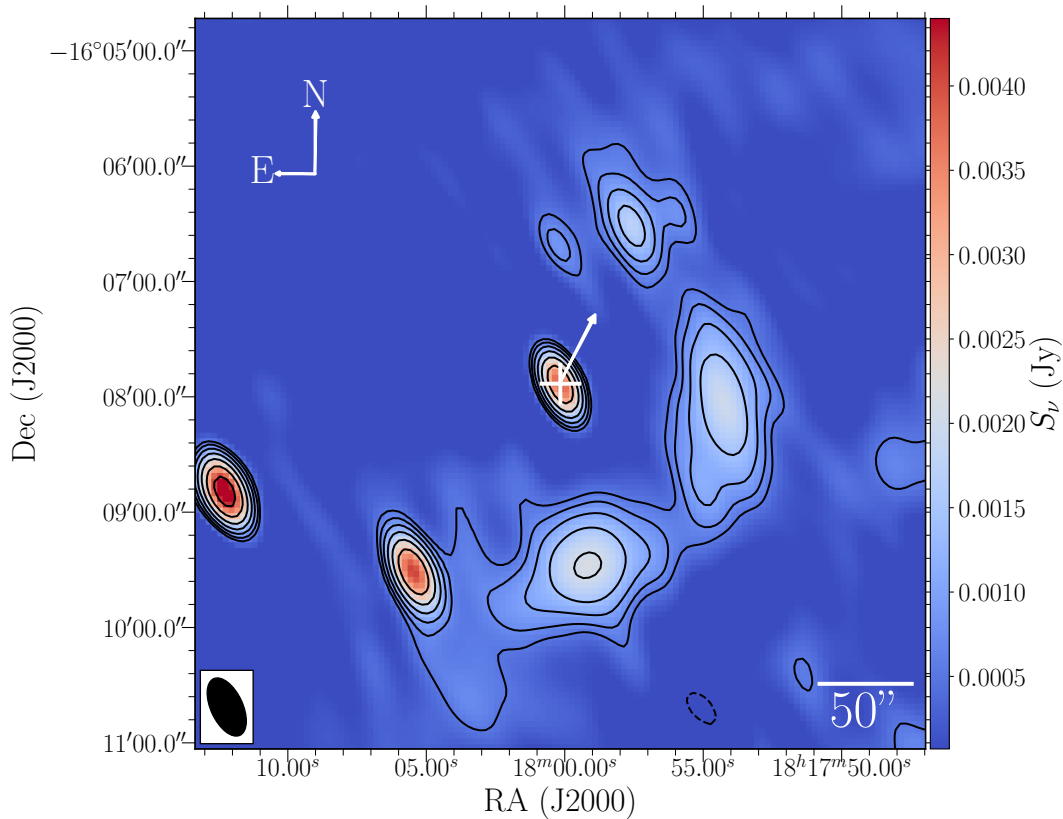
FIGURE 2.8: 3 GHz VLA radio image of Swift J1818.0−1607 and the surrounding diffuse emission. This image was created using a natural weighting scheme to ensure that any diffuse emission was retained. The position of Swift J1818.0−1607 is marked by the white cross. The white arrow originating from the source position indicates its proper motion multiplied by a factor of 5000 (Ding et al., 2022). Contours are drawn at intervals of $\sqrt{2^n} \times$ rms, where $n = 5, 6, 7, 8, ...$ and the image rms (near the source region) was 90 μJy/beam. The negative contour at the bottom of the figure is marked by dashed lines. The black-filled ellipse in the bottom-left corner represents the shape and size of the synthesized beam. Swift J1818.0−1607 is clearly detected as a bright point source, which is surrounded by a half ring-like structure of diffuse emission.

point source with peak flux density of S_ν, of 4.38 ± 0.05 mJy, where ν is the observing frequency (3 GHz). We also measured an in-band spectral index, α, of -2 ± 1, where $S_\nu \propto \nu^\alpha$.

We also imaged the field with a Briggs robust parameter of two (corresponding to a natural weighting) to emphasise any diffuse emission in the field (see, Figure 2.8), although this did increase the image noise (to ~ 0.09 mJy/beam). We detected a relatively bright (peaking at ≈ 2.2 mJy/beam) half-ring of diffuse emission located $\sim 90''$ to the west of Swift J1818.0−1607. The diffuse structure exhibits a radio spectral index between $-1(\pm 1)$ and $-3(\pm 1)$. Unfortunately, from the radio image alone, we are unable to unambiguously connect this diffuse emission to Swift J1818.0−1607 where, instead, the emission may be related to another source in the field (in particular the second bright source to the south-east of Swift J1818.0−1607). However, taking into account the shape around Swift J1818.0−1607 we lean towards the scenario in which this diffuse radio emission is related to the magnetar. Further radio observations are planned/on-going to identify the nature and behaviour of this emission.

2.4 Discussion

We have presented the evolution of the X-ray spectral and timing properties of the magnetar Swift J1818.0−1607 following its first outburst with onset on 2020 March 12, as well as a VLA radio observation of the field. The X-ray monitoring campaign covered ∼19 months of the outburst decay, allowing us to characterize accurately the behavior of the source over a long time span.

2.4.1 Long-term light curve modeling

The 0.3–10 keV luminosity reached a peak value of $\sim 9 \times 10^{34}$ erg s^{-1} only a few minutes after the detection of the short burst that triggered *Swift*/BAT on 2020 March 12 (Evans et al., 2020). Then, it decreased down to $\sim 3 \times 10^{33}$ erg s^{-1} after 575 days. To study the post-outburst luminosity decay, we modeled the temporal evolution of the 0.3–10 keV luminosity with a phenomenological model consisting of an exponential function:

$$L(t) = A \exp[-(t - t_0)/\tau] \,, \tag{2.2}$$

where t_0 is the epoch of the outburst onset fixed to MJD 58920.8866 (2020 March 12, 21:16:47 UTC; Evans et al. 2020), and the *e*-folding time τ can be interpreted as the decay timescale of the outburst. The fit resulted in $\tau = 153 \pm 1$ days for a reduced $\chi^2_\nu = 0.8$ for 59 d.o.f assuming an uncertainty of 20% on all the nominal values of the luminosity. We can compare this result with that obtained by Hu et al. (2020), who modeled the first ∼100 days of the luminosity temporal evolution using a double exponential function, giving *e*-folding timescales of $\tau_1 = 9 \pm 2$ and $\tau_2 = 157 \pm 13$ days. The latter reflects the decay trend on a longer timescale, and is fully consistent within the uncertainties with the value derived in this work using data covering the first ∼19 months of the outburst. We then integrated the best-fitting model over a time range spanning from the outburst onset (March 2020) to the last epoch of our observing campaign (October 2021), and estimated a total energy released in the outburst of $\approx 10^{42}$ erg. The reported results of the decay timescale and the released energy of the outburst of Swift J1818.0−1607 are in agreement with those derived by Coti Zelati et al. (2018) for magnetars showing major outbursts (e.g., SGR 1833–0832) and follow the correlation trend between these two quantities, implying that the decay pattern of this outburst is similar to that observed for other magnetar outbursts.

2.4.2 Timing analysis

We attempted to derived a phase-connected timing solution from the *XMM–Newton* and *NuSTAR* dataset, which covered a 7-months period from 2020 March to October. However, the sparsity of the observations lead to phase ambiguity and prevented us from identifying the correct timing model for the source. During the monitoring campaign, the spindown rate $\dot{\nu}$ of the source fluctuates but is overall increasing with time. Despite being poorly constrained, the spin evolution we observe is consistent with the timing results obtained by Rajwade et al. (2022) from the radio monitoring of the source after 2020 July, although we note a more rapid slowdown over the (earlier) time coverage of our X-ray data. At the reference epoch (MJD) 59022, we estimate a characteristic age $\tau_c \sim 510$ yr that is consistent with other measurements reported shortly following the onset of the outburst (e.g., Champion et al. 2020a;
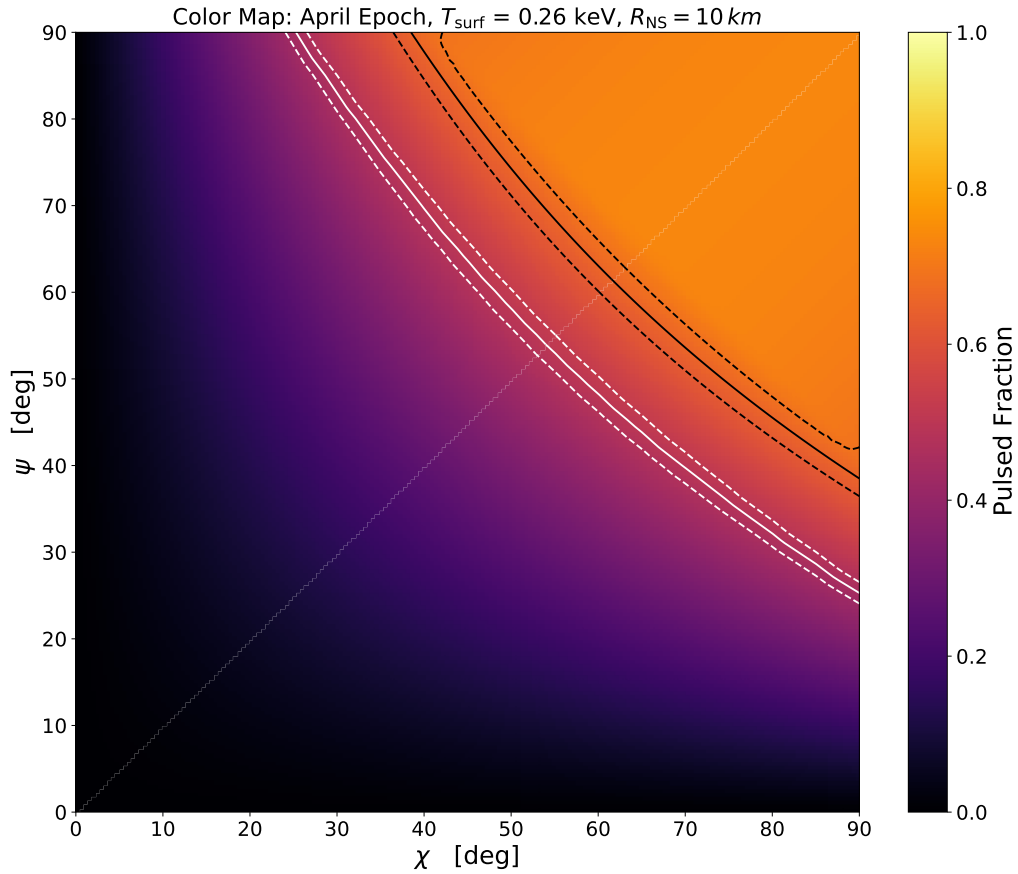
FIGURE 2.9: Constraints on the emission geometry of Swift J1818.0−1607 based on the PF measured in April 2020. The color scale represents the 0.3–10 keV PF at different angles calculated by employing a surface temperature of $kT_{star} = 0.26$ keV. The black lines represent the measured value (PF = $66 \pm 3\%$). The white lines represent the same contours calculated considering only the flux from the hot-spot, neglecting the contribution from the remaining of the star.

Hu et al. 2020) but younger than the late-time radio measurements by Rajwade et al. (2022, i.e., $\sim 860\,\mathrm{yr}$) which is more likely to reflect the true spindown rate of the magnetar. Despite the torque variability of Swift J1818.0−1607 it remains clear that this object is one of the youngest neutron stars in the Galaxy. However, a targeted monitoring campaign of the source during its quiescent state is needed to determine a more accurate secular spin-down rate.

2.4.3 Constraining the emission geometry via pulsed-fraction modeling

We constrain the emission geometry of Swift J1818.0−1607 namely the orientation of the hot spot with respect to the line of sight and the rotational axis, by comparing the PF observed in the *XMM–Newton* data to a set of simulated PFs calculated using the approach described by Perna, Heyl, and Hernquist (2001) and Gotthelf, Perna, and Halpern (2010).

We define a temperature map on the stellar surface, characterized by a uniform background temperature plus a single hot spot with a Gaussian temperature profile. The hot spot is oriented at an angle χ with respect to the star's rotational axis. After defining our line of sight as orientated at an angle ψ with respect to the rotational axis, we calculate the observed phase-resolved spectra by integrating the local blackbody emission on the visible portion of the stellar surface. We take into account the gravitational light bending by approximating the ray-tracing function (Pechenick, Ftaclas, and Cohen, 1983; Page, 1995) with the formula derived by Beloborodov (2002). The interstellar medium absorption was also taken into account.

For each combination of (χ, ψ) angles in the range $[0°, 90°]$, we integrate the phase-resolved spectra in the energy range 0.3–10 keV to obtain a light curve, whose maximum and minimum values allow us to calculate the PF, according to Eq. (2.1).

We performed the analysis using the hot-spot parameters measured in April 2020 epoch ($kT_{BB} = 1.15\,\mathrm{keV}$ and $R_{BB} = 0.50\,\mathrm{km}$) and October 2020 epoch ($kT_{BB} = 1.17\,\mathrm{keV}$ and $R_{BB} = 0.28\,\mathrm{km}$). We used two different setups: a setup where we consider only the hot-spot contribution to the flux, neglecting the rest of the surface, and another setup, where we consider also the emission from the remaining surface, whose temperature is set as $kT_{\mathrm{star}} = 0.26\,\mathrm{keV}$ (this latter setup describes a case where the contribution of the stellar background to the flux is maximal). This value is an upper limit estimated by assuming uniform blackbody emission from the entire stellar surface (we have adopted a stellar radius of 10 km) and taking into account the effects of interstellar absorption (we fixed the absorption column density to $N_{\mathrm{H}} = 1.24 \times 10^{23}\,\mathrm{cm}^{-2}$): it is the one that gives an observed flux consistent with the count-rate upper limits derived using *XMM–Newton* at pre-outburst epochs (0.008 counts s^{-1} at 3σ; see Esposito et al. 2020).

Figure 2.9 shows the PF variation in the $\chi - \psi$ plane. The color scale represents the PF calculated using the hot-spots parameters derived from the April epoch with the second setup, where the contribution of the whole surface is considered. The black lines represent the constant PF contour equivalent to the measured value for this epoch, i.e., PF = $66 \pm 3\%$. The white lines instead represent the same contour, but derived from the first setup, where only the hot spot emits. It is worth noticing that including the emission from the entire surface causes a shift of constant PF lines toward the upper-right corner. The reason is that this additional contribution acts in the direction of decreasing the PF, so that in order to keep the PF at the same value, we have to move towards higher values of χ and ψ. In this way, the hot-spot+surface and the only-hot-spot setups determine an upper and lower limit, respectively, in the $\chi - \psi$ plane. These limits constrain the geometry of the source.

Since the result for the April epoch are more constraining than those for the October epoch, we report here only the former results. The geometrical constraints that we derive through modelling the rotation of the brightest hot spot cannot be directly compared with those usually derived via radio polarimetric observations (Johnston and Kerr, 2018). During a magnetar outburst, the magnetosphere is very dynamic, and as a consequence the radio emission is highly variable in terms of intensity, pulse profile, polarization position angle (PA) on timescales ranging from hours to days (see Lower et al. 2020b). For this reason, PA swings during magnetar outbursts are not a direct trace of the system geometry. On the other hand, the surface hot spot (which may or may not be located close to the magnetic pole) cannot move during the outburst and is a better proxy for the system geometry. For sources undergoing multiple outbursts, the properties of the heated spots may differ from event to event depending on the exact position and extension of the bundle that triggers that particular outburst. However, once formed, the hot spot cools down but does not move on the surface as the outburst decays.

2.4.4 Spectral evolution of the source and diffuse emission

We detected diffuse emission around Swift J1818.0−1607 in the *XMM– Newton*/EPIC-pn observations, which confirms the result previously obtained by Esposito et al., 2020. Extracting the surface brightness profiles, we found that the diffuse emission extends within $50'' - 110''$ (Figure 2.2, top panel). The spectra of this component are well described by a single blackbody model (Figure 2.3). The best-fitting values show that the temperature of the diffuse emission kT_{diff} does not vary in time, while we see a clear decrease in the flux $F_{\mathrm{X.diff}}$ of $\approx 35\%$ between March and October 2020. Since an angular scale of $110''$ correspond to an extent of more than 8 light years at a distance of 4.8 kpc, we can explain this variability in such a short time only by invoking a projection effect, such as in the case of a dust-scattering halo.

The study of the long-term spectral evolution of Swift J1818.0−1607 from EPIC-pn and FPMA observations showed that the X-ray spectrum is well described by a single blackbody, except for the epoch close to the outburst onset, where a power law was required to model the emission. To improve the sampling of the long-term magnetar flux evolution and trace the blackbody radius and temperature, we complemented these data sets with additional observations from the *Swift*/XRT telescope (see Table A.1). Figure 2.5 shows the temporal evolution of the X-ray flux, the blackbody temperature and radius for Swift J1818.0−1607.While the temperature remained constant around 1 keV across the time span covered by the observations, the observed 0.3–10 keV flux as well as the radius of the emitting region showed an exponentially decreasing trend.

To compare the decay rate of the 0.3–10 keV flux of the thermal and non-thermal components of Swift J1818.0−1607 in the early stages of the outburst, we evaluated the rate of the flux decrease separately for the two components over the period from March to April 2020. In the case of the *XMM–Newton+NuSTAR* observations performed in April 2020, we added a power-law component in the spectral modeling, fixing the index at the value measured during the March epoch ($\Gamma = 1.04$). We found that, between the two epochs, the flux decay of the power-law component is about two times faster than that of the blackbody component.

2.4.5 Point-like and diffuse radio emission

Large radio flux variability was observed from Swift J1818.0−1607 during its outburst evolution, in line with what is typically seen in other radio-loud magnetars. The point-like continuum radio emission observed from Swift J1818.0−1607 in our VLA observations had a flux density of 4.38 ± 0.05 mJy at 3 GHz. Comparing this flux with the pulsed flux evolution reported by Rajwade et al. ([2022](#)) at 1.4 GHz, the source continuum emission appears to be compatible with the reported pulsed flux assuming a flat spectrum between the two bands. The different bands, the large variability of the radio spectrum of this object, and the non-simultaneous flux measurements do not allow us to draw any strong conclusion about the presence of a non-pulsed continuum radio emission (i.e. a pulsar wind nebulae component).

Recent preliminary indication of a proper motion detected by VLBA (Ding et al., [2022](#)) hints to a motion of the source in the N-W direction, which would be toward the higher end of the observed radio ring-like structure.

The presence of X-ray and radio diffuse emission on similar scales ($\sim 90''$) might, in the first place, lead to a tentative association of these two emission regions. However, the variability we observe in the X-ray diffuse emission, its relatively soft X-ray spectrum, as well as the large N_H we measure along the line of sight, lead us to interpret the X-ray diffuse emission as a dust scattering halo which is not expected to have radio counterparts. In addition, we stress that it is also possible that the diffuse radio emission is unrelated to Swift J1818.0−1607.

If it is related to Swift J1818.0−1607, the radio diffuse emission with its semi-circular and patchy appearance is similar to that observed in some supernova remnants. At a distance of 4.8 kpc, the $\sim 90''$ structure translates to a physical dimension of ~ 2 pc. Assuming that this radio emission comes from the supernova remnant associated with the magnetar, we attempt to study its evolutionary status. The evolutionary path of a supernova remnant can be described in the radio domain by the $\Sigma - D$ diagram (see; Urošević, [2020](#), Figure. 3), where Σ is the radio surface brightness and D is the diameter. We used the information obtained from our radio observation to assess the position of the remnant in this diagram and the associated evolutionary status.

The integrated flux density of the nebula is $\sim 3.6 \times 10^{-2}$ Jy at 3 GHz, from which we obtained a surface brightness at 1 GHz of $\Sigma \sim 1.1 \times 10^{-21}$ W m $^{-2}$ Hz $^{-1}$ sr $^{-1}$ assuming a spectral index α of 0.5 (corresponding to the mean radio spectral index of the observed Galactic supernova remnants; e.g. Dubner and Giacani [2015](#)). Assuming a distance of 4.8 kpc, this value would imply that the supernova remnant lies in the left corner of the $\Sigma - D$ diagram. Such a position is relative to a free expansion in an extremely-low density medium, which seems rather untenable (a similar scenario is discussed and rejected by Filipović et al. [2022](#) for the supernova remnant J0624–6948). On the other hand, if the source distance is 8.1 kpc (Champion et al., [2020a](#)), the supernova remnant would lie in the lower right corner of the diagram, meaning that it is in full Sedov phase. We also used the equipartition (eqp[7]) calculator (Urošević, [2020](#))

to estimate the magnetic field strength by considering a distance of the remnant of 8.1 kpc and a $\alpha = 0.5$. We obtained $B \sim 40$ μG, which is consistent (in terms of order of magnitude) with the value obtained for other well-studied supernova remnants in the same evolutionary phase (see the case the middle-age Cygnus Loop supernova remnant Loru et al., [2021](#)).

---

[7]Equipartition calculation for supernova remnants:
https://poincare.matf.bg.ac.rs/~arbo/eqp/

Further radio observations are planned to disentangle the spectrum of this diffuse radio emission, and possibly confirm its remnant nature (the corresponding results will be presented in a future paper).

3 An X-ray and radio view of the 2022 reactivation of the magnetar SGR J1935+2154

3.1 The Galactic Magnetar SGR J1935+2154

SGR J1935+2154 was discovered in 2014 July 5, when the Burst Alert Telescope (BAT) on board the *Neil Gehrels Swift Observatory* (*Swift*; Gehrels et al., 2004) detected a short burst (Stamatikos et al., 2014). Follow-up observations enabled the measurement of the source spin period $P \sim 3.24\,\mathrm{s}$ and spin-down rate of $\dot{P} \sim 1.43 \times 10^{-11}\,\mathrm{s\,s^{-1}}$. These values resulted in a surface dipolar magnetic field $B \sim 2.2 \times 10^{14}\,\mathrm{G}$ at the equator, confirming the magnetar nature of the source (Israel et al., 2016b). The distance to the magnetar has been the focus of various works. Some of these studies associate SGR J1935+2154 with the supernova remnant G57.2+0.8, for which distances of 6.6±0.7 kpc (Zhou et al., 2020) and ≤ 10 kpc (Kozlova et al., 2016) have been derived. On the other hand, other studies reported a distance of $4.4^{+2.8}_{-1.3}$ kpc, based on the analysis of an expanding dust-scattering ring associated with a bright X-ray burst (Mereghetti et al., 2020).

Since its discovery, SGR J1935+2154 has been a very active source, experiencing multiple outbursts in 2015, 2016 (twice) and 2020 (see e.g., Younes et al., 2017; Borghese et al., 2020), as well as frequent bursting episodes (e.g., Lin et al., 2020). Additionally, one day after the 2020 reactivation, a short and very bright, double-peaked radio burst (known as FRB 200428) temporally coincident with a hard X-ray burst was observed (CHIME/FRB Collaboration et al., 2020; Bochenek et al., 2020; Mereghetti et al., 2020; Ridnaia et al., 2021; Tavani et al., 2021; Li et al., 2021). This was the first time SGR J1935+2154 was detected in the radio band. The radio burst showed properties similar to those of Fast Radio Bursts (FRBs). FRBs are bright radio pulses characterised by a millisecond duration and dispersion measures greater than the Galactic one, suggesting an extragalactic origin (for a detailed review see Petroff, Hessels, and Lorimer, 2022, and references therein). The progenitor engines of these FRBs are still broadly discussed in the literature. However, the detection of FRB-like bursts from SGR J1935+2154 supports the scenario that magnetars can power at least a subgroup of FRBs.

On 2022 October 10–11, multiple short X-ray bursts were detected from SGR J1935+2154 by *INTEGRAL*, *Swift*/BAT and other X-ray satellites indicating a reactivation of the source (e.g., Mereghetti et al., 2022; Palmer, 2022; Ibrahim et al., 2022). Following this bursting activity, *NICER* began observing the source and measured a persistent X-ray flux that was about one order of magnitude higher than the quiescent level (Younes et al., 2022b). A new outburst had begun. Similarly to the 2020 outburst, radio bursts with X-ray counterparts were also observed during the initial stage of this outburst (e.g., Maan et al., 2022; Pearlman and Chime/Frb Collaboration, 2022; Younes et al., 2022a), but none as bright as FRB 200428.
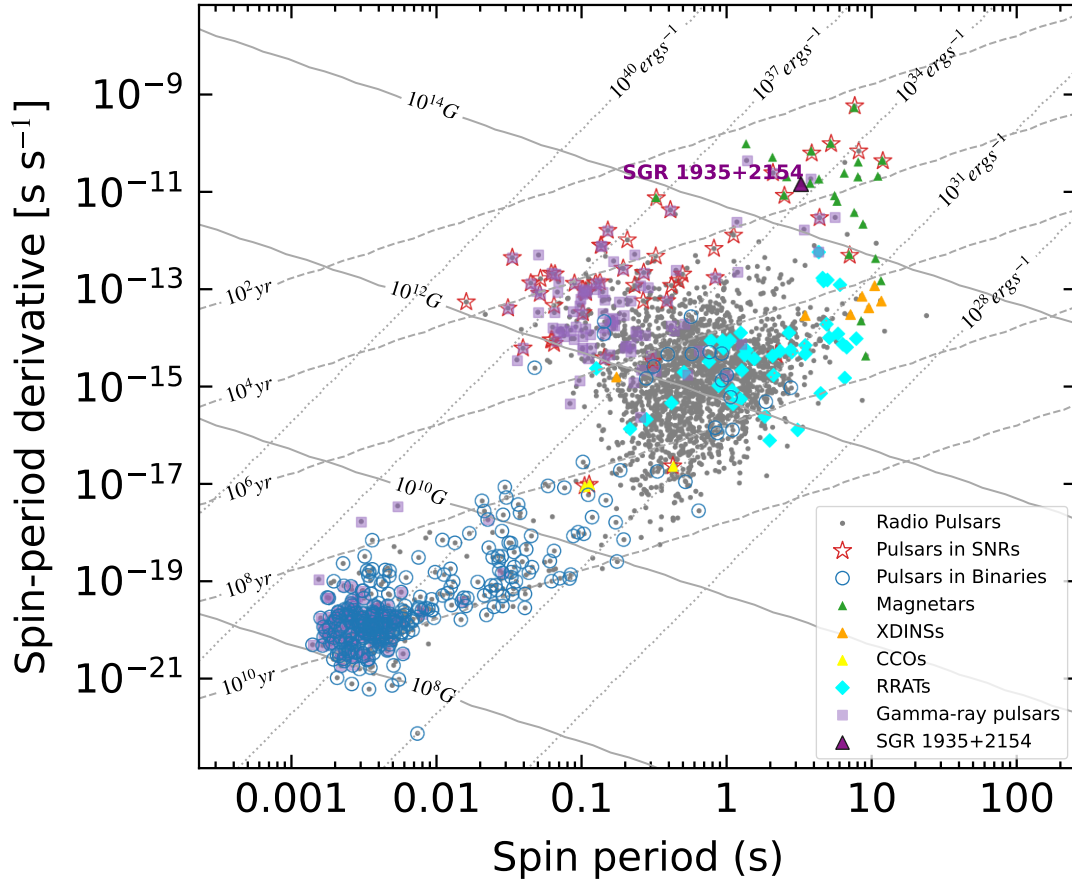
FIGURE 3.1: The $P\dot{P}$ diagram highlights SGR J1935+2154, marked in purple, among various pulsars. It also features radio pulsars (grey dots), RRATs (cyan diamonds), gamma-ray pulsars (purple squares), XDINSs, CCOs, and shows lines for characteristic age, magnetic fields, and spin-down luminosity. Adapted from (with permission; Ronchi, 2024) and updated with data from the ATNF pulsar catalogue (version: 2.2.0; Manchester et al., 2005).

Here, we report on the X-ray persistent and bursting emission properties of SGR J1935+2154 during the first weeks of the most recent active period, as well as on our searches for single pulses and pulsed emission in quasi-simultaneous radio observations. We first summarise the X-ray data analysis procedure in Section 3.2. We then present the timing and spectral analysis, as well as a search for short bursts in Section 3.3. In Section 3.4, we describe our radio observations. Finally, Section 3.5 presents a discussion of our findings.

3.2   X-ray observations and data reduction

We report on nearly simultaneous *XMM–Newton* and *NuSTAR* observations, carried out between 2022 October 15 and 22. Data reduction was carried out using HEASOFT package (v6.31; NASA High Energy Astrophysics Science Archive Research Center - HEASARC, 2014) and the Science Analysis Software (SAS[1], v.19.1.0 Gabriel et al. 2004) with the latest calibration files.

---

[1]SAS:
https://www.cosmos.esa.int/web/xmm-newton/sas

Throughout this work, we adopted the coordinates reported by Israel et al. (2016b), i.e. R.A. = $19^h34^m55^s.598$, decl. = $+21°53'47''.79$ (J2000.0), and the JPL planetary ephemeris DE 200 to convert the photon arrival times to the Solar system barycenter. Additionally, to be consistent with our previous works (e.g., Borghese et al., 2022), we adopted a distance of 6.6 kpc (Zhou et al., 2020) and quote all uncertainties at a 1σ confidence level (c.l.).

3.2.1 *XMM–Newton*

XMM–Newton observed SGR J1935+2154 twice with the European Photon Imaging Camera (EPIC), for an exposure time of ~ 40 ks and ~ 50 ks for the first (ID:0902334101, between 2022 October 15, 19:48:48 UTC, and October 16, 12:06:17 UTC) and the second (ID:0882184001, 2022 October 22 between 03:22:56 and 22:12:09 UTC) observation, respectively. For each observation, the EPIC-pn (Strüder et al., 2001) was set in Small Window mode (time resolution of 5.7 ms) while the EPIC-MOS1 and EPIC-MOS2 (Turner et al., 2001) were set in Full Window mode (time resolution of 2.6 s) and Timing mode (time resolution of 1.75 ms), respectively. Following standard procedures, we filtered the event files for periods of high background activity, resulting in a net exposure of 39 ks and 41 ks for the first and the second pointings. No pile-up was detected. The source counts were extracted from a circle of radius $30''$ centered on the source and the background level was estimated from a 60-arcsec-radius circle far from the source, on the same CCD. In this study, our primary focus was on data collected with the EPIC-pn, because of its higher counting statistics owing to its larger effective area compared to that of the two MOS. However, we verified that the MOS data yielded consistent results.

3.2.2 *NuSTAR*

SGR J1935+2154 was observed twice with *NuSTAR* (Harrison et al., 2013): the first time between 2022 October 18, 21:51:09 UTC, and October 20, 22:21:09 UTC (ID:80702311002, on-source exposure time $\sim$50 ks); the second time between 2022 October 22, 22:21:09 UTC, and October 24, 03:11:09 UTC (ID:80702311004, on-source exposure time $\sim$51 ks). Source photons were accumulated within a circular region of radius $100''$. A similar region centered on a position uncontaminated by the source emission was used for the extraction of the background events. The light curves, the spectra and the corresponding response files for the two focal plane detectors, referred to as FPMA and FPMB, were extracted using the NUPRODUCTS script.

3.2.3 *INTEGRAL*

We searched the *INTEGRAL* archive for data obtained simultaneously with *XMM–Newton* and *NuSTAR* observations. This resulted in 23 pointings where SGR J1935+2154 was in the field of view of the IBIS coded mask imaging instrument. These pointings cover about 60% of the first *XMM–Newton* observation (from October 15 at 18:51 to October 16 at 04:47 UTC) and 15% of the first *NuSTAR* observation (on October 19, from 14:43 to 17:45 UTC). We used data from the IBIS/ISGRI detector that operates in the nominal energy range 15–1000 keV providing photon-by-photon data with excellent time resolution of 73 μs. *INTEGRAL* data were only examined for the presence of short bursts.
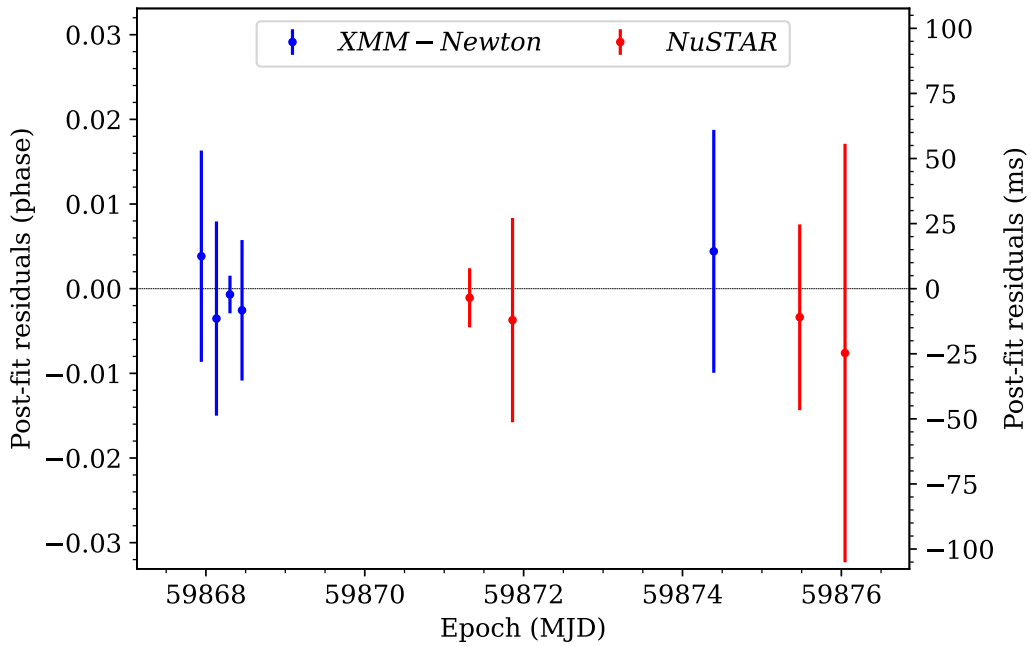
FIGURE 3.2: Post-fit residuals of our best-fit coherent timing solution for SGR J1935+2154 (Table 3.1).

3.3 X-ray Analysis and results

3.3.1 X-ray timing analysis

To perform the timing analysis of SGR J1935+2154, we first filtered out the burst events from the dataset so that they do not affect the integrated pulse profile morphology. We then used the `photonphase` task of the `PINT` software (Luo et al., 2021b) to assign a rotational phase to the barycentered events by extrapolating the ephemeris from Borghese et al. (2022). In order to use the same fiducial reference phase for the *XMM–Newton* and *NuSTAR* dataset, thus enabling phase coherence across the observations, only photons with energies below 15 keV were analysed. We then combined those events into a stable template profile which we modeled with multiple Gaussian components. Using the `photon_toa.py` tool of the `NICERsoft` package[2], we extracted barycentric pulse time of arrivals (TOAs) and proceeded to phase-connect the four dataset with the `TEMPO` timing software (Nice et al., 2015b). We achieved coherence across the dataset using a simple model that only has the spin frequency ν and its first derivative $\dot{\nu}$ as free parameter. We show the post-fit residuals in Figure 3.2 and provide our coherent solution in Table 3.1.

Using our timing model, we then computed the rotational phase associated with the (barycentric) *XMM–Newton* and *NuSTAR* burst epochs (see Table B.1 in Appendix B). Figure 3.3 shows the burst phases against the integrated pulse profiles observed with both instruments. We find no evidence for a preferred burst rotational phase: the burst cumulative distribution in phase across a full rotation cycle is statistically consistent with a uniform distribution (we determined a p-value > 25% using both an Anderson-Darling and Kolmogorov–Smirnov test). Similarly, Younes

---

[2]NICERsoft:
https://github.com/paulray/NICERsoft/wiki

et al. (2020) found no obvious clustering at any particular phase for the $\sim$220 bursts emitted from SGR J1935+2154 during the 2020 reactivation.

TABLE 3.1: Coherent timing solution of SGR J1935+2154 derived from the *XMM–Newton* and *NuSTAR* data. Values in parentheses are the 1-σ uncertainty in the last digit of the fitting parameters reported by TEMPO. The epoch of frequency refers to the reference time for the spin measurements at the Solar system barycenter, while the reference epoch is the phase-zero reference for TOA phase predictions.

Parameter	Measured Value
R.A. (J2000)	19:34:55.598
Decl. (J2000)	21:53:47.79
ν (s^{-1})	0.307525543(4)
$\dot{\nu}$ (10^{-12} s^{-2})	-5.22(5)
P (s)	3.25176241(5)
$\dot{P}$ (10^{-11})	5.52(5)
Epoch of frequency (MJD)	59871.00
Validity range (MJD)	59867.9 – 59876.0
Reference epoch (MJD)	59871.320339421679
Timescale	TDB
Solar system ephemeris	DE200
RMS residuals (ms)	10.8
Daily-averaged RMS residuals (ms)	8.1
	Derived Value
Surface dipolar magnetic field, B_{eq} (10^{14} G)	4.3
Spin down luminosity, $\dot{E}$ (10^{34} erg s^{-1})	6.3
Characteristic age, τ_c (yr)	930

Figure 3.4 shows the background-subtracted light curves folded using the timing solution presented in Table 3.1 as a function of energy for the two epochs. We modelled all the pulse profiles with a combination of a constant plus two sinusoidal functions, with periods fixed to those of the fundamental and first harmonic components. The pulse profile exhibits a simple morphology below 3 keV that evolves to a double-peaked shape at higher energies. At both epochs, the second peak (at phase $\sim$0.7) becomes more prominent above 10 keV and dominates in the 25–79 keV energy interval. The separation between the two peaks increases with energy for both epochs from $\sim$0.3–0.35 in phase at soft X-rays (<10 keV) to $\sim$0.65–0.7 in phase at hard X-rays (>10 keV). Moreover, we detected a phase shift $\Delta\phi$ between the soft (0.3–10 keV) and hard (10–25 keV) energy bands. For the first peak, $\Delta\phi_{0.3-10/10-25}$ is 0.13 ± 0.02 cycles during the first epoch, with the hard photons anticipating the soft ones, and it is not significant for the second epoch. While, for the second peak, we determined a shift of $\Delta\phi_{0.3-10/10-25} = 0.19 \pm 0.01$ and 0.22 ± 0.01 cycles for the first and second epoch, respectively, with the soft photons leading the hard ones. Finally, we studied the dependence of the with the photon energy and its time evolution. The PF (PF) was computed by dividing the value of the semi-amplitude of the fundamental sinusoidal component describing the pulse profile by the average count rate. We did not detect any specific trend in the PF, apart from (i) an increase between the 10–25 keV and 25–79 keV bands for both epoch, and (ii) an increase of the 25–79 keV PF between the two epochs.
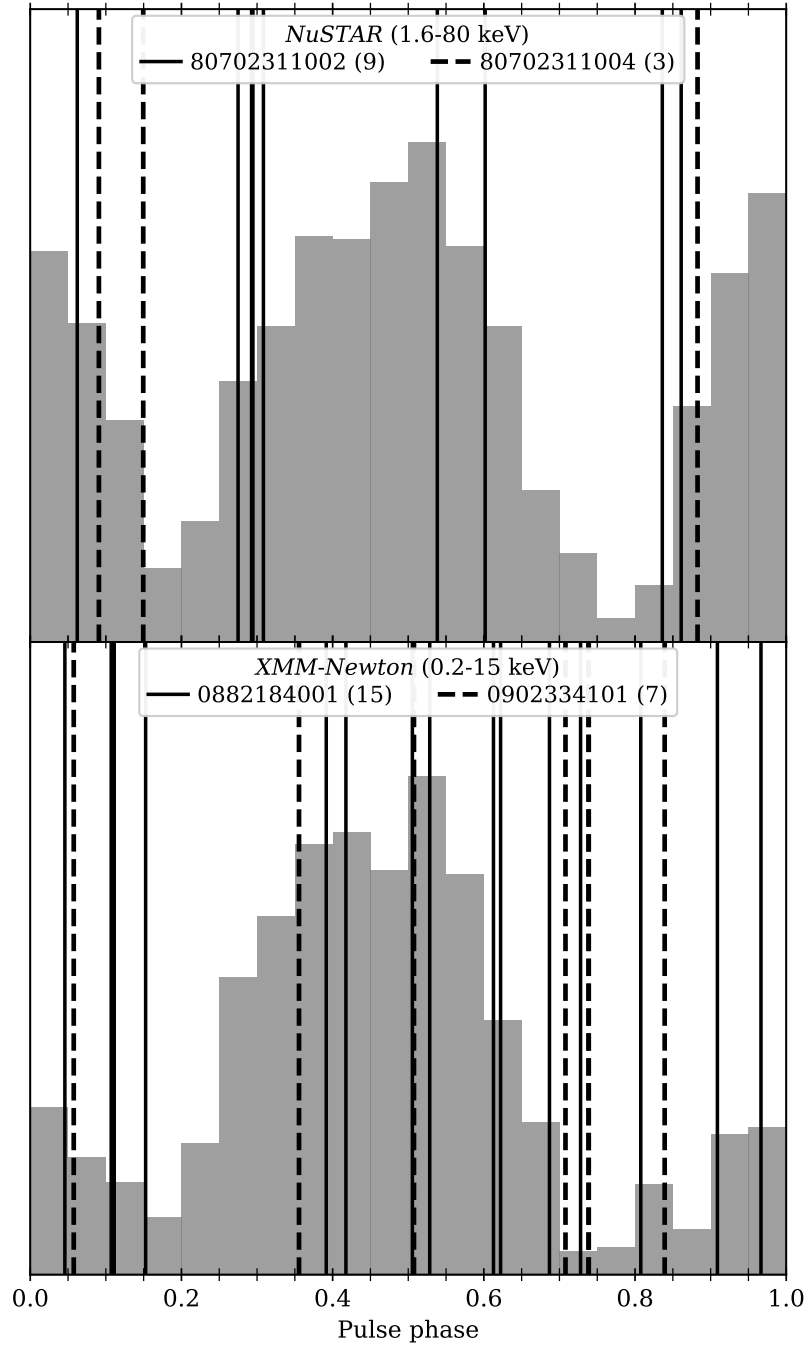
FIGURE 3.3: Phase distribution of the bursts (vertical black lines) detected in the *NuSTAR* (top) and *XMM–Newton* (bottom) dataset (Table B.1), plotted against the combined pulse profiles in each datasets (light grey) over one rotation cycle. The number of bursts in each observation is specified in parentheses next to the observation ID in the legends. The timing model of Table 3.1 was used for the absolute phase alignment. To show the burst phases more clearly, the burst widths (which have duty cycles ranging from ∼1 to 16%) are not depicted in this figure.
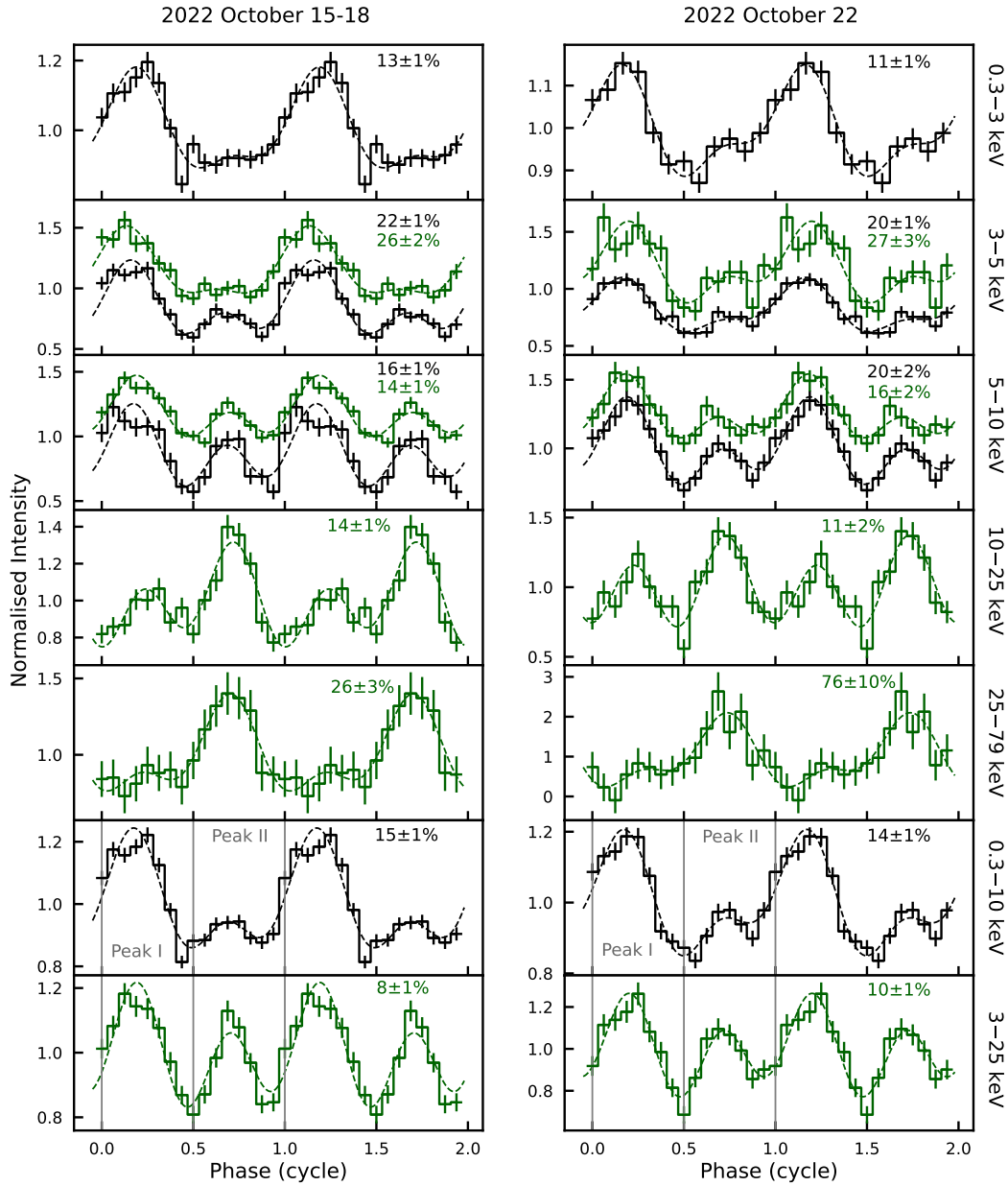
FIGURE 3.4: Background-subtracted, energy-resolved *XMM–Newton*/EPIC-pn (black) and *NuSTAR*/FPMA+FPMB (green) pulse profiles for the 2022 October 15–18 (left-hand panel) and October 22 (right-hand panel) datasets. The dashed line in each panel indicates the best fit for the profiles (for more details, see Section. 3.3.1). The vertical grey lines in the last two panels denote the phase intervals adopted for the phase-resolved spectroscopy (for more details, see Section.3.3.3). The corresponding pulsed fraction values are reported in each panel. Two cycles are shown for clarity and some pulse profiles have been arbitrarily shifted along the y-axis.

3.3.2 X-ray spectral analysis of the persistent emission and search for diffuse emission

The light curves of our observations exhibited several bursts, which will be properly investigated in Section. 3.3.4. In order to exclude the bursts, we filtered out all the events with a count-rate higher than the average count-rate during the persistent state. We then used these filtered events to extract the spectra corresponding to the persistent emission only.

The spectral analysis was performed with XSPEC (v12.12.0; Arnaud, 1996). We used SPECGROUP and GRPPHA tools to group the spectra with a minimum of 50 counts per energy bin for *XMM–Newton*/EPIC-pn and *NuSTAR*/FPMA datasets so as to use the χ^2 statistics. In the following fits, we only used *NuSTAR*/FPMA spectra, but checked that *NuSTAR*/FPMB gave consistent results. The *XMM–Newton* spectra were fit in the 0.5–10 keV energy interval, while for the *NuSTAR* ones the analysis was limited to the 3–25 keV energy band owing to the low signal-to-noise ratio above 25 keV. We adopted the TBABS model with chemical abundances from Wilms, Allen, and McCray (2000) and photoionization cross-sections from Verner et al. (1996) to describe the interstellar absorption.

We simultaneously fit the *XMM–Newton* and *NuSTAR* spectra with an absorbed blackbody plus power-law model (BB+PL), including a constant to account for cross-calibration between the two instruments (see Figure 3.5). N_{H} was tied up across all the four spectra, resulting in $N_{\mathrm{H}}=(2.57 \pm 0.05) \times 10^{22}\,\mathrm{cm}^{-2}$ (reduced chi-square χ^2_ν=1.08 for 567 degrees of freedom (dof)). This value is compatible with those derived in previous studies of SGR J1935+2154 (see e.g., Younes et al., 2017). For each epoch (2022 Oct 15–18 and 22), we linked all the BB+PL parameters across the *XMM–Newton* and *NuSTAR* spectra. However, we allow these parameters to vary between the two epochs. Our analysis showed that there were no significant variations for the blackbody parameters between the first and second epoch, with an emitting radius of $R_{\mathrm{BB}} \sim 1.9$ km and temperature of $kT_{\mathrm{BB}} \sim 0.4$ keV. On the other hand, the photon index slightly changed from $\Gamma = 1.51 \pm 0.02$ to 1.41 ± 0.02 and the PL normalisation decreased by a factor of ~ 1.5. The 0.5–25 keV observed fluxes were $(1.26 \pm 0.02) \times 10^{-11}$ and $(1.04 \pm 0.02) \times 10^{-11}\,\mathrm{erg\,s}^{-1}\mathrm{cm}^{-2}$, giving luminosities of $(9.17 \pm 0.07) \times 10^{34}$ and $(7.48 \pm 0.07) \times 10^{34}\,\mathrm{erg\,s}^{-1}$. The PL component accounted for $\sim 93\%$ and $\sim 89\%$ of the total luminosity at the first and second epochs, respectively.

We also inspected the data taken from the EPIC-MOS1 detector for diffuse emission. For both epochs, we extracted radial profiles of the X-ray emission up to a distance of $100'' - 150''$ from the magnetar, both from the images covering the entire observation duration, and from the images covering variable time intervals following the detection of the brightest X-ray bursts (see Section. 3.3.4 for more details). This second type of analysis was aimed at detecting short episodes of diffuse emission possibly associated with scattering haloes produced by the bursts. In no case did we find evidence of emission in excess of that from the magnetar.

3.3.3 Phase-resolved spectroscopy

We performed a phase-resolved spectroscopy of the *XMM–Newton* and *NuSTAR* datasets of the magnetar persistent emission. Our aim is to investigate any changes with rotational phase (and time) of the parameters of the spectra corresponding to
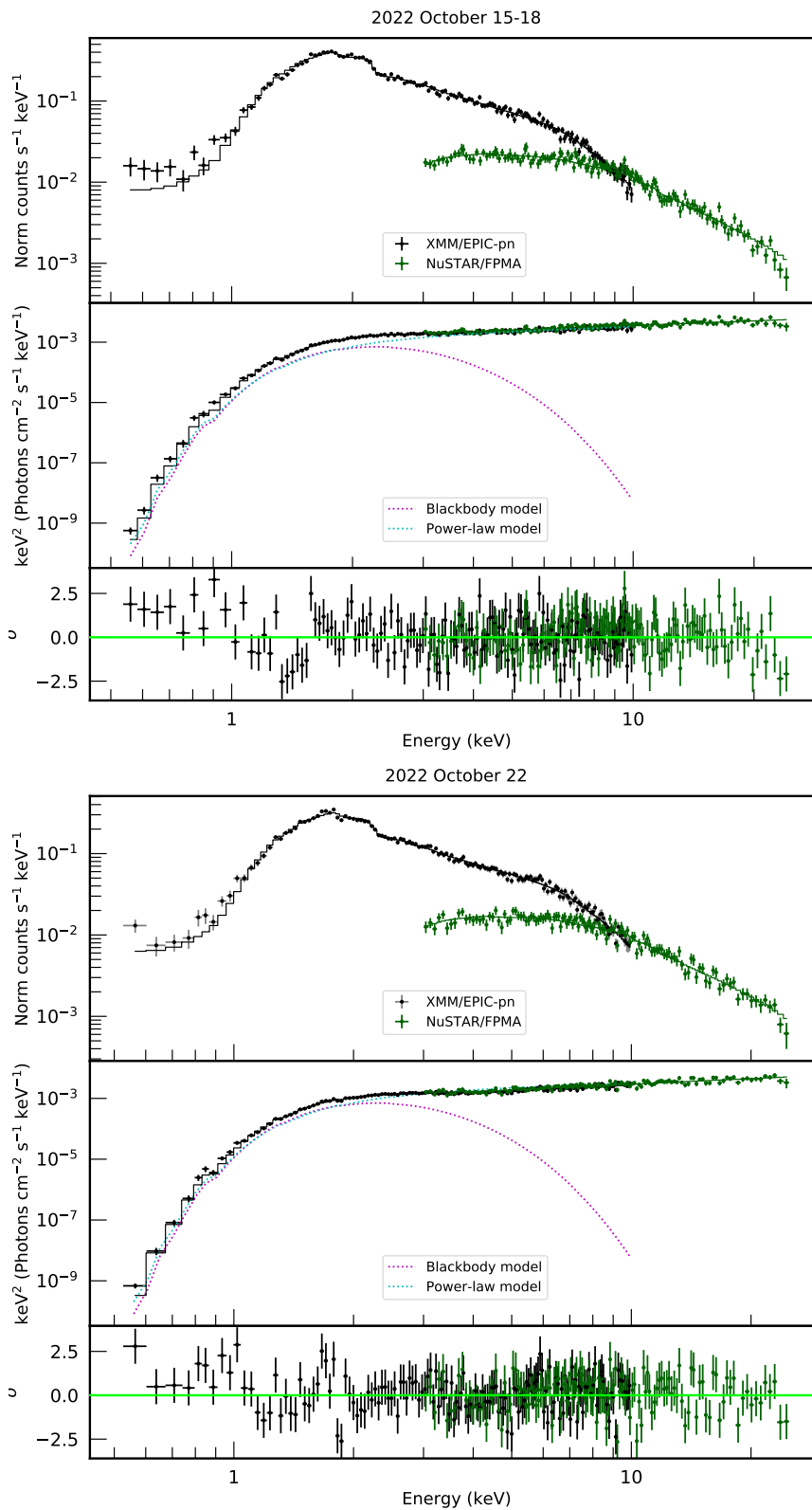
FIGURE 3.5: Spectra of the persistent emission of SGR J1935+2154. The 0.5–10 keV *XMM–Newton*/EPIC-pn (black) and the 3–25 keV *NuSTAR*/FPMA (green) spectra are jointly fit with an absorbed blackbody plus power-law model. For each plot: the *top panel* shows the counts spectra and the best-fitting model; the *middle panel* shows the $E^2 f(E)$ unfolded spectra and the contribution of the single components (dotted lines); the *bottom panel* shows the post-fit residuals in units of standard deviations.

TABLE 3.2: Results of the phase-resolved spectral analysis presented in Section 3.3.3.

	Phase	kT_{BB} (keV)	R_{BB} (km)	Γ	Flux[a] Unabs BB $(10^{-12}\,\mathrm{erg\,s^{-1}cm^{-2}})$	Flux[a] Unabs PL
				2022 Oct 15–18		
Peak I	0.0–0.5	0.42±0.02	1.3±0.1	1.58±0.04	1.38±0.02	7.36±0.01
Peak II	0.5–1.0	0.44±0.01	1.26±0.08	1.36±0.04	1.61±0.02	7.19±0.01
				2022 Oct 22		
	Phase	kT_{BB} (keV)	R_{BB} (km)	Γ	Flux[a] Unabs BB $(10^{-12}\,\mathrm{erg\,s^{-1}cm^{-2}})$	Flux[a] Unabs PL
Peak I	0.0–0.5	0.41±0.01	1.86±0.09	1.30±0.04	2.52±0.01	12.79±0.01
Peak II	0.5–1.0	0.41±0.01	1.83±0.09	1.43±0.04	2.38±0.01	10.05±0.01

[a] The fluxes are estimated in the 0.5–25 keV energy range.

the two pulse profile peaks. Therefore, we extracted the 0.5–10 keV EPIC-pn and 3–25 keV FPMA spectra from the 0.0–0.5 (peak I) and 0.5–1.0 (peak II) phase intervals (see Figure 3.4).

The phase-resolved spectra were fit simultaneously with the BB+PL model. The column density was held fixed at the phase-averaged value (N_{H}=2.57×10^{22} cm^{-2}; see Section. 3.3.2). The spectral fitting results, reported in Table 3.2, revealed variations along the spin phase, which can be primarily attributed to fluctuations in the PL photon index. During the first epoch, the variability was more pronounced with the index decreasing from 1.58±0.04 for peak I to 1.36±0.04 for peak II. In contrast, the second epoch displayed less variability with the index slightly changing from 1.30 ± 0.04 (peak I) to 1.43 ± 0.04 (peak II). At a given epoch, the BB parameters are consistent with each other in the different phase ranges.

3.3.4   X-ray burst search and properties

We investigated the *XMM–Newton* and *NuSTAR* light curves of all observations for the presence of short bursts, applying the method described by Borghese et al. (2020) (see also, e.g., Gavriil, Kaspi, and Woods 2004). We extracted time series with three different time resolutions (1/16, 1/32 and 1/64 s) in order to identify events of different durations. We classified a time bin as a burst if it had a probability $<10^{-4}(NN_{\mathrm{trials}})^{-1}$ of being a Poissonian fluctuation of the average count rate, where N is the total number of time bins in a given light curve and N_{trials} is the number of timing resolutions used in the search. We detected a total of 22 and 12 bursts in the *XMM–Newton*/EPIC-pn and merged *NuSTAR*/FPMA+FPMB light curves, respectively. The burst epochs referred to the Solar system barycenter, as well as the burst fluences and durations, are reported in Table B.1 and Figure 3.6 shows the light curves for the two strongest bursts detected in *XMM–Newton* and *NuSTAR* data.

We extracted the spectra for those events with at least 25 net counts for *XMM–Newton* and for the event with the highest counting statistics for *NuSTAR* (i.e., the burst labelled 80702311002 #9 in Table B.1 with 80 net counts). The background level was estimated from time intervals of the same duration in the persistent state. We employed a minimum number of counts to group the spectra that varies from burst to burst depending on the fluence of the burst itself. We applied the chi-square statistic for model fitting, except for the cases where the counting statistic was too low. In such cases, we adopted the *W*-statistic instead. The spectra were fitted with

an absorbed blackbody model, fixing N_H to the value obtained from the analysis of the phase-average broadband spectrum. The fit results are reported in Table B.1.

Furthermore, for each observation, we extracted a stacked spectrum of all bursts and assigned the spectrum of the persistent-only emission as the background spectrum. We then fit the stacked spectra using the same model we adopted for the spectra of the single bursts (i.e., an absorbed blackbody with N_H fixed at $2.57 \times 10^{22}\,\mathrm{cm}^{-2}$). The *XMM–Newton* spectra were well described by a single blackbody with temperature of $kT_{BB} = 1.14 \pm 0.06\,\mathrm{keV}$ and $kT_{BB} = 1.88 \pm 0.08\,\mathrm{keV}$ for the first and second epochs, respectively. Using the assumed distance of SGR J1935+2154, i.e 6.6 kpc, we obtained radii of $R_{BB} = 0.9 \pm 0.1\,\mathrm{km}$ for the first epoch and $R_{BB} = 1.14 \pm 0.07\,\mathrm{km}$ for the second one. However, this model was unsatisfactory for the *NuSTAR* spectra, and thus a second blackbody component was added. This resulted in temperatures of $kT_{BB,cold} = 0.5 \pm 0.2\,\mathrm{keV}$ and $kT_{BB,hot} = 3.1 \pm 0.3\,\mathrm{keV}$ for the cold and hot components, respectively, with radii of $R_{BB,cold} = 8^{+39}_{-3}\,\mathrm{km}$ and $R_{BB,hot} = 0.27^{+0.06}_{-0.04}\,\mathrm{km}$ for the first epoch. For the second epoch, the temperatures were $kT_{BB,cold} = 0.8 \pm 0.3\,\mathrm{keV}$ and $kT_{BB,hot} = 4^{+4}_{-1}\,\mathrm{keV}$ with radii of $R_{BB,cold} = 1.7^{+6.6}_{-0.5}\,\mathrm{km}$ and $R_{BB,hot} = 0.09 \pm 0.03\,\mathrm{km}$.

For the *INTEGRAL* data, the burst search was carried out in the 30–150 and 30–80 keV energy ranges, by examining light curves binned on seven timescales between 10 and 640 ms. Only the pixels that had more than 50% of their surface illuminated by the source were considered in our analysis. Potential bursts were identified as significant excesses above the expected background level derived from a running average. Once identified, these excesses were then examined through an imaging analysis to confirm their authenticity and positional association with the magnetar. This search resulted in the detection of only two bursts.

Among the three bursts seen with *XMM–Newton* during the *INTEGRAL* observations (i.e., the bursts labelled 0902334101 #1, #2 and #3 in Table B.1), only the brightest one (#3) was detected by *INTEGRAL* as well. The burst had a fluence of 36.6 counts (30–150 keV) in ISGRI, over a duration of about 90 ms. The light curve is shown in Figure 3.6. We assume a spectrum described by thermal bremsstrahlung with a temperature of 30 keV, which is commonly used to describe spectrum of magnetar bursts (e.g. Borghese et al., 2019). The resulting average count rate of 406.6 counts s^{-1} corresponds to a flux of $2.04 \times 10^{-8}\,\mathrm{erg\,s^{-1}cm^{-2}}$. The two bursts detected by *NuSTAR* (8070231100 #7 and #8) were not visible in the *INTEGRAL* data. The second burst detected with ISGRI occurred on 2022 October 19 at 15:25:54.037 (UTC), during a time gap in the *NuSTAR* data. Its fluence and duration were 49 counts (30–150 keV) over 200 ms. The rate of 245.0 counts s^{-1} corresponds to a flux of $1.23 \times 10^{-8}\,\mathrm{erg\,s^{-1}cm^{-2}}$.

3.4 Quasi-simultaneous radio observations

We observed SGR J1935+2154 using three radio telescopes in Europe: the 25-m RT-1 telescope in Westerbork, the Netherlands (Wb), the 25-m telescope in Onsala, Sweden (O8) and the 32-m telescope in *Toruń*, Poland (Tr). Observations were carried out at 1.4 GHz, 1.6 GHz (L-band) and 330 MHz (P-band) (see Table **??** for the observational setup). The source was monitored between October 15 and 19, 2022 for a total of 92.5 hr. This number reduces to 60.4 hr when taking into account the overlap between observations at different telescopes.
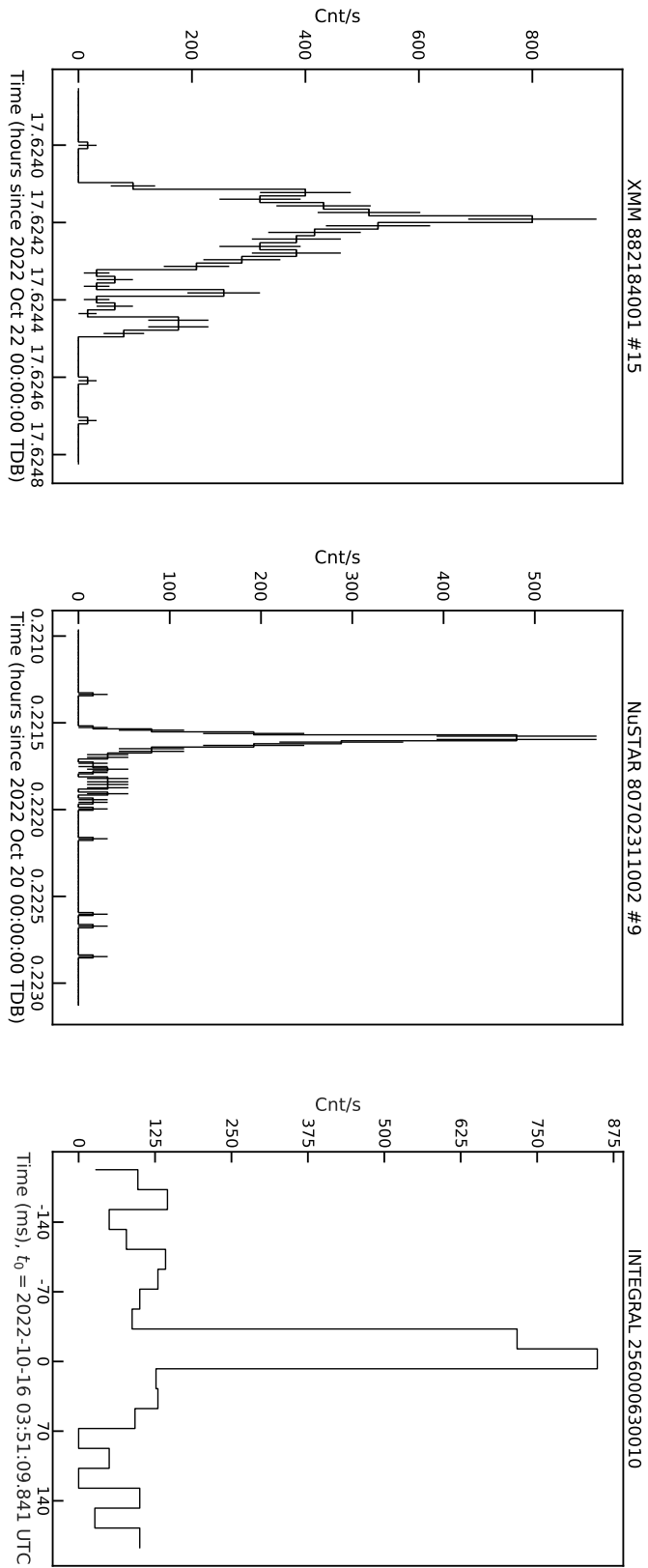
FIGURE 3.6: Light curves extracted from *XMM–Newton*/EPIC-pn (left-hand panel) and *NuSTAR*/FPMA+FPMB (middle panel) data for the strongest bursts, binned at 62.5 ms, while *INTEGRAL*/IBIS/ISGRI (right-hand panel) data is binned at 20 ms.

Station[a]	Band	Frequency Range [MHz]	Bandwidth[b] [MHz]	Bandwidth per subband [MHz]	SEFD[c] [Jy]	Completeness[d] [Jy ms]	Time observed [hrs]
Wb	P	300–364	50	8	2100	46	11.4
Wb	L	1207–1335	100	16	420	7	45.5
Tr	L	1350–1478	100	16	250	4	22.0
O8	L_{O8-1}	1360–1488	100	16	310	5	6.3
O8	L_{O8-2}	1594.49–1722.49	100	16	310	5	7.4
Total telescope time/total time on source [hrs][e]							92.5/60.4

[a] Wb: Westerbork RT1 25-m, O8: Onsala 25-m, Tr: Toruń 32-m
[b] Effective bandwidth accounting for RFI and band edges.
[c] From the EVN status page.
[d] Using Equation 3.1, assuming a 7σ detection threshold and a pulse width of 1 ms.
[e] Total time on source accounts for overlap between the participating stations.

3.4.1 Single pulse search

We searched the data for FRB-like emission applying the custom pipeline described by Kirsten et al. (2021) and Kirsten et al. (2022).

Data is recorded as "raw voltages", also known as baseband data, at each station in *.vdif* format (Whitney et al., 2010). This format encapsulates dual circular polarization with 2-bit sampling. In order to search the data, we first create Stokes I (full intensity) `filterbank` files with 8-bit encoding using `digifil` which is part of `DSPSR` (van Straten and Bailes, 2011). For observations at L-band, the frequency resolution is 125 KHz, and the time resolution of the `filterbank` is 64 μs, with the exception of Tr, which has a time resolution of 8 μs. For the P-band observation, these values are 512 μs and 7.8125 KHz, respectively. We mitigated radio frequency interference (RFI) by applying a static mask. This mask is manually determined for each station and observational setup by identifying channels affected by RFI. We then searched the data for burst candidates using Heimdall[3], setting a signal-to-noise threshold of 7. We only searched for bursts within a dispersion measure (DM) range of $\pm$ 50 units, with the known DM of SGR J1935+2154 being 332.7206 $\pm$ 0.0009 pc cm^{-3} (CHIME/FRB Collaboration et al., 2020). Burst candidates are subsequently classified using the machine learning classifier FETCH (Agarwal et al., 2020). We use models A & H and set a probability threshold of 50%. The produced burst candidates were then all manually inspected to determine if they are astrophysical or RFI.

3.4.2 Search for pulsed emission

In an effort to detect pulsed radio emission from SGR J1935+2154, we folded our radio data using the ephemeris derived from the X-ray data (see Section. 3.3.1). Additionally, we also folded individual scans which were coincident with an X-ray burst. Overall, we had six instances of overlap between X-ray burst detections and radio coverage. Four of these instances were covered by multiple radio telescopes simultaneously (see Table 3.3 for details).

The radio observations are divided into scans each lasting typically 900 s. We first identified the scan that encompassed an X-ray burst, as well as the scans immediately before and after it, totalling roughly 2700 s of data. We used `DSPSR` to fold the data based on the ephemeris. Folding was only possible due to the contemporaneous X-ray and radio observations. These folded scans were subsequently combined into a single file using `psradd`. We then created a diagnostic plot using `psrplot` to determine the presence of pulsed emission. We validated this method by applying it to observations of the pulsar J1935+1616.

---

[3]Heimdall:
https://sourceforge.net/projects/heimdall-astro/

3.4.3 Results

No FRB-like bursts were found in the radio observations. This allows us to calculate a completeness threshold. The completeness threshold is the upper limit on the fluence of a burst that falls below the sensitivity of our instruments and can be derived using the radiometer equation,

$$\mathcal{F} = (\text{S/N}) \cdot \frac{T_\text{sys}}{G} \cdot \sqrt{\frac{W}{n_\text{pol}\Delta\nu}} \ [\text{Jy ms}]\,, \tag{3.1}$$

where (S/N) is the signal-to-noise detection threshold value, $\frac{T_\text{sys}}{G}$ is the System-Equivalent Flux Density (SEFD), W is the width of the burst, n_pol is the number of recorded polarizations and $\Delta\nu$ is the recorded bandwidth. Using Equation 3.1 and the properties of the radio telescopes listed in Table **??**, and assuming a width of 1 ms and a 7σ detection threshold, we can find completeness thresholds of 5 Jy ms for Onsala, 4 Jy ms for *Toruń*, 7 Jy ms and 46 Jy ms for Westerbork L- and P-band, respectively. Moreover, we folded radio data at the times of overlap between X-ray detections of bursts and we folded all recorded L-band data spread over four days from Westerbork and *Toruń*, which corresponds to 45.5 hr and 21.9 hr of observations, respectfully. We found no evidence for pulsed radio emission from SGR J1935+2154 using both approaches. We can therefore determine an upper limit on the typical minimum flux density using the following equation:

$$S_\text{mean} = (\text{S/N}) \cdot \frac{\beta T_\text{sys}}{G\sqrt{n_\text{pol}t_\text{obs}\Delta\nu}} \cdot \sqrt{\frac{W}{P-W}} \ [\text{Jy}]\,, \tag{3.2}$$

where β is a factor accounting for quantization effects and is approximated to be 1.1 (see Lorimer and Kramer, 2004, and references therein); P is the spin period of the source as quoted in Table 3.1; and W is the width of the folded profile which is assumed to be equal to 10% of the period. A complete overview of all derived upper limits can be found in Table 3.3. For the Westerbork P-band observation we find a mean flux density limit of 14.86 mJy, while for the L-band observations we find flux density limits between $0.23 - 2.1$ mJy for the different telescopes, configurations and integration times.

3.5 Discussion

On 2022 October 10-11, the magnetar SGR J1935+2154 entered a new outburst, characterized by the emission of several short X-ray bursts and an increase of the persistent X-ray flux. Moreover, like the previous outburst in 2020, the source emitted a few radio bursts with X-ray counterparts (e.g., Younes et al., 2022a). This event is the sixth detected outburst from SGR J1935+2154, making this magnetar one of the most active known so far.

Here, we presented the properties of the X-ray persistent emission and bursts of SGR J1935+2154 during the first weeks of its most recent outburst based on observations obtained with *XMM–Newton* and *NuSTAR*. Additionally, we performed searches for single pulses and pulsed emission through quasi-simultaneous radio observations without any successful results.

Flux and spectral decomposition:
The outburst onset was marked by the emission of several short X-ray bursts between 10 and 11 October 2022 (see e.g., Palmer, 2022; Mereghetti et al., 2022). Our observations were carried out $\sim$6 and 12 days later. At both epochs, emission was detected up to 25 keV (see Figure. 3.5). Hard X-ray emission from SGR J1935+2154 was also seen in a pointing performed $\sim$5 days after the 2015 outburst onset and was still observed 5 months after the 2020 reactivation (Younes et al., 2017; Borghese et al., 2022). The persistent X-ray spectra were well modeled by the combination of a thermal and non-thermal components. The thermal component was well described by a blackbody model. Its parameters remained stable over time, with a temperature of $\sim$0.4 keV and radius of $\sim$1.9 km. The non-thermal component had a power-law shape and its contribution to the total 0.5–25 keV luminosity decreased only marginally from $\sim$93% to $\sim$89% in about 5 days.

The quiescent level of SGR J1935+2154 is not known yet. Here, we adopt the quiescent observed flux derived by Borghese et al. (2022) using a *XMM–Newton* observation performed on 2014 October 4, i.e. $(8.7 \pm 0.3) \times 10^{-13}\,\mathrm{erg\,s^{-1}cm^{-2}}$ (0.3–10 keV). The ratio between the 0.3–10 keV observed flux measured during our first observation, $(6.45 \pm 0.05) \times 10^{-12}\,\mathrm{erg\,s^{-1}cm^{-2}}$, and that in quiescence is $R_{2022} \sim 7.4$. Assuming the same quiescent flux and considering the peak fluxes of the previous outbursts measured by Younes et al. (2017) and Borghese et al. (2020), we calculated the same ratio. Upon comparison, we found that R_{2022} was greater than the values from the 2014 and 2015 events, which were $R_{2014} \sim 4.9$ and $R_{2015} \sim 5.4$, respectively. However, it was lower than the ratios from the May and June 2016 outbursts, which were $R_{2016\mathrm{May}} \sim 9.7$ and $R_{2016\mathrm{June}} \sim 16$, respectively. Notably, the 2020 reactivation was the most powerful, with a ratio of $R_{2020} \sim 49$.

Spin-down rate and pulse profile:
We detected the spin period and the spin-down rate using *XMM–Newton* and *NuSTAR* datasets, covering the period of 15–22 October 2022. We were able to establish a phase-coherent timing solution (see Table 3.1). The spin-down rate we inferred was markedly different from those derived during previous outbursts. Specifically, our results indicated that the spin-down rate during the first weeks on the 2022 reactivation ($\dot{P} \simeq 5.52(5) \times 10^{-11}\,\mathrm{s\,s^{-1}}$) was a factor of 3.8 times larger than the value measured during the first four months of the 2014 outburst ($\dot{P} \simeq 1.43 \times 10^{-11}\,\mathrm{s\,s^{-1}}$; Israel et al. 2016b), and 1.5 times larger than the spin-down rate during the 2020 outburst ($\dot{P} \simeq 3.5 \times 10^{-11}\,\mathrm{s\,s^{-1}}$; Borghese et al. 2022, see also Younes et al. 2020, Younes et al. 2023). The observed variations in the spin-down rate suggest a notable change in the factors affecting the spin-down, e.g. the magnetospheric geometry and/or the relativistic wind of SGR J1935+2154 during different outbursts. Moreover, changes in the spin-down rate are common during outbursts, indicating changes in the magnetosphere caused by the rearrangement of magnetic fields. To determine the secular spin-down rate of SGR J1935+2154, a targeted monitoring campaign during the quiescence state is needed. The evolution of the pulse profile during the 2022 reactivation of SGR J1935+2154 displays some differences when compared to previous outbursts. The pulse profiles observed in both *XMM–Newton* and *NuSTAR* observations exhibits a distinctive double-peaked morphology (see Figure. 3.4). Notably, the second peak (at phase $\sim$0.7) becomes more prominent at energies above 10 keV for both epochs. The observed double-peaked structure contrasts with the quasi-sinusoidal shape showed during the 2014 outburst, as reported in *XMM–Newton* and *Chandra* observations (Israel et al., 2016b). However, it closely resembles that extracted from *NuSTAR* and *XMM–Newton* observations taken

during the 2020 outburst (Borghese et al., 2020; Borghese et al., 2022). The change of the pulse profile from a single-peak shape in the 2014 outburst to a double-peak shape during the 2022 reactivation may be related to the fact that different regions on the neutron star surface are heated during each outburst. Similarly to the 2014 outburst, we detected an energy-dependent pulse profile phase shift. Slight phase shifts between the peak emissions in the soft and hard X-ray pulse profiles have been observed in a number of magnetars, e.g., XTE J1810−197 (Borghese et al., 2021) and 1E 1547.0−5408 (see Coti Zelati et al., 2020, and references therein). This phenomenology is consistent with the widely accepted scenario that magnetars non-thermal X-ray emission stems from resonant inverse Compton scattering of photons emitted from the star surface by charged particles moving along magnetic loops anchored to the crust and corotating with the star (Wadiasingh et al., 2018, and references therein). In this scenario, the hard, non-thermal X-ray emission is expected to be beamed along the loop and to be misaligned (in most cases) to some extent with respect to the soft, thermal X-ray emission pattern from the hot spots on the star surface. The PF increased when shifting from the 10–25 keV to 25–79 keV energy bands at each epochs. We also observed a time-dependent change in the PF for the 25–79 keV and 3–25 keV energy intervals with its value increasing between the two epochs. These results are inconsistent with the findings reported by Israel et al. (2016b), where they reported a time independent PF in the 17–21 % range.

Pulse profile modelling:
We determine the emission geometry of SGR J1935+2154 by examining the orientation of the hot spot relative to the line of sight and the star's rotational axis. To achieve this, we compared the observed PF to a set of simulated PFs generated using the method outlined by Perna, Heyl, and Hernquist (2001) and Gotthelf, Perna, and Halpern (2010).

Our approach involved creating a temperature map on the surface of the star. This map included a uniform background temperature and a single hot spot characterized by a Gaussian temperature profile. The hot spot's orientation with respect to the star's rotational axis was defined as an angle χ, while we also specified the line of sight's orientation as an angle ψ relative to the rotational axis. We then computed the observed phase-resolved spectra by integrating the local blackbody emission from the visible part of the stellar surface. In this calculation, we considered the effects of gravitational light bending, approximating the ray-tracing function (Pechenick, Ftaclas, and Cohen, 1983; Page, 1995) using the formula derived by Beloborodov (2002). Additionally, we took into account absorption by the interstellar medium. Since our model includes thermal emission only, we restrict our analysis to the energy range 0.3–2 keV where the blackbody component dominates the emission. In this range, the PF is 10.8 ± 1.4 % in the first epoch, and 7.3 ± 1.1 % in the second one. The pulse profile can be modelled using a simple sinusoidal function with a single peak per rotational phase, so in our modelling we consider a temperature map with a single hot-spot. For the temperature and the radius of the hot-spot, we considered the values obtained from the phase-resolved spectral-fit of peak I reported in Table 3.2. The contribution from the rest of the stellar surface is neglected since it does not contribute significantly to the emission.

We report the results of our analysis in Figure 3.7. The color map on the $\chi - \psi$ plane represents the value of the PF obtained by our modelling using the input parameters from the first epoch. The white and red contours represent the regions matching the observed PF in the first and second epoch, respectively. Continuous
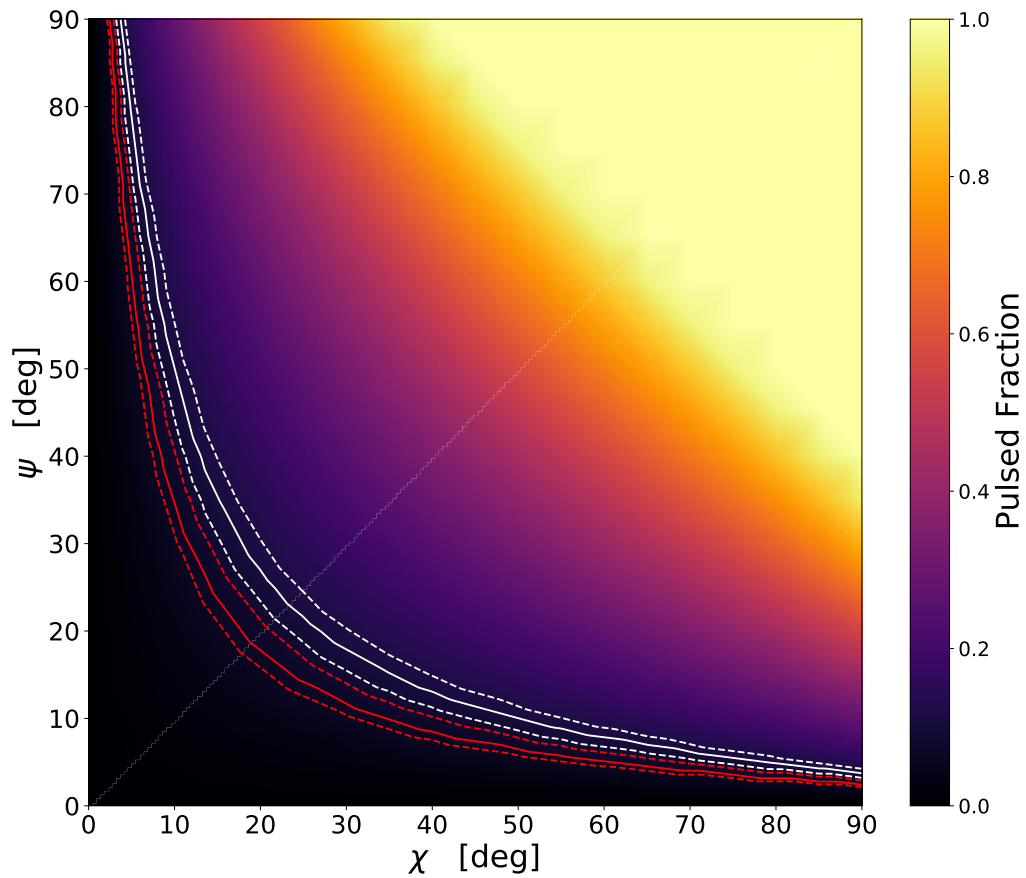
FIGURE 3.7: Constraints on the emission geometry of SGR J1935+2154, based on the PF measured in the first epooch (15th October 2022). The color scale represents the 0.3–2 keV PF at different angles. The white lines represent the measured value (PF = 10.8 ± 1.4%), while the red lines represent the measured value at the second epoch (PF = 7.3 ± 1.1%).

curves represent the central value of the PF, dashed curves represents the 1σ uncertainty regions. While the two regions do not overlap, they are consistent within 2σ. Our analysis suggests two preferable configurations: one where both angles have moderate values (*e.g.* $(\chi - \psi) \sim (25^\circ - 25^\circ)$) and another where the line-of-sight is near the rotational axis and the hot-spot is almost perpendicular to it.

TABLE 3.3: Limits on the mean flux density S_{mean} after folding the radio data for the entire Westerbork and *Toruń* observations using the ephemeris as derived in the X-ray analysis. Additionally, we also fold and place upper limits on the flux density in the case of X-ray burst overlap instances.

Overlap X-ray	Station	Band	Start time[a] [TOPO UTC]	Stop time[a] [TOPO UTC]	#Scans	Exposure time [s]	S_{mean}[b] [mJy]
	Tr	L	2022-10-15 14:30:08	2022-10-19 22:11:59	111	79041	0.23
	Wb	L	2022-10-16 11:30:41	2022-10-19 23:14:38	180	163754	0.27
XMM/0902334101 #1	Wb	P	2022-10-15 20:13:19	2022-10-15 20:58:38	3	2685	14.86
#1	O8	L_{O8-2}	2022-10-15 20:19:37	2022-10-15 21:04:58	3	2685	1.55
#1	Tr	L	2022-10-15 20:12:57	2022-10-15 20:49:49	3	2138	1.40
#2	O8	L_{O8-1}	2022-10-16 00:24:14	2022-10-16 00:54:21	2	1791	1.90
NuSTAR/80702311002 #5	Wb	L	2022-10-19 11:18:42	2022-10-19 12:04:04	3	2690	2.10
#6	Wb	L	2022-10-19 13:00:50	2022-10-19 13:46:10	3	2687	2.10
#7	Wb	L	2022-10-19 17:04:03	2022-10-19 17:49:24	3	2690	2.10
#7	Tr	L	2022-10-19 17:12:37	2022-10-19 17:49:29	3	2137	1.40
#8	Wb	L	2022-10-19 17:34:27	2022-10-19 18:19:48	3	2691	2.10
#8	Tr	L	2022-10-19 17:37:38	2022-10-19 18:14:30	3	2136	1.40

[a] The time elapsed between start and stop times is not continuous due to $\sim$ 10-s gaps between scans.
[b] Using Equation 3.2, properties from Table ?? and assuming a 10σ detection and 10% duty cycle.

4 Searching for an isolated magnetic white dwarf pulsar ZTF J1901+1458

4.1 Introduction

Isolated magnetic white dwarfs (WDs) have been predicted to emit dipolar radiation in the radio band for a long time, since the discovery of radio pulsars. However, to date no such emission has been conclusively recognized. The recent discovery of long-periodic radio transients such as GLEAM-X J162759.5−523504.3 (hereafter GLEAM-X J1627−52, Hurley-Walker et al., 2022) and GPM J1839−10 (Hurley-Walker et al., 2023) has presented new challenges in interpreting their emission within the traditional pulsar framework. Notably, these sources display radio luminosities that exceed their estimated spin-down luminosities, making it difficult to explain their emission through typical pulsar mechanisms. For example, GLEAM-X J1627−52 has a period of $P = 1,091$ s, a radio luminosity of $L_{1.4\,GHz} = 4 \times 10^{31}$ erg s^{-1} with a peak flux density of $S_{154\,MHz} = 45$ Jy, based on measurements taken over several months and spin-down luminosity of $\dot{E} = 6.17 \times 10^{28}$ erg s^{-1}. Similarly, GPM J1839−10 which has been active for over three decades, exhibits a period of $P = 1,318$ s, a radio luminosity of $L_{1.4\,GHz} = 10^{28}$ erg s^{-1}, and a spin-down luminosity of $\dot{E} = 8.4 \times 10^{24}$ erg s^{-1}. Figure. 4.1 shows the radio luminosity vs the spin-down power for isolated radio pulsars, highlighting both GLEAM-X J1627−52 and GPM J1839−10 as they lie above the line where $L_{1.4\,GHz}$ equals $\dot{E}$.

Motivated by these discoveries, we initiated a search for the known isolated magnetic WDs with short spin period in the radio band. The primary target of our investigation is ZTF J190132.9+145808.7 (hereafter ZTF J1901+1458), a massive WD discovered by the Zwicky Transient Facility (ZTF[1]; Masci et al., 2019)). ZTF J1901+1458 has a mass ranging between 1.327 $M_\odot$ and 1.365 $M_\odot$, placing it close to the Chandrasekhar limit. It has a spin period of 416 s, and a magnetic field in the range of $B = 6 \times 10^8 - 9 \times 10^8$ G (Caiazzo et al., 2021). Additionally, the effective temperature and the cooling age of ZTF J1901+1458 were estimated to be $T_{eff} = 46,000^{+19.000}_{-8.000}$ K and 10-100 Myr, respectively.

In this work, we present the analysis performed to search for radio emission from ZTF J1901+1458. Section. 4.2 details the observations and data reduction process. Section 4.3 presents the analysis and results, followed by the conclusion.

---

[1]the Zwicky Transient Facility:
https://www.ztf.caltech.edu/publications.html
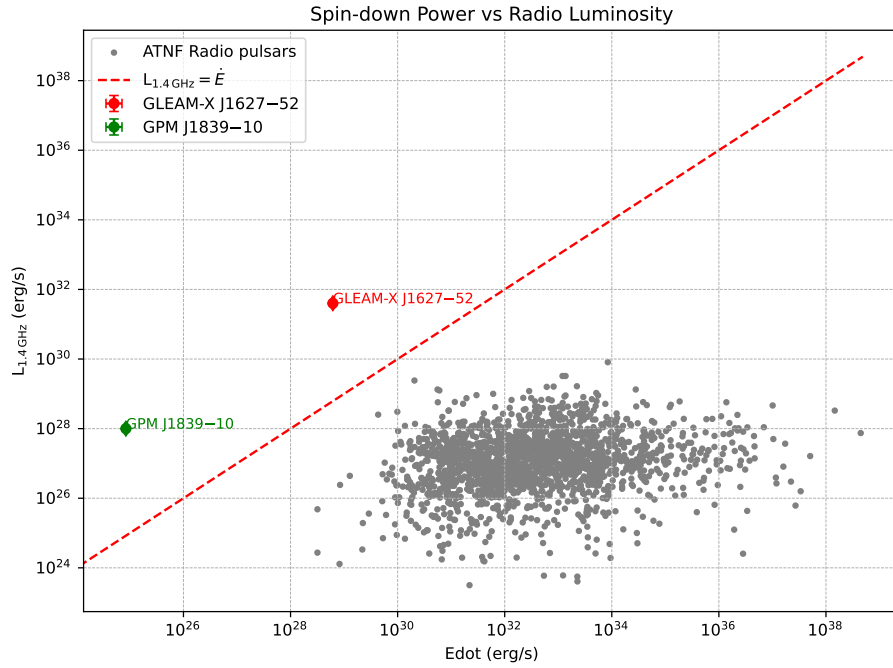
FIGURE 4.1: Radio luminosity at 1.4 GHz ($L_{1.4\,GHz}$) as a function of spin-down power ($\dot{E}$) for isolated radio pulsars from the ATNF catalog. GPM J1839−10 (upper limits) is marked in green, and GLEAM-X J1627−52 (upper limits) is marked in red. The dashed line represents where $L_{1.4\,GHz}$ equals $\dot{E}$

4.2 Radio Observations

4.2.1 *ASKAP*

The Australian Square Kilometre Array Pathfinder (*ASKAP*[2]) is a radio telescope array located in Western Australia. It consists of 36 dish antennas, each 12 meters in diameter, equipped with innovative Phased Array Feeds (PAFs) that enable a wide field of view of $\sim 30\,\mathrm{deg}^2$ and $15\,\mathrm{deg}^2$ at 800 MHz and 1700 MHz frequency bands, respectively (Hotan et al., 2021). *ASKAP* data are processed using *ASKAPsoft*[3] pipeline (Guzman et al., 2019), which calibrates and images the data to produce per-beam calibrated visibilities and full-Stokes images for the entire field of view. We checked the CSIRO ASKAP Science Data Archive (CASDA[4]), using the known coordinates of ZTF J1901+1458, i.e. R.A. = $19^{\mathrm{h}}01^{\mathrm{m}}32\overset{s}{.}9$, Decl. = +14°58′08″7; J2000. Table. 4.1 lists all *ASKAP* observations covering the region of the source within a radius of 3′. These data include observations from the Rapid ASKAP Continuum Survey (RACS; McConnell et al., 2020) and the Variables and Slow Transients Survey (VAST; Murphy et al., 2021). RACS is a multi-band survey designed to cover the whole sky south of declination Decl. = +50°. We obtained observations from both RACS-low (central frequency of 888 MHz) and RACS-mid (central frequency of 1367.5 MHz; see, Duchesne et al., 2023) with an integration time of 15 minutes for

---

[2]ASKAP:
https://www.skatelescope.org
[3]ASKAPsoft:
https://bitbucket.csiro.au/projects/ASKAPSDP/repos/yandasoft
[4]CASDA:
https://research.csiro.au/casda

TABLE 4.1: Observations log of ZTF J1901+1458

Observation ID	Beam	Start Date (UTC)	End Date (UTC)
		(YYYY-MM-DD hh:mm:ss)	
		ASKAP/RACS	
SB56544†	19,25,26	2024-01-02 05:03:20	2024-01-02 05:17:16
SB21693⋆	19,25,26	2021-01-21 02:24:52	2021-01-21 02:39:47
SB8570†	19,20	2019-04-24 19:08:34	2019-04-24 19:23:59
		ASKAP/VAST[a]	
SB62085	07,19,20	2024-05-04 19:10:07	2024-05-04 19:22:14
SB61312	19,20	2024-04-19 21:44:18	2024-04-19 21:56:24
SB60807	20	2024-04-04 22:45:13	2024-04-04 22:57:19
SB60211	20	2024-03-19 21:45:29	2024-03-19 21:58:45
		VLA[b]	
19A-386	N/A	2019-08-22 04:13:32	2019-08-22 06:14:40

†RACS-low (888 MHz) observations

⋆RACS-mid (1367.5 MHz) observations

[a]*ASKAP*/VAST observations performed at centre frequency of 888 MHz

[b]*VLA* observations performed within a frequency range of ~ 1–$2\,$GHz

both bands. VAST survey focuses on detecting and monitoring variable and transient radio sources over timescales from $\sim 5\,$s to 5 years. VAST observations are performed at central frequency of 888 MHz with a band width of 288 MHz, each with 12 minutes integration time.

4.2.2 Very Large Array (*VLA*)

We searched the NRAO archive[5] and found a *VLA* observation at L-band that covers the region of ZTF J1901+1458. The observation was conducted with the Expanded Very Large Array (EVLA) project. It contains a total of 6,750,900 data records, with a total elapsed time of 7268 seconds (see Table 4.1). The observation schedule consisted of multiple scans targeting different fields and calibrators. The primary field of interest "Field 67" was performed on August 22, 2019 from 05:46:52.0 to 05:48:00.0 (UTC), centered at R.A. $= 19^{\text{h}}01^{\text{m}}32\overset{\text{s}}{.}2$, Decl. $= +15°00'21''\!.0$; J2000. The spectral setup included 12 unique spectral windows covering various frequency ranges. Each spectral window was observed with 2048 channels, except for the third, fourth, fifth, seventh, ninth, and tenth windows, which had 64 channels each.

4.3 Analysis and Results

We performed a search for radio emission from ZTF J1901+1458 using data from *ASKAP*, and *VLA* calibrated measurements set (MS). The data were processed and imaged using the Common Astronomy Software Application CASA (v.6.5.4.9; THE CASA TEAM et al., 2022) package. Before proceeding with the imaging and the sub-analysis, we first fixed the beam direction of *ASKAP* visibility data. As processed

---

[5]NRAO Archive:
https://data.nrao.edu/portal/

with ASKAPSOFT, these visibilities are organised per beam. However, the MS for each beam records the center of the 36-beam combined field as the pointing center, instead of the actual pointing center of the individual beam. This misalignment can introduce phase errors if left uncorrected. Thus, we updated the MS for each *ASKAP* observations listed in Table. 4.1 to reflect the accurate pointing center for ZTF J1901+1458.

4.3.1 Imaging Analysis

We performed the imaging process using `tclean` task in CASA, generating both dirty and clean images to carefully examine the data for potential detection. Visual inspection of these images was performed using the CARTA software (Cube Analysis and Rendering Tool for Astronomy, Comrie et al., 2021). Following the inspection of the dirty images, which provided an overview of the field and an estimate of the RMS noise, we proceeded to generate the clean images.

For the clean images, we employed the `hogbom` cleaning algorithm for deconvolution process, maximising the sensitivity with a standard grading and natural weighting scheme. The imaging parameters for *ASKAP* and *VLA* data were adjusted based on the result from the dirty images for each observation. In most cases, we used an image size of 4000 pixels with a scale of 1.0 arcsec per pixel, centering (using "phase-center" parameter of `tclean`) on the pointing direction for ZTF J1901+1458. Despite our efforts, ZTF J1901+1458 was not detected in the final cleaned images, with a sensitivity limit of 0.4 mJy for the *ASKAP* data and 0.8 mJy for the *VLA* data. Figure. 4.2 presents two examples of *ASKAP* images with the position of ZTF J1901+1458 is highlighted by a cyan circle.

4.3.2 Variability Analysis

We also conducted time variability analysis by creating 10-second timestep images from the *ASKAP* data to search for any transient or variable radio emission from ZTF J1901+1458. Each snapshot image covers a 10-second interval, with a total number of images generated corresponding to the full duration of the observation. The images were generated using the `briggs` weighting scheme, with the default robustness parameter and were then exported to FITS format for further inspection using the `ds9` tool.

After carefully examining the 10-second step images, we did not detect any emission from ZTF J1901+1458 during the observation period of *ASKAP* data.

4.4 Preliminary conclusion

In this work, we conducted a detailed search for radio emissions from the isolated magnetic white dwarf ZTF J1901+1458 using observations from *ASKAP* and the *VLA*. Our analysis included both standard imaging techniques and a variability search through dynamic spectral analysis.

After careful processing and imaging of the *ASKAP* and *VLA* data, we did not detect any significant radio emission from ZTF J1901+1458. The final cleaned images provided sensitivity limits down to 0.4 mJy for the *ASKAP* data and 0.8 mJy for the *VLA* data, yet no emission was observed at the location of ZTF J1901+1458. Additionally, a detailed inspection of 10-second timestep images generated from the *ASKAP* data also revealed no variability or transient emission from the source.
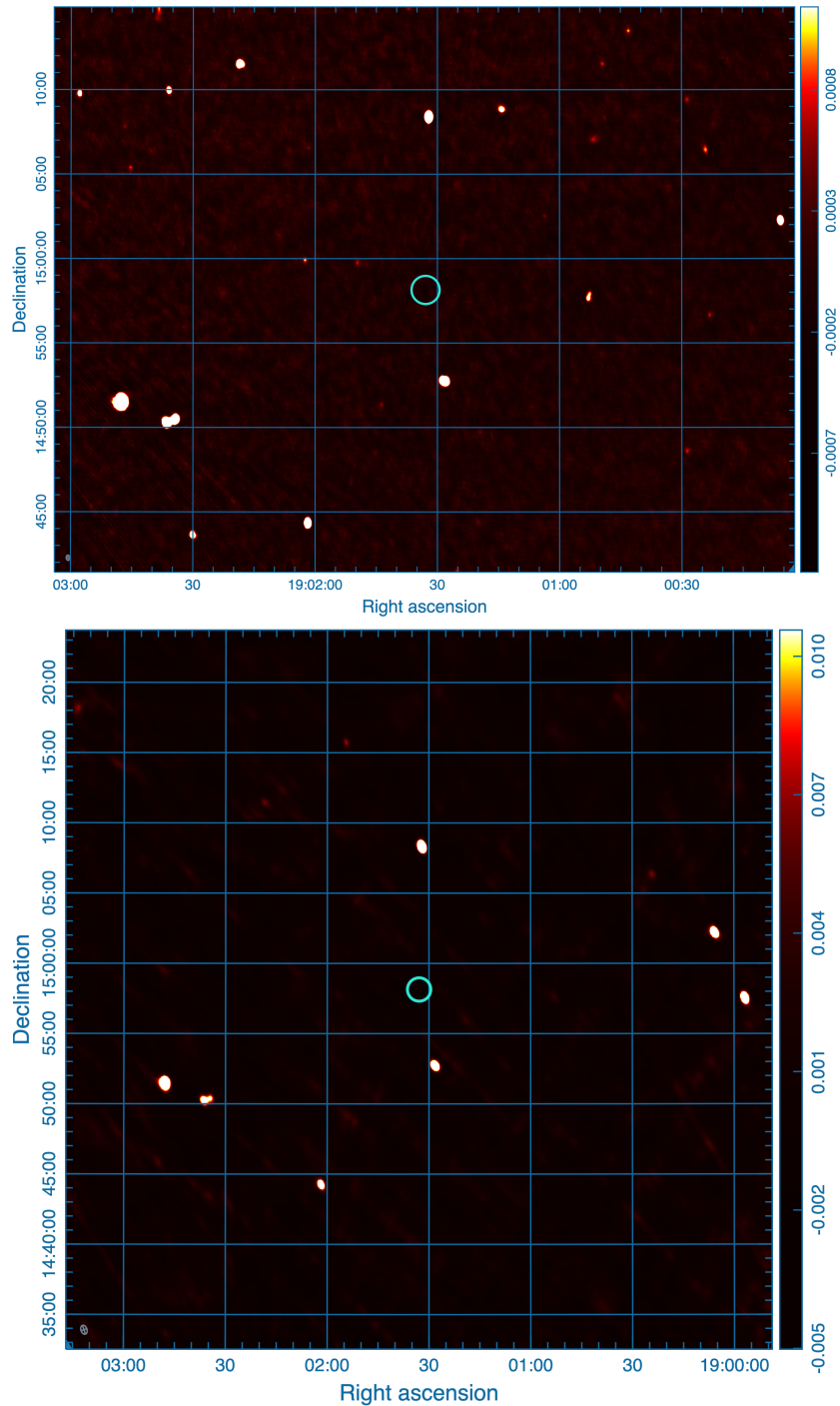
FIGURE 4.2: Processed images from the *ASKAP* telescope. The top panel shows the cleaned image from the RACS-mid survey with a 15-minute integration time at L-band, while the bottom panel presents the cleaned image from the VAST survey data with a 12-minute integration time at 888 MHz. The position of ZTF J1901+1458 is indicated by the cyan circle in both images. The color bar in the right-side of each image shows the color-scale rendering of the image viewer.

Further observations with higher sensitivity and at different radio frequencies may be required to definitively determine the radio emission properties of ZTF J1901+1458.

5 *eBANDERAS*: Pulsar and Transient Search Pipeline

5.1 Overview of the *eBANDERAS* Pipeline Project

The *eBANDERAS* project aims to develop an automated and systematic pipeline to search and characterize X-ray variability in X-ray surveys. This project follows in the footsteps of previous efforts, such as CATS@BAR and Exploring the Transient and Variable Sky X-ray (EXTraS)[1] projects, which systematically searched for X-ray periodic and transient sources using *Chandra* and *XMM–Newton*, respectively (see, e.g. Israel et al., 2016a; De Luca et al., 2021).
eBANDERAS is designed to be as mission-independent as possible, ensuring flexibility and adaptability to current and future missions, such as *eROSITA* (Predehl et al., 2021) and Einstein Probe (EP, Yuan et al., 2022) with minimal modifications.

Figure. 5.1 presents the design of *eBANDERAS* pipeline. The flowchart in the figure illustrates the mission-independent tasks with their dedicated modules, shown in gray and violet boxes. These tasks include:

- **The transient search component**: Currently under development and led under my guidance, this component aims for detecting transients X-ray events (more details in Subsection 5.2).

- **Periodicity search with** `dpspy`: This module is responsible for identifying coherent periodic signals in the power density spectrum (PDS) from a time series, playing a critical role in the detection of pulsars and other periodic sources.

- **Aperiodic search with** `avenue`: The avenue (Aperiodic Variability Exploration iN cUrvEs) module aims at exploring and performing a search for irregular variations in a time series.

- **Spectral analysis with** `pyxie`: The `pyxie` module performs spectral fitting and analysis of detected X-ray sources.

- **Candidate diagnostics and Visual inspection**: These steps involve the final review of detected candidates, ensuring that automated detections are accurate and scientifically relevant.

However, some steps in the pipeline remain mission-specific and depend on software customised for specific X-ray missions. For instance, data reduction requires specific software for each X-ray mission, such as eSASS[2] for *eROSITA*, SAS for *XMM–Newton*, HEASoft for *Swift* and CIAO for *Chandra* (these missions are detailed in Section 1.3). These mission-specific steps are represented by green

---

[1] *EXTraS*:
http://www.extras-fp7.eu/

[2] Updated version for Science Analysis Software System (eSASS):
https://erosita.mpe.mpg.de/dr1/eSASS4DR1/

boxes in the flowchart. The data reduction module is written in Python, however it requires the prior installation of the aforementioned mission-specific external software packages to operate correctly.

5.1.1   *eROSITA* **Application**

As the first practical application of the *eBANDERAS* pipeline, we started the project by focusing on the recent *eROSITA* data[3] reduction (details about the *eROSITA* telescope are provided in Sub-section 1.3.5). The `eroReduction` tool handles the reduction of raw FITS files and extracts the necessary files for subsequent analysis, following guidelines from the eSASS cookbook[4]. `eroReduction` can be used for single sources or in pipeline mode. In single source mode, it requires inputs such as the source regions. In pipeline mode, `eroReduction` implements the source detection chain as described in the online guide, identifies detected sources, defines extraction regions, and extracts both event files and light curves for each source.

Additionally, mission-specific modules such as the `eroBary` tool were developed to barycenter *eROSITA* event files. We adopted the convention of naming each mission-dependent module with the mission's name, such as ero (e.g., `eroReduction` for the *eROSITA* mission). For instance, we named the module `eroBary` because it relies on both HEASoft and eSASS tools.

5.2   **Transients search**

The main focus of my contribution to the *eBANDERAS* pipeline is the development of the transient search module. Building upon the framework established by the EXTraS project (see, e.g., De Luca et al., 2021), this module is designed to detect and analyze transient events within X-ray survey data. The EXTraS was an EU-funded project designed to extract and characterize all temporal domain information from the *XMM–Newton* archive. It achieves this through four lines of analysis including short- and long-term variability and search for coherent pulsations and transients. The analysis was performed within 3XMM catalogues (i.e. ~ 400 thousands X-ray sources detected within the $0.1-12$ keV energy range; see, Rosen et al., 2016). Results can be accessed through a public archive[5].

EXTraS transients pipeline performed a systematic search for X-ray transients within the whole *XMM–Newton* observations included in the $3XMM-DR5$ catalogue (i.e. ~ 8 thousands observarions; Rosen et al., 2016). This resulted in the detection of 136 X-ray transient sources with a duration between 1000 s and 5000 s (see, Table B.1; De Luca et al., 2021).

5.3   **Status and future plans**

At the time of writing this thesis, my efforts are concentrated on retrieving and studying the *EXTraS* transients search pipeline. Specifically, and very briefly, the

---

[3]First *eROSITA*-DR1 data release:
https://erosita.mpe.mpg.de/dr1/
[4]eSASS cookbook:
https://erosita.mpe.mpg.de/edr/DataAnalysis/esasscookbook.html
[5]*EXTraS* Archive:
http://www.extras-fp7.eu/index.php/archive
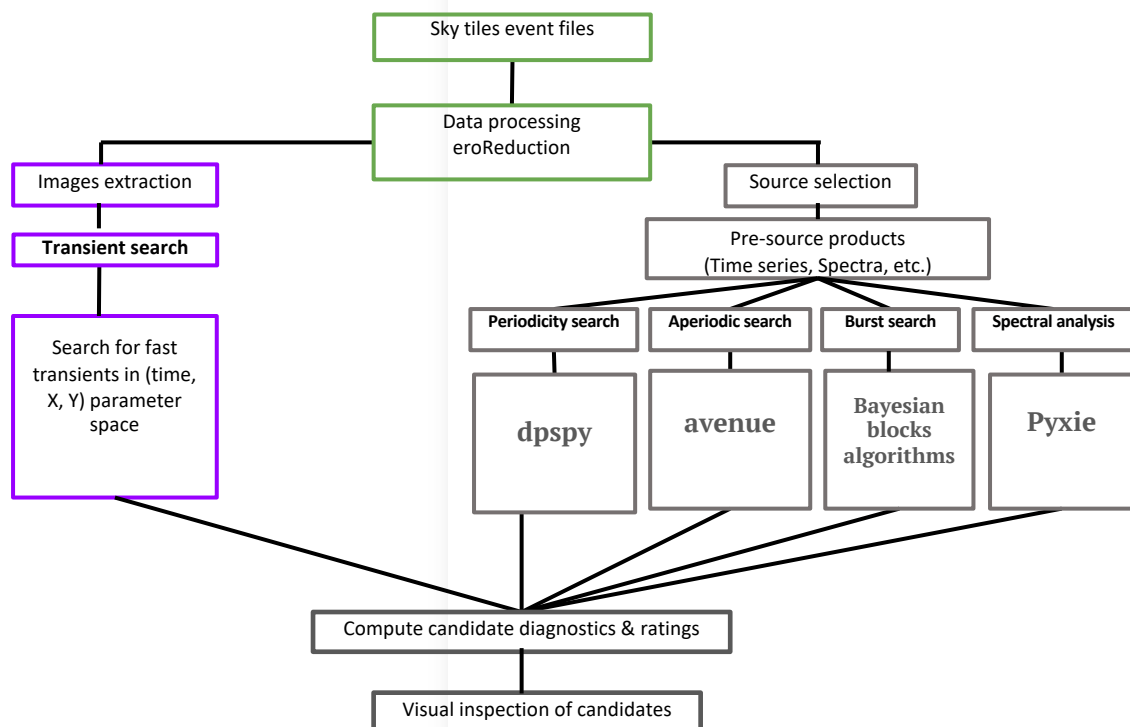
FIGURE 5.1: The design of *eBANDERAS* pipeline. Mission-independent steps with their modules are shown in gray and violet boxes. The data reduction with its associated modules are shown in green boxes.

pipeline consists of software scripts written in C-SHELL, C++ and PYTHON. It operates by dividing each *XMM–Newton* observation into time intervals and applying source detection to time-resolved images. The observations can be from a single *XMM–Newton* instrument – i.e. MOS1, MOS2, or pn – or a combination of them. The pipeline employs several approaches, one of which is the Bayesian Blocks algorithm (see Scargle et al., 2013). The algorithm identifies intervals where significant changes in the count rate occur by analysing small, overlapping regions (e.g., the default is $60'' \times 60''$ for the latest version) within the field of view.

The final products of this analysis include, among others, a catalogue of transient sources, a summary file and a sky image corresponding to each time interval where a transient was detected. Understanding these technical details is an essential step towards my primary goal of integrating the pipeline into our *eBANDERAS* framework using *eROSITA* data.

In parallel, I also plan to run the pipeline on the most recent *XMM–Newton* catalog, currently 4XMM−DR14 [6] (Webb et al., 2020), to take advantage of the latest data and improve the resulting catalog. By understanding the original pipeline and adapting it to the specific requirements of *eROSITA* data, my aim is to enhance the ability to detect and characterize X-ray transients within the *eROSITA* dataset.

---

[6]For the latest version of *XMM–Newton* catalogues, visit:
http://xmmssc.irap.omp.eu

6 Conclusions

In this thesis, we explored the complex phenomena of persistent emission and transient activities of magnetars—the most magnetised neutron stars—through multi-frequency observations. These phenomena provide a unique opportunity to investigate the emission physics of magnetars.

The research primarily focused on studying the temporal and spectral properties of magnetars X-ray and radio emissions during their bursts and outbursts phases. Characterised by their sudden and significant increases in X-ray fluxes, outbursts can help us better understand the nature and the properties of the emission on the magnetar surface and within the magnetosphere.

By utilising X-ray satellites (e.g. *XMM–Newton*, *NuSTAR*, *Swift*, *INTEGRAL*) and radio telescopes (e.g. *VLA*; *ASKAP*), we monitored the outbursts of magnetars Swift J1818.0−1607 and SGR J1935+2154 (see, Chapters. 2 and 3). The analysis of X-ray data collected for Swift J1818.0−1607 shows that its spectrum is best modeled by a combination of a blackbody and a power law at the peak of the outburst, with the power law component becoming undetectable as early as three days after the onset of the outburst. Studying the long-term spectral evolution of Swift J1818.0−1607 over a time span of about 19 months since the outburst onset, we found a rapid decrease in both the observed flux and the size of the thermally-emitting region of the source. However, no significant change was observed for the blackbody temperature, as it remains within 1 keV across the entire time span of the observations. From the timing analysis, we observed a significant variability in the spin-down evolution and estimated an average value for the spin-down rate of $\dot{v} = -2.3 \times 10^{-11} \, Hz^2$ ($\dot{P} = 4.2 \times 10^{-11} \, ss^{-1}$). Although this variability could stem from the impact of magnetospheric processes on spin behaviour during magnetar outbursts, it may also be attributed to the limitation and sparsity of the dataset used in this study.

Additionally, we identified a presence of diffuse emission associated with Swift J1818.0−1607, at both X-ray and radio wavelengths. The X-ray diffuse emission showed a soft X-ray spectrum and experienced a 30% decrease in flux over the course of seven months following the outburst, which is likely associated to a dust scattering halo. The diffuse radio emission, which is semi-circular in appearance, could be related to a supernova remnant associated with the magnetar, although further radio observations are necessary to confirm this and better understand its nature and evolutionary status.

In the case of SGR J1935+2154, we studied both the persistent and the burst X-ray spectra. The persistent emission is well described by a blackbody model plus powerlaw, representing the thermal and non-thermal components, respectively. In contrast, the bursts' spectra were best fit by a single blackbody model (see, Table B.1). We derived a phase-coherent timing solution with a spin frequency derivative of $\dot{v} = -5.25 \times 10^{-12} \, Hz^2$ ($\dot{P} = 5.52 \times 10^{-11} \, ss^{-1}$); a factor of ~ 4 times larger than the value measured during the first outburst of SGR J1935+2154 in 2014. This result suggests that the spin parameters of SGR J1935+2154 could vary during outburst due to relativistic winds. Similar to the significant spin-down variation observed in Swift J1818.0−1607, this change could also result from the rearrangement of the

magnetic fields within the magnetosphere of the magnetar.

In chapter 4, we conducted a search for isolated magnetic white dwarf pulsar ZTF J1901+1458 using archival data from *ASKAP* and *VLA* telescopes. Our analysis involved imaging data from an L-band *VLA* observation and from both the RACS and VAST *ASKAP* surveys. We did not detect any significant radio emission from ZTF J1901+1458 with sensitivity limits of 0.8 mJy and 0.4 mJy for *VLA* and *ASKAP*, respectively. The analysis also include a search for variability in the radio emission of the source, with no evidence of emission in 10-second timestep images from the *ASKAP* observations. These results highlight the need for continued observational efforts and/or preforming additional analysis to confirm any potential radio emission from ZTF J1901+1458.

In Chapter. 5, we outlined the development of the *eBANDERAS* project, which aims to build a mission-independent pipeline for detecting and analysing variability in X-ray data. The project seeks to build on the legacy of earlier efforts by integrating a systematic approach to searching for periodic and transients X-ray sources potentially in any X-ray mission with imaging capabilities. The focus in this chapter was primarily on the transient search module, which is being under development using methods from the *EXTraS* project. We discussed the current status and future direction of this component, including the study of the core *EXTraS* transient tools and the updates of the previous *EXTraS* catalog of transient sources. The update involved running the pipeline on the latest *XMM–Newton* catalog to incorporate the most recent data.

As the project progresses, the integration of these tools will be critical for advancing our ability to detect and analyse transient events in the X-ray sky.

List of Figures

List of Tables

A Appendix

A.1 Observation log of Swift J1818.0−1607

In this section we report observations log of Swift J1818.0−1607 carried out by *XMM–Newton NuSTAR* and *Swift* satellites.

TABLE A.1: Observation log of SwiftJ1818.0−1607, including the observations analysed by Esposito et al. (2020) above the double-horizontal solid lines.

Instrument	Obs.ID	Start YYYY-MM-DD hh:mm:ss (TT)	Stop YYYY-MM-DD hh:mm:ss (TT)	Exposure (ks)	Count rate (counts s^{-1})
Swift/XRT (PC)	00960986000	2020-03-12 21:18:22	2020-03-12 21:36:48	1.1	0.15 ± 0.01
Swift/XRT (PC)	00960986001	2020-03-12 22:57:45	2020-03-13 05:13:02	4.9	0.14 ± 0.01
Swift/XRT (WT)	00960986002	2020-03-13 20:47:55	2020-03-13 21:21:15	2.0	0.16 ± 0.01
Swift/XRT (PC)	00960986003	2020-03-15 00:10:37	2020-03-15 03:36:52	1.5	0.14 ± 0.01
NuSTAR/FPMA	80402308002	2020-03-15 03:58:21	2020-03-15 15:58:03	22.2	0.443 ± 0.005
XMM/EPIC-pn (LW)	0823591801	2020-03-15 07:57:47	2020-03-15 14:41:12	22.1	1.45 ± 0.01
Swift/XRT (WT)	00960986004	2020-03-19 09:33:11	2020-03-19 11:16:56	1.7	0.19 ± 0.02
Swift/XRT (WT)	00960986005	2020-03-20 04:34:19	2020-03-20 04:49:56	1.8	0.20 ± 0.01
Swift/XRT (WT)	00960986006	2020-03-22 02:35:21	2020-03-22 03:01:56	1.6	0.16 ± 0.01
Swift/XRT (WT)	00960986007	2020-03-24 05:51:38	2020-03-24 09:02:56	1.2	0.13 ± 0.01
Swift/XRT (WT)	00960986008	2020-03-26 05:40:29	2020-03-26 23:20:56	1.1	0.19 ± 0.01
Swift/XRT (WT)	00960986009	2020-03-28 03:40:53	2020-03-28 18:07:56	1.2	0.18 ± 0.02
Swift/XRT (WT)	00960986010	2020-03-29 16:25:13	2020-03-30 21:03:56	1.3	0.16 ± 0.01
Swift/XRT (WT)	00960986011	2020-04-01 19:17:34	2020-04-01 19:25:56	0.5	0.17 ± 0.02
NuSTAR/FPMA	80402308004	2020-04-04 02:01:09	2020-04-05 13:36:09	59.1	0.339 ± 0.002
XMM/EPIC-pn (FF)	0823593901	2020-04-04 03:44:15	2020-04-04 13:32:52	33.4	1.08 ± 0.01
Swift/XRT (WT)	00089033001	2020-04-05 05:51:22	2020-04-05 06:18:56	1.6	0.13 ± 0.01
Swift/XRT (WT)	00960986012	2020-04-17 11:22:40	2020-04-18 17:58:56	2.1	0.22 ± 0.01
Swift/XRT (WT)	00960986013	2020-04-21 01:15:46	2020-04-21 12:42:55	1.3	0.17 ± 0.01
Swift/XRT (WT)	00960986014	2020-05-02 07:58:09	2020-05-02 12:50:56	1.3	0.13 ± 0.02
NuSTAR/FPMA	80402308006	2020-05-02 20:56:09	2020-05-03 20:26:09	42.2	0.277 ± 0.003
Swift/XRT (PC)	00089033002	2020-05-02 22:22:26	2020-05-02 22:49:53	1.6	0.08 ± 0.01
Swift/XRT (PC)	00969823991^{c1}	2020-05-06 17:38:19	2020-05-06 17:48:46	0.6	0.08 ± 0.01

Continued on next page

TABLE A.1: Observation log of Swift J1818.0−1607, continued

Instrument	Obs.ID	Start YYYY-MM-DD hh:mm:ss (TT)	Stop YYYY-MM-DD hh:mm:ss (TT)	Exposure (ks)	Count rate (counts s^{-1})
Swift/XRT (PC)	00969823001[c1]	2020-05-06 18:43:12	2020-05-06 20:42:42	1.9	0.09 ± 0.01
Swift/XRT (WT)	00969823002	2020-05-13 05:39:09	2020-05-13 10:16:56	1.3	0.13 ± 0.01
Swift/XRT (WT)	00969823003	2020-05-15 05:19:42	2020-05-15 20:02:56	1.6	0.13 ± 0.01
Swift/XRT (PC)	00972614991	2020-05-16 15:04:54	2020-05-16 16:27:25	1.7	0.08 ± 0.01
Swift/XRT (WT)	00969823004	2020-05-21 20:38:46	2020-05-21 22:24:56	1.9	0.10 ± 0.01
Swift/XRT (WT)	00969823005	2020-05-28 00:46:46	2020-05-28 20:09:56	2.5	0.14 ± 0.01
Swift/XRT (WT)	00969823006	2020-06-04 08:14:35	2020-06-04 18:08:56	2.7	0.12 ± 0.01
Swift/XRT (WT)	00969823007[c2]	2020-06-12 01:11:04	2020-06-13 07:21:56	1.5	0.13 ± 0.01
Swift/XRT (WT)	00969823008[c2]	2020-06-15 08:53:23	2020-06-15 12:12:55	0.4	0.12 ± 0.02
Swift/XRT (WT)	00969823009[c2]	2020-06-18 19:16:44	2020-06-18 19:21:56	0.3	0.10 ± 0.02
Swift/XRT (WT)	00969823010	2020-06-21 20:47:49	2020-06-22 21:07:56	3.1	0.05 ± 0.01
Swift/XRT (WT)	00969823011	2020-06-25 05:54:07	2020-06-25 23:46:56	3.1	0.07 ± 0.01
NuSTAR/FPMA	80402308008	2020-06-30 02:46:09	2020-06-30 15:16:09	23.5	0.129 ± 0.002
NuSTAR/FPMA	80402308010	2020-07-01 19:01:09	2020-07-02 01:01:09	12.3	0.161 ± 0.003
Swift/XRT (PC)	00089033003	2020-07-01 19:49:42	2020-07-01 20:12:54	1.4	0.041 ± 0.006
Swift/XRT (PC)	00980513991	2020-07-02 07:11:35	2020-07-02T08:34:14	1.7	0.061 ± 0.006
Swift/XRT (WT)	00969823012	2020-07-02 08:49:43	2020-07-02 16:22:56	1.7	0.059 ± 0.006
Swift/XRT (PC)	00089033004	2020-07-10 01:31:26	2020-07-10 08:10:54	3.6	0.059 ± 0.004
Swift/XRT (PC)	00089033005	2020-07-26 12:23:40	2020-07-26 18:58:52	3.8	0.050 ± 0.003
Swift/XRT (PC)	00089033006[c3]	2020-08-07 03:12:00	2020-08-07 08:10:52	2.8	0.057 ± 0.005
Swift/XRT (PC)	00089033007[c3]	2020-08-12 17:14:14	2020-08-12 17:33:52	1.2	0.031 ± 0.005
Swift/XRT (PC)	00089033008	2020-08-21 00:20:13	2020-08-21 14:47:27	3.0	0.044 ± 0.004
Swift/XRT (PC)	00089033009[c4]	2020-09-04 07:12:43	2020-09-04 10:36:53	1.4	0.041 ± 0.006
NuSTAR/FPMA	80402308012[d]	2020-09-07 00:41:09	2020-09-08 00:11:09	39.3	0.097 ± 0.001

TABLE A.1: Observation log of Swift J1818.0−1607, continued

Instrument	Obs.ID	Start YYYY-MM-DD hh:mm:ss (TT)	Stop YYYY-MM-DD hh:mm:ss (TT)	Exposure (ks)	Count rate (counts s^{-1})
XMM/EPIC-pn (FF)	0823594001	2020-09-07 15:12:48	2020-09-07 22:38:50	26.7	0.429 ± 0.005
Swift/XRT (PC)	00089033010[c4]	2020-09-07 17:58:15	2020-09-07 19:30:52	2.0	0.043 ± 0.005
Swift/XRT (PC)	00089033011	2020-09-11 17:17:33	2020-09-12 04:34:52	4.8	0.044 ± 0.003
Swift/XRT (PC)	00089033012	2020-09-26 00:03:15	2020-09-26 20:39:53	4.5	0.040 ± 0.003
XMM/EPIC-pn (FF)	0823594201	2020-10-08 10:24:17	2020-10-09 00:49:31	49.4	0.288 ± 0.004
Swift/XRT (PC)	00089033013	2020-10-08 14:47:04	2020-10-09 20:58:54	4.8	0.036 ± 0.003
Swift/XRT (PC)	03110882001	2020-10-19 08:54:19	2020-10-19 23:37:52	4.7	0.037 ± 0.003
Swift/XRT (PC)	00089033014	2020-10-25 09:43:50	2020-10-26 23:59:52	4.2	0.038 ± 0.003
Swift/XRT (PC)	00089033015	2020-11-06 06:55:28	2020-11-06 16:48:54	4.2	0.035 ± 0.003
Swift/XRT (PC)	00013996001	2021-02-15 09:24:24	2021-02-15 22:35:52	4.5	0.018 ± 0.002
Swift/XRT (PC)	00013996002	2021-03-01 00:16:23	2021-03-01 21:05:53	3.8	0.013 ± 0.002
Swift/XRT (PC)	00013996003	2021-03-15 14:26:25	2021-03-15 17:58:53	4.6	0.009 ± 0.002
Swift/XRT (PC)	00013996004	2021-03-29 01:52:19	2021-03-29 10:10:54	4.5	0.009 ± 0.001
Swift/XRT (PC)	00013996005	2021-04-12 03:40:52	2021-04-12 18:18:52	4.3	0.011 ± 0.002
Swift/XRT (PC)	00013996006	2021-04-26 02:28:48	2021-04-26 23:20:53	4.2	0.010 ± 0.002
Swift/XRT (PC)	00013996007	2021-05-10 02:30:39	2021-05-10 20:22:55	4.5	0.008 ± 0.002
Swift/XRT (PC)	00013996008[c5]	2021-05-24 02:30:31	2021-05-24 10:38:17	2.3	0.008 ± 0.002
Swift/XRT (PC)	00013996009[c5]	2021-05-29 19:27:09	2021-05-29 22:51:54	2.4	0.005 ± 0.002
Swift/XRT (PC)	00013996010[c5]	2021-06-06 03:11:41	2021-06-07 22:04:51	1.6	0.010 ± 0.002
Swift/XRT (PC)	00013996011[c6]	2021-06-26 18:32:43	2021-06-26 18:41:52	0.5	0.008 ± 0.004
Swift/XRT (PC)	00013996012[c6]	2021-06-28 00:48:50	2021-06-28 18:02:52	1.0	0.007 ± 0.003
Swift/XRT (PC)	00013996013[c6]	2021-06-29 06:56:55	2021-06-29 21:32:54	2.1	0.007 ± 0.002
Swift/XRT (PC)	00013996014[c6]	2021-06-30 02:07:20	2021-06-30 14:40:52	2.7	0.008 ± 0.002
Swift/XRT (PC)	00013996015[c7]	2021-07-05 11:13:57	2021-07-06 17:19:06	1.0	0.007 ± 0.003

TABLE A.1: Observation log of Swift J1818.0−1607, continued

Instrument	Obs.ID	Start YYYY-MM-DD hh:mm:ss (TT)	Stop YYYY-MM-DD hh:mm:ss (TT)	Exposure (ks)	Count rate (counts s^{-1})
Swift/XRT (PC)	00013996016[c7]	2021-07-08 01:13:22	2021-07-08 12:38:52	0.6	0.002 ± 0.002
Swift/XRT (PC)	00013996017[c7]	2021-07-13 06:45:26	2021-07-13 18:11:53	2.6	0.005 ± 0.002
Swift/XRT (PC)	00013996018[c7]	2021-07-18 01:52:35	2021-07-18 23:59:52	0.3	0.005 ± 0.001
Swift/XRT (PC)	00013996019[c8]	2021-08-08 10:46:46	2021-08-08 12:26:54	0.6	0.010 ± 0.005
Swift/XRT (PC)	00013996020[c8]	2021-08-10 08:34:29	2021-08-10 08:45:53	0.7	0.010 ± 0.004
Swift/XRT (PC)	00013996021[c9]	2021-09-24 02:13:29	2021-09-24 23:07:52	4.1	0.006±0.001
Swift/XRT (PC)	00013996022[c9]	2021-10-24 02:27:38	2021-10-25 15:15:53	4.4	0.004±0.001

The instrumental setup is indicated in paren-
theses: PC = photon counting, WT = windowed
timing, LW = large window, and FF = full
frame.
The count rate is in the 0.3–10 keV energy
range, except for NuSTAR (3–10 keV).
Observations with the same superscripts were
merged for the spectral analysis.
Data collected with FPMB were not included in
the analysis as they are heavily affected by stray
light contamination.

B Appendix

B.1 Log of SGR J1935+2154 short X-ray bursts

Table B.1 lists the epochs, fluence, durations, best-fit spectral parameters and unabsorbed fluxes for the bursts detected in our datasets. The fluence refers to the 3–79 keV and 0.2–12 keV ranges for *NuSTAR* and *XMM–Newton* bursts, respectively. The duration has to be considered as an approximate value. We estimated it by summing the 15.625-ms time bins showing enhanced emission for the structured bursts, and by setting it equal to the coarser time resolution at which the burst is detected in all the other cases.

TABLE B.1: Log of X-ray bursts detected in all datasets and results of the spectral analysis for the brightest events. The N_H has been fixed to the average value in the spectral fits.

Instrument/Obs.ID	Burst epoch YYYY-MM-DD hh:mm:ss (TDB)	Fluence (counts)	Duration (ms)	kT_{BB} (keV)	R_{BB} (km)	$F_{X,unabs}$ ($\times 10^{-9}$ erg s^{-1} cm^{-2})	χ^2/ W-stat (dof)
XMM/0902334101 #1†	2022-10-15 20:26:14.457	17	31.25				
#2†	2022-10-16 00:41:42.870	11	62.5				
#3*	03:53:09.083	55	109.375	$1.5^{+0.2}_{-0.2}$	$3.0^{+0.8}_{-0.6}$	0.9 ± 0.1	χ^2=15.86 (14)
#4	10:35:28.285	31	62.5	$1.7^{+0.7}_{-0.4}$	$7.6^{+5.2}_{-2.4}$	10 ± 3	W-stat=21.55 (11)
#5	10:45:11.000	10	62.5				
#6	10:45:14.351	61	109.375	$2.2^{+0.8}_{-0.5}$	$4.6^{+2.1}_{-1.2}$	9 ± 2	χ^2=5.14 (6)
#7	12:05:02.934	29	62.5	$1.4^{+0.4}_{-0.2}$	$7.7^{+3.7}_{-2.0}$	5 ± 1	W-stat=13.54 (16)
NuSTAR/80702311002 #1	2022-10-19 06:29:29.769	25	46.875				
#2	07:56:58.869	13	125				
#3	08:21:05.061	8	62.5				
#4	09:48:56.934	21	46.875				
#5†	11:33:02.606	20	46.875				
#6†	13:21:31.841	30	62.5				
#7†	17:24:38.512	12	31.25				
#8†	17:46:13.429	15	125				
#9	2022-10-20 00:13:17.634	80	171.875	$3.1^{+0.6}_{-0.4}$	$1.0^{+0.8}_{-0.6}$	1.2 ± 0.2	W-stat=10.87 (17)
XMM/0882184001 #1	2022-10-22 03:59:47.011	16	62.5				
#2	04:27:31.542	9	31.25				
#3	04:46:13.754	110	218.75	$2.2^{+0.4}_{-0.3}$	$3.9^{+1.0}_{-0.7}$	5.9 ± 0.8	χ^2=4.15 (6)
#4	04:53:17.448	20	62.5				
#5	05:01:16.104	14	62.5				
#6	06:12:48.464	20	125				
#7	06:18:35.417	28	93.75	$2.6^{+1.8}_{-0.7}$	$3.2^{+2.3}_{-1.1}$	7 ± 2	W-stat=14.42 (13)
#8	09:29:20.325	27	93.75	$1.9^{+0.4}_{-0.4}$	$4.9^{+2.9}_{-1.4}$	6 ± 2	W-stat=11.01 (14)
#9	10:01:26.472	132	187.5	$2.3^{+0.4}_{-0.6}$	$4.0^{+1.4}_{-0.9}$	7 ± 1	χ^2=7.33 (6)
#10	14:18:57.919	27	125	$1.4^{+0.4}_{-0.3}$	$3.1^{+1.8}_{-0.8}$	0.8 ± 0.2	χ^2=2.74 (4)
#11	15:41:35.417	12	62.5				
#12	16:25:01.920	30	156.25	$2.4^{+1.2}_{-0.6}$	$2.9^{+1.7}_{-0.9}$	4 ± 1	W-stat=13.08 (18)
#13	16:31:33.816	123	203.125	$1.9^{+0.3}_{-0.3}$	$4.8^{+1.3}_{-0.9}$	5.3 ± 0.7	χ^2=14.13 (8)
#14	16:42:44.030	28	125	$0.8^{+0.2}_{-0.2}$	$12.9^{+8.0}_{-3.7}$	1.5 ± 0.4	W-stat=4.91 (8)
#15	17:37:26.814	290	531.25	2.1 ± 0.2	$3.4^{+0.5}_{-0.4}$	4.0 ± 0.3	χ^2=21.87 (24)
NuSTAR/80702311004 #1	2022-10-22 22:57:23.582	23	62.5				
#2	2022-10-23 21:58:05.838	10	62.5				
#3	22:50:23.135	27	62.5				

* Burst detected also with *INTEGRAL*.

† These bursts were covered by radio observations (for details, see Table 3.3).

† The flux was estimated in the 0.5–10 keV range for *XMM–Newton* and *NuSTAR*.

The notation # N corresponds to the burst number in a given observation.

Bibliography

Agarwal, Devansh et al. (Sept. 2020). "FETCH: A deep-learning based classifier for fast transient classification". In: *MNRAS* 497.2, pp. 1661–1674. DOI: 10.1093/mnras/staa1856. arXiv: 1902.06343 [astro-ph.IM].

Arnaud, K. A. (1996). "XSPEC: The First Ten Years". In: *XSPEC: The First Ten Years*. Ed. by G. H. Jacoby and J. Barnes. Vol. 101. Astronomical Data Analysis Software and Systems V. ASP, San Francisco, pp. 17–20.

Baade, W. and F. Zwicky (July 1934). "Remarks on Super-Novae and Cosmic Rays". In: *Physical Review* 46.1, pp. 76–77. DOI: 10.1103/PhysRev.46.76.2.

Baring, M. G. and A. K. Harding (Apr. 2007). "Resonant Compton upscattering in anomalous X-ray pulsars". In: *Ap&SS* 308, pp. 109–118. DOI: 10.1007/s10509-007-9326-x. eprint: arXiv:astro-ph/0610382.

Barthelmy, S. D. et al. (Oct. 2005). "The Burst Alert Telescope (BAT) on the SWIFT Midex Mission". In: *Space Science Reviews* 120, pp. 143–164.

Beloborodov, A. M. (Feb. 2002). "Gravitational Bending of Light Near Compact Objects". In: *ApJ* 566, pp. L85–L88. DOI: 10.1086/339511. eprint: arXiv:astro-ph/0201117.

— (Sept. 2009). "Untwisting Magnetospheres of Neutron Stars". In: *ApJ* 703, pp. 1044–1060. DOI: 10.1088/0004-637X/703/1/1044. arXiv: 0812.4873.

Blumer, Harsha and Samar Safi-Harb (Dec. 2020). "Chandra Observations of the Newly Discovered Magnetar Swift J1818.0-1607". In: *ApJ* 904.2, L19, p. L19. DOI: 10.3847/2041-8213/abc6a2. arXiv: 2011.00324 [astro-ph.HE].

Bochenek, C. D. et al. (2020). "A fast radio burst associated with a Galactic magnetar". In: *Nature* 587.7832, pp. 59–62. DOI: 10.1038/s41586-020-2872-x. URL: https://doi.org/10.1038/s41586-020-2872-x.

Bogdanov, Slavko and Wynn Ho (June 2024). "The "Magnificent Seven" X-Ray Isolated Neutron Stars Revisited. I. Improved Timing Solutions and Pulse Profile Analysis". In: *The Astrophysical Journal* 969, p. 53. DOI: 10.3847/1538-4357/ad452b.

Borghese, A. et al. (Apr. 2019). "The multi-outburst activity of the magnetar in Westerlund I". In: *MNRAS* 484.3, pp. 2931–2943. DOI: 10.1093/mnras/stz084. arXiv: 1901.02026 [astro-ph.HE].

Borghese, A. et al. (Oct. 2020). "The X-Ray Reactivation of the Radio Bursting Magnetar SGR J1935+2154". In: *ApJ* 902.1, L2, p. L2. DOI: 10.3847/2041-8213/aba82a. arXiv: 2006.00215 [astro-ph.HE].

Borghese, A. et al. (July 2021). "The X-ray evolution and geometry of the 2018 outburst of XTE J1810-197". In: *MNRAS* 504.4, pp. 5244–5257. DOI: 10.1093/mnras/stab1236. arXiv: 2104.11083 [astro-ph.HE].

Borghese, A. et al. (Oct. 2022). "The first seven months of the 2020 X-ray outburst of the magnetar SGR J1935+2154". In: *MNRAS* 516.1, pp. 602–616. DOI: 10.1093/mnras/stac1314. arXiv: 2205.04983 [astro-ph.HE].

Borghese, Alice and Paolo Esposito (2023). *Isolated Neutron Stars*. arXiv: 2311.08353 [astro-ph.HE].

Burrows, D. N. et al. (Oct. 2005a). "The Swift X-Ray Telescope". In: *Space Science Reviews* 120, pp. 165–195.

Burrows, David N. et al. (Oct. 2005b). "The Swift X-Ray Telescope". In: *Space Sci. Rev.* 120.3-4, pp. 165–195. DOI: 10.1007/s11214-005-5097-2. arXiv: astro-ph/0508071 [astro-ph].

Caiazzo, Ilaria et al. (June 2021). "A highly magnetized and rapidly rotating white dwarf as small as the Moon". In: *Nature* 595.7865, pp. 39–42. DOI: 10.1038/s41586-021-03615-y. arXiv: 2107.08458 [astro-ph.SR].

Camilo, F. et al. (Aug. 2006). "Transient pulsed radio emission from a magnetar". In: *Nature* 442, pp. 892–895. DOI: 10.1038/nature04986. eprint: arXiv:astro-ph/0605429.

Camilo, F. et al. (Sept. 2007). "1E 1547.0-5408: A Radio-emitting Magnetar with a Rotation Period of 2 Seconds". In: *ApJ* 666, pp. L93–L96.

Chadwick, J. (Feb. 1932). "Possible Existence of a Neutron". In: *Nature* 129.3252, p. 312. DOI: 10.1038/129312a0.

Champion, David et al. (Nov. 2020a). "High-cadence observations and variable spin behaviour of magnetar Swift J1818.0-1607 after its outburst". In: *MNRAS* 498.4, pp. 6044–6056. DOI: 10.1093/mnras/staa2764. arXiv: 2009.03568 [astro-ph.HE].

Champion, David et al. (Mar. 2020b). "Spin-evolution of the new magnetar J1818.0-1607". In: *Astron. Tel.* 13559, p. 1.

Chandrasekhar, S. (July 1931). "The Maximum Mass of Ideal White Dwarfs". In: *ApJ* 74, p. 81. DOI: 10.1086/143324.

CHIME/FRB Collaboration et al. (Nov. 2020). "A bright millisecond-duration radio burst from a Galactic magnetar". In: *Nature* 587.7832, pp. 54–58. DOI: 10.1038/s41586-020-2863-y. arXiv: 2005.10324 [astro-ph.HE].

CHIME/FRB Collaboration Andersen, B. C. et al. (2020). "A bright millisecond-duration radio burst from a Galactic magnetar". In: *Nature* 587.7832, pp. 54–58. DOI: 10.1038/s41586-020-2863-y. URL: https://doi.org/10.1038/s41586-020-2863-y.

Comella, J. M. et al. (Feb. 1969). "Crab Nebula Pulsar NP 0532". In: *Nature* 221.5179, pp. 453–454. DOI: 10.1038/221453a0.

Comrie, Angus et al. (Mar. 2021). *CARTA: Cube Analysis and Rendering Tool for Astronomy*. Astrophysics Source Code Library, record ascl:2103.031.

Coti Zelati, F. et al. (Feb. 2018). "Systematic study of magnetar outbursts". In: *MNRAS* 474, pp. 961–1017.

Coti Zelati, Francesco et al. (Jan. 2020). "The long-term enhanced brightness of the magnetar 1E 1547.0-5408". In: *A&A* 633, A31, A31.

De Grandis, Davide et al. (June 2021). "X-Ray Emission from Isolated Neutron Stars Revisited: 3D Magnetothermal Simulations". In: *ApJ* 914.2, 118, p. 118. DOI: 10.3847/1538-4357/abfdac. arXiv: 2105.00684 [astro-ph.HE].

De Luca, A. (2017). "Central Compact Objects in Supernova Remnants". In: *International Conference Physics of Neutron Stars - 2017. 50 years after, St. Petersburg, Russian Federation*. Ed. by G. G. Pavlov et al. Vol. 932. Journal of Physics Conference Series, 012006, p. 012006.

De Luca, A. et al. (June 2021). "The EXTraS project: Exploring the X-ray transient and variable sky". In: *A&A* 650, A167, A167. DOI: 10.1051/0004-6361/202039783. arXiv: 2105.02895 [astro-ph.HE].

Dhillon, V. S. et al. (Sept. 2011). "The first observation of optical pulsations from a soft gamma repeater: SGR 0501+4516". In: *MNRAS* 416, pp. L16–L20. DOI: 10.1111/j.1745-3933.2011.01088.x. arXiv: 1106.1355 [astro-ph.SR].

Dib, R., V. M. Kaspi, and F. P. Gavriil (Feb. 2008). "Glitches in Anomalous X-Ray Pulsars". In: *ApJ* 673, pp. 1044–1061. DOI: 10.1086/524653.

Ding, Hao et al. (Jan. 2022). "Probing magnetar formation channels with high-precision astrometry: The progress of VLBA astrometry of the fastest-spinning magnetar Swift J1818.0-1607". In: *arXiv e-prints*, arXiv:2201.07376, arXiv:2201.07376. arXiv: 2201.07376 [astro-ph.HE].

Dubner, Gloria and Elsa Giacani (Sept. 2015). "Radio emission from supernova remnants". In: *A&ARv* 23, 3, p. 3. DOI: 10.1007/s00159-015-0083-5. arXiv: 1508.07294 [astro-ph.HE].

Duchesne, S. W. et al. (Aug. 2023). "The Rapid ASKAP Continuum Survey IV: continuum imaging at 1367.5 MHz and the first data release of RACS-mid". In: *Publ. Astron. Soc. Australia* 40, e034, e034. DOI: 10.1017/pasa.2023.31. arXiv: 2306.07194 [astro-ph.IM].

Duncan, R. C. and C. Thompson (June 1992). "Formation of very strongly magnetized neutron stars - Implications for gamma-ray bursts". In: *ApJ* 392, pp. L9–L13.

Eatough, R. P. et al. (Sept. 2013). "A strong magnetic field around the supermassive black hole at the centre of the Galaxy". In: *Nature* 501, pp. 391–394. DOI: 10.1038/nature12499. arXiv: 1308.3147 [astro-ph.GA].

Enoto, T. et al. (July 2017). "Magnetar Broadband X-Ray Spectra Correlated with Magnetic Fields: Suzaku Archive of SGRs and AXPs Combined with NuSTAR, Swift, and RXTE". In: *ApJS* 231, 8, p. 8. DOI: 10.3847/1538-4365/aa6f0a. arXiv: 1704.07018 [astro-ph.HE].

Enoto, Teruaki et al. (Mar. 2020). "NICER detection of 1.36 sec periodicity from a new magnetar, Swift J1818.0-1607". In: *Astron. Tel.* 13551, p. 1.

Esposito, P. et al. (June 2020). "A Very Young Radio-loud Magnetar". In: *ApJ* 896.2, L30, p. L30. DOI: 10.3847/2041-8213/ab9742. arXiv: 2004.04083 [astro-ph.HE].

Esposito, Paolo, Nanda Rea, and Gian Luca Israel (Jan. 2021). "Magnetars: A Short Review and Some Sparse Considerations". In: *Astrophysics and Space Science Library*. Ed. by Tomaso M. Belloni, Mariano Méndez, and Chengmin Zhang. Vol. 461. Astrophysics and Space Science Library, pp. 97–142. DOI: 10.1007/978-3-662-62110-3_3. arXiv: 1803.05716 [astro-ph.HE].

Evans, P. A. et al. (Mar. 2020). "Swift-BAT trigger 960986: Swift detection of a new SGR Swift J1818.0-1607". In: *GRB Coordinates Network* 27373, p. 1.

Fahlman, G. G. and P. C. Gregory (Sept. 1981). "An X-ray pulsar in SNR G109.1-1.0". In: *Nature* 293, pp. 202–204.

Filipović, Miroslav D. et al. (May 2022). "Mysterious odd radio circle near the large magellanic cloud - an intergalactic supernova remnant?" In: *MNRAS* 512.1, pp. 265–284. DOI: 10.1093/mnras/stac210. arXiv: 2201.10026 [astro-ph.HE].

Freire, Paulo C. C. and Alessandro Ridolfi (June 2018). "An algorithm for determining the rotation count of pulsars". In: *MNRAS* 476.4, pp. 4794–4805. DOI: 10.1093/mnras/sty524. arXiv: 1802.07211 [astro-ph.IM].

Gabriel, C. et al. (July 2004). "The XMM-Newton SAS - Distributed Development and Maintenance of a Large Science Analysis System: A Critical Analysis". In: *Astronomical Data Analysis Software and Systems (ADASS) XIII*. Ed. by Francois Ochsenbein, Mark G. Allen, and Daniel Egret. Vol. 314. Astronomical Society of the Pacific Conference Series, p. 759.

Gavriil, F. P., V. M. Kaspi, and P. M. Woods (June 2004). "A Comprehensive Study of the X-Ray Bursts from the Magnetar Candidate 1E 2259+586". In: *ApJ* 607, pp. 959–969. DOI: 10.1086/383564. eprint: arXiv:astro-ph/0310852.

Gehrels, N. et al. (Aug. 2004). "The Swift Gamma-Ray Burst Mission". In: *ApJ* 611, pp. 1005–1020.

Gendreau, Keith C. et al. (July 2016). "The Neutron star Interior Composition Explorer (NICER): design and development". In: *Space Telescopes and Instrumentation 2016: Ultraviolet to Gamma Ray*. Ed. by Jan-Willem A. den Herder, Tadayuki Takahashi, and Marshall Bautz. Vol. 9905. Society of Photo-Optical Instrumentation Engineers (SPIE) Conference Series, 99051H, 99051H. DOI: 10.1117/12.2231304.

Ghizzardi, S. (2002). " In-flight calibration of the PSF for the PN camera". In: *XMM–Newton Calibration Report* EPIC-MCT-TN-012.

Giacconi, R. et al. (Apr. 1971). "An X-Ray Scan of the Galactic Plane from UHURU". In: *ApJ* 165, p. L27.

Gold, T. (May 1968). "Rotating Neutron Stars as the Origin of the Pulsating Radio Sources". In: *Nature* 218.5143, pp. 731–732. DOI: 10.1038/218731a0.

Gotthelf, E. V., R. Perna, and J. P. Halpern (Dec. 2010). "Modeling the Surface X-ray Emission and Viewing Geometry of PSR J0821-4300 in Puppis A". In: *ApJ* 724, pp. 1316–1324. DOI: 10.1088/0004-637X/724/2/1316. arXiv: 1009.4473 [astro-ph.HE].

Götz, D. et al. (2006). "Two years of INTEGRAL monitoring of the soft gamma-ray repeater SGR 1806-20: from quiescence to frenzy". In: *A&A* 445.1, pp. 313–321. DOI: 10.1051/0004-6361:20053648. URL: https://doi.org/10.1051/0004-6361:20053648.

Gourgouliatos, Konstantinos N. and Samuel K. Lander (Sept. 2021). "Axisymmetric magneto-plastic evolution of neutron-star crusts". In: *MNRAS* 506.3, pp. 3578–3587. DOI: 10.1093/mnras/stab1869. arXiv: 2106.03869 [astro-ph.HE].

Guzman, Juan et al. (Dec. 2019). *ASKAPsoft: ASKAP science data processor software.* Astrophysics Source Code Library, record ascl:1912.003.

Harrison, F. A. et al. (June 2013). "The Nuclear Spectroscopic Telescope Array (NuSTAR) High-energy X-Ray Mission". In: *ApJ* 770, 103, p. 103.

Hewish, A. et al. (Feb. 1968). "Observation of a Rapidly Pulsating Radio Source". In: *Nature* 217.5130, pp. 709–713. DOI: 10.1038/217709a0.

Hotan, A. W. et al. (Mar. 2021). "Australian square kilometre array pathfinder: I. system description". In: *Publ. Astron. Soc. Australia* 38, e009, e009. DOI: 10.1017/pasa.2021.1. arXiv: 2102.01870 [astro-ph.IM].

Hu, Chin-Ping et al. (Oct. 2020). "NICER Observation of the Temporal and Spectral Evolution of Swift J1818.0-1607: A Missing Link between Magnetars and Rotation-powered Pulsars". In: *ApJ* 902.1, 1, p. 1. DOI: 10.3847/1538-4357/abb3c9. arXiv: 2009.00231 [astro-ph.HE].

Huang, Zhi-Peng et al. (July 2021). "Simultaneous 2.25/8.60 GHz observations of the newly discovered magnetar - Swift J1818.0-1607". In: *MNRAS* 505.1, pp. 1311–1315. DOI: 10.1093/mnras/stab1362. arXiv: 2105.03580 [astro-ph.HE].

Hurley, K. et al. (1999). "A giant periodic flare from the soft gamma-ray repeater SGR 1900+14." In: *Nature* 397, pp. 41–43.

Hurley, K. et al. (Apr. 2005). "An exceptionally bright flare from SGR 1806-20 and the origins of short-duration γ-ray bursts". In: *Nature* 434.7037, pp. 1098–1103. DOI: 10.1038/nature03519. arXiv: astro-ph/0502329 [astro-ph].

Hurley-Walker, N. et al. (Jan. 2022). "A radio transient with unusually slow periodic emission". In: *Nature* 601.7894, pp. 526–530. DOI: 10.1038/s41586-021-04272-x.

Hurley-Walker, N. et al. (July 2023). "A long-period radio transient active for three decades". In: *Nature* 619.7970, pp. 487–490. DOI: 10.1038/s41586-023-06202-5.

Ibrahim, A. Y. et al. (Nov. 2022). "XMM-Newton and NuSTAR observations of SGR 1935+2154 during its latest activation in 2022 October". In: *The Astronomer's Telegram* 15745, p. 1.

Ibrahim, A. Y. et al. (Jan. 2023). "Deep X-Ray and Radio Observations of the First Outburst of the Young Magnetar Swift J1818.0-1607". In: *ApJ* 943.1, 20, p. 20. DOI: 10.3847/1538-4357/aca528. arXiv: 2211.12391 [astro-ph.HE].

Ibrahim, A. Y. et al. (Apr. 2024). "An X-Ray and Radio View of the 2022 Reactivation of the Magnetar SGR J1935+2154". In: *ApJ* 965.1, 87, p. 87. DOI: 10.3847/1538-4357/ad293b. arXiv: 2402.08596 [astro-ph.HE].

Israel, G. L. et al. (Nov. 2016a). "The Chandra ACIS Timing Survey Project: glimpsing a sample of faint X-ray pulsators". In: *MNRAS* 462.4, pp. 4371–4385. DOI: 10.1093/mnras/stw1897. arXiv: 1608.00077 [astro-ph.HE].

Israel, G. L. et al. (Apr. 2016b). "The discovery, monitoring and environment of SGR J1935+2154". In: *MNRAS* 457.4, pp. 3448–3456. DOI: 10.1093/mnras/stw008. arXiv: 1601.00347 [astro-ph.HE].

Israel, G. L. et al. (Jan. 2021). "X-Ray and Radio Bursts from the Magnetar 1E 1547.0-5408". In: *ApJ* 907.1, 7, p. 7. DOI: 10.3847/1538-4357/abca95. arXiv: 2011.06607 [astro-ph.HE].

Jansen, F. et al. (Jan. 2001). "XMM-Newton observatory. I. The spacecraft and operations". In: *A&A* 365, pp. L1–L6. DOI: 10.1051/0004-6361:20000036.

Johnston, Simon and Matthew Kerr (Mar. 2018). "Polarimetry of 600 pulsars from observations at 1.4 GHz with the Parkes radio telescope". In: *MNRAS* 474.4, pp. 4629–4636. DOI: 10.1093/mnras/stx3095. arXiv: 1711.10092 [astro-ph.HE].

Karuppusamy, Ramesh et al. (Mar. 2020). "Detection of pulsed radio emission from new magnetar Swift J1818.0-1607". In: *Astron. Tel.* 13553, p. 1.

Kaspi, V. M. and A. M. Beloborodov (Aug. 2017). "Magnetars". In: *ARA&A* 55, pp. 261–301.

Kirsten, F. et al. (Apr. 2021). "Detection of two bright radio bursts from magnetar SGR 1935 + 2154". In: *Nature Astronomy* 5, pp. 414–422. DOI: 10.1038/s41550-020-01246-3. arXiv: 2007.05101 [astro-ph.HE].

Kirsten, F. et al. (Feb. 2022). "A repeating fast radio burst source in a globular cluster". In: *Nature* 602.7898, pp. 585–589. DOI: 10.1038/s41586-021-04354-w. arXiv: 2105.11445 [astro-ph.HE].

Kouveliotou, C. et al. (1998). "An X-ray pulsar with a superstrong magnetic field in the soft gamma-ray repeater SGR 1806-20." In: *Nature* 393, pp. 235–237.

Kouveliotou, C. et al. (Jan. 1999). "Discovery of a Magnetar Associated with the Soft Gamma Repeater SGR 1900+14". In: *ApJ* 510, pp. L115–L118.

Kozlova, A. V. et al. (Aug. 2016). "The first observation of an intermediate flare from SGR 1935+2154". In: *MNRAS* 460.2, pp. 2008–2014. DOI: 10.1093/mnras/stw1109. arXiv: 1605.02993 [astro-ph.HE].

Large, M. I., A. E. Vaughan, and B. Y. Mills (Oct. 1968). "A Pulsar Supernova Association?" In: *Nature* 220.5165, pp. 340–341. DOI: 10.1038/220340a0.

Lebrun, F. et al. (Nov. 2003). "ISGRI: The INTEGRAL Soft Gamma-Ray Imager". In: *A&A* 411, pp. L141–L148. DOI: 10.1051/0004-6361:20031367. arXiv: astro-ph/0310362 [astro-ph].

Levin, L. et al. (Sept. 2010). "A Radio-loud Magnetar in X-ray Quiescence". In: *ApJ* 721, pp. L33–L37. DOI: 10.1088/2041-8205/721/1/L33. arXiv: 1007.1052 [astro-ph.HE].

Li, C. K. et al. (Apr. 2021). "HXMT identification of a non-thermal X-ray burst from SGR J1935+2154 and with FRB 200428". In: *Nature Astronomy* 5, pp. 378–384. DOI: 10.1038/s41550-021-01302-6. arXiv: 2005.11071 [astro-ph.HE].

Li, T., Y. Shao, and X.-D. Li (June 2016). "Can the Subsonic Accretion Model Explain the Spin Period Distribution of Wind-fed X-Ray Pulsars?" In: *ApJ* 824, 143, p. 143. DOI: 10.3847/0004-637X/824/2/143. arXiv: 1605.03669 [astro-ph.HE].

Lin, Lin et al. (Oct. 2020). "Fermi/GBM View of the 2019 and 2020 Burst Active Episodes of SGR J1935+2154". In: *ApJ* 902.2, L43, p. L43. DOI: 10.3847/2041-8213/abbefe. arXiv: 2010.02767 [astro-ph.HE].

Livingstone, Margaret A. et al. (Dec. 2009). "X-ray and Radio Timing of the Pulsar in 3C 58". In: *ApJ* 706.2, pp. 1163–1173. DOI: 10.1088/0004-637X/706/2/1163. arXiv: 0901.2119 [astro-ph.SR].

Lorimer, D. R. and M. Kramer (2004). *Handbook of Pulsar Astronomy*. Vol. 4.

Loru, S. et al. (Jan. 2021). "New high-frequency radio observations of the Cygnus Loop supernova remnant with the Italian radio telescopes". In: *MNRAS* 500.4, pp. 5177–5194. DOI: 10.1093/mnras/staa2868. arXiv: 2009.09948 [astro-ph.HE].

Lower, Marcus E. and Ryan M. Shannon (Mar. 2020). "Multi-band observations of Swift J1818.0-1607 with Parkes". In: *The Astronomer's Telegram* 13587, p. 1.

Lower, Marcus E. et al. (Mar. 2020a). "MeerKAT observation of the radio magnetar candidate Swift J1818.0-1607". In: *The Astronomer's Telegram* 13562, p. 1.

Lower, Marcus E. et al. (Apr. 2020b). "Spectropolarimetric properties of Swift J1818.0−1607: a 1.4 s radio magnetar". In: *ApJ, submitted (eprint: astro-ph.HE/2004.11522)*, arXiv:2004.11522, arXiv:2004.11522. arXiv: 2004.11522 [astro-ph.HE].

Luo, Jing et al. (Apr. 2021a). "PINT: A Modern Software Package for Pulsar Timing". In: *ApJ* 911.1, 45, p. 45. DOI: 10.3847/1538-4357/abe62f. arXiv: 2012.00074 [astro-ph.IM].

— (Apr. 2021b). "PINT: A Modern Software Package for Pulsar Timing". In: *ApJ* 911.1, 45, p. 45. DOI: 10.3847/1538-4357/abe62f. arXiv: 2012.00074 [astro-ph.IM].

Maan, Yogesh et al. (Oct. 2022). "GBT detection of bright 5 GHz radio bursts from SGR 1935+2154, coincident with X-ray and 600 MHz bursts". In: *The Astronomer's Telegram* 15697, p. 1.

Manchester, R. N. et al. (Apr. 2005). "The Australia Telescope National Facility Pulsar Catalogue". In: *AJ* 129, pp. 1993–2006. DOI: 10.1086/428488.

Masci, Frank J. et al. (Jan. 2019). "The Zwicky Transient Facility: Data Processing, Products, and Archive". In: *PASP* 131.995, p. 018003. DOI: 10.1088/1538-3873/aae8ac. arXiv: 1902.01872 [astro-ph.IM].

Mazets, E. P. et al. (Dec. 1979). "Observations of a flaring X-ray pulsar in Dorado". In: *Nature* 282, pp. 587–589.

Mazets, E. P. et al. (May 1982). "The 5 March 1979 event and the distinct class of short gamma bursts Are they of the same origin". In: *Ap&SS* 84, pp. 173–189.

McConnell, D. et al. (Nov. 2020). "The Rapid ASKAP Continuum Survey I: Design and first results". In: *Publ. Astron. Soc. Australia* 37, e048, e048. DOI: 10.1017/pasa.2020.41. arXiv: 2012.00747 [astro-ph.IM].

McLaughlin, M. A. et al. (Feb. 2006). "Transient radio bursts from rotating neutron stars". In: *Nature* 439, pp. 817–820. DOI: 10.1038/nature04440. eprint: arXiv:astro-ph/0511587.

Mereghetti, S., J. A. Pons, and A. Melatos (Oct. 2015). "Magnetars: Properties, Origin and Evolution". In: *Space Sci. Rev.* 191, pp. 315–338. DOI: 10.1007/s11214-015-0146-y. arXiv: 1503.06313 [astro-ph.HE].

Mereghetti, S. and L. Stella (Mar. 1995). "The very low mass X-ray binary pulsars: A new class of sources?" In: *ApJ* 442, pp. L17–L20.

Mereghetti, S. et al. (Aug. 2020). "INTEGRAL Discovery of a Burst with Associated Radio Emission from the Magnetar SGR 1935+2154". In: *ApJ* 898.2, L29, p. L29. DOI: 10.3847/2041-8213/aba2cf. arXiv: 2005.06335 [astro-ph.HE].

Mereghetti, S. et al. (Oct. 2021). "INTEGRAL Limits on Past High-energy Activity from FRB 20200120E in M81". In: *The Astrophysical Journal Letters* 921.1, p. L3. DOI: 10.3847/2041-8213/ac2ee7. URL: https://doi.org/10.3847/2041-8213/ac2ee7.

Mereghetti, S. et al. (Oct. 2022). "INTEGRAL detection of a burst from SGR J1935+2154". In: *GRB Coordinates Network* 32698, p. 1.

Murphy, Tara et al. (Oct. 2021). "The ASKAP Variables and Slow Transients (VAST) Pilot Survey". In: *Publ. Astron. Soc. Australia* 38, e054, e054. DOI: 10.1017/pasa.2021.44. arXiv: 2108.06039 [astro-ph.HE].

NASA High Energy Astrophysics Science Archive Research Center - HEASARC (Aug. 2014). *HEAsoft: Unified Release of FTOOLS and XANADU*. ascl: 1408.004.

Nice, D. et al. (Sept. 2015a). *Tempo: Pulsar timing data analysis*. ascl: 1509.002.

— (Sept. 2015b). *Tempo: Pulsar timing data analysis*. Astrophysics Source Code Library, record ascl:1509.002. ascl: 1509.002.

Olausen, S. A. and V. M. Kaspi (May 2014). "The McGill Magnetar Catalog". In: *ApJS* 212.1, 6, p. 6. DOI: 10.1088/0067-0049/212/1/6. arXiv: 1309.4167 [astro-ph.HE].

Pacini, F. (Nov. 1967). "Energy Emission from a Neutron Star". In: *Nature* 216, pp. 567–568. DOI: 10.1038/216567a0.

— (July 1968). "Rotating Neutron Stars, Pulsars and Supernova Remnants". In: *Nature* 219.5150, pp. 145–146. DOI: 10.1038/219145a0.

Page, Dany (Mar. 1995). "Surface Temperature of a Magnetized Neutron Star and Interpretation of the ROSAT Data. I. Dipolar Fields". In: *ApJ* 442, p. 273. DOI: 10.1086/175439. arXiv: astro-ph/9407015 [astro-ph].

Palmer, D. M. et al. (Apr. 2005). "A giant γ-ray flare from the magnetar SGR 1806 - 20". In: *Nature* 434, pp. 1107–1109. DOI: 10.1038/nature03525.

Palmer, David M. (Oct. 2022). "Multiple Bursts from SGR J1935+2154". In: *The Astronomer's Telegram* 15667, p. 1.

Pavlinsky, M. et al. (May 2022). "SRG/ART-XC all-sky X-ray survey: Catalog of sources detected during the first year". In: *A&A* 661, A38, A38. DOI: 10.1051/0004-6361/202141770. arXiv: 2107.05879 [astro-ph.HE].

Pearlman, Aaron B. and Chime/Frb Collaboration (Dec. 2022). "CHIME/FRB Detection of Another Bright Radio Burst from SGR 1935+2154". In: *The Astronomer's Telegram* 15792, p. 1.

Pechenick, K. R., C. Ftaclas, and J. M. Cohen (Nov. 1983). "Hot spots on neutron stars - The near-field gravitational lens". In: *ApJ* 274, pp. 846–857. DOI: 10.1086/161498.

Perna, Rosalba, Jeremy Heyl, and Lars Hernquist (June 2001). "X-Ray Emission from Middle-aged Pulsars". In: *ApJ* 553.2, pp. 809–813. DOI: 10.1086/320985. arXiv: astro-ph/0104470 [astro-ph].

Petroff, E., J. W. T. Hessels, and D. R. Lorimer (Dec. 2022). "Fast radio bursts at the dawn of the 2020s". In: *A&ARv* 30.1, 2, p. 2. DOI: 10.1007/s00159-022-00139-w. arXiv: 2107.10113 [astro-ph.HE].

Predehl, P. et al. (Mar. 2021). "The eROSITA X-ray telescope on SRG". In: *A&A* 647, A1, A1. DOI: 10.1051/0004-6361/202039313. arXiv: 2010.03477 [astro-ph.HE].

Rajwade, K. M. et al. (Feb. 2022). "Long term radio and X-ray evolution of the magnetar Swift J1818.0-1607". In: *arXiv e-prints*, arXiv:2202.07548, arXiv:2202.07548. arXiv: 2202.07548 [astro-ph.HE].

Ray, P. S. et al. (June 2011). "Precise γ-ray Timing and Radio Observations of 17 Fermi γ-ray Pulsars". In: *ApJS* 194.2, 17, p. 17. DOI: 10.1088/0067-0049/194/2/17. arXiv: 1011.2468 [astro-ph.HE].

Richards, D. W. and J. M. Comella (May 1969). "The Period of Pulsar NP 0532". In: *Nature* 222.5193, pp. 551–552. DOI: 10.1038/222551a0.

Ridnaia, A. et al. (Feb. 2021). "A peculiar hard X-ray counterpart of a Galactic fast radio burst". In: *Nature Astronomy*. DOI: 10.1038/s41550-020-01265-0. arXiv: 2005.11178 [astro-ph.HE].

Roming, P. W. A. et al. (Oct. 2005). "The Swift Ultra-Violet/Optical Telescope". In: *Space Science Reviews* 120, pp. 95–142. DOI: 10.1007/s11214-005-5095-4. eprint: arXiv:astro-ph/0507413.

Ronchi, Michele (Apr. 2024). "Population synthesis of Galactic pulsars with machine learning". In: *arXiv e-prints*, arXiv:2404.15953, arXiv:2404.15953. DOI: 10.48550/arXiv.2404.15953. arXiv: 2404.15953 [astro-ph.HE].

Rosen, S. R. et al. (May 2016). "The XMM-Newton serendipitous survey. VII. The third XMM-Newton serendipitous source catalogue". In: *A&A* 590, A1, A1.

Scargle, J. D. et al. (Feb. 2013). "Studies in Astronomical Time Series Analysis. VI. Bayesian Block Representations". In: *ApJ* 764, 167, p. 167.

Staelin, David H. and III Reifenstein Edward C. (Dec. 1968). "Pulsating Radio Sources near the Crab Nebula". In: *Science* 162.3861, pp. 1481–1483. DOI: 10.1126/science.162.3861.1481.

Stamatikos, M. et al. (Jan. 2014). "GRB 140705A: Swift detection of a short burst." In: *GRB Coordinates Network* 16520, p. 1.

Strüder, L. et al. (Jan. 2001). "The European Photon Imaging Camera on XMM-Newton: The pn-CCD camera". In: *A&A* 365, pp. L18–L26.

Sunyaev, R. et al. (Dec. 2021). "SRG X-ray orbital observatory. Its telescopes and first scientific results". In: *A&A* 656, A132, A132. DOI: 10.1051/0004-6361/202141179. arXiv: 2104.13267 [astro-ph.HE].

Tavani, M. et al. (Feb. 2021). "An X-ray burst from a magnetar enlightening the mechanism of fast radio bursts". In: *Nature Astronomy*. DOI: 10.1038/s41550-020-01276-x. arXiv: 2005.12164 [astro-ph.HE].

THE CASA TEAM et al. (Oct. 2022). "CASA, the Common Astronomy Software Applications for Radio Astronomy". In: *arXiv e-prints*, arXiv:2210.02276, arXiv:2210.02276. arXiv: 2210.02276 [astro-ph.IM].

Thompson, C. and A. M. Beloborodov (Nov. 2005). "High-Energy Emission from Magnetars". In: *ApJ* 634, pp. 565–569. DOI: 10.1086/432245. eprint: astro-ph/0408538.

Thompson, C. and R. C. Duncan (July 1995). "The soft gamma repeaters as very strongly magnetized neutron stars - I. Radiative mechanism for outbursts". In: *MNRAS* 275, pp. 255–300.

— (Dec. 1996). "The Soft Gamma Repeaters as Very Strongly Magnetized Neutron Stars. II. Quiescent Neutrino, X-Ray, and Alfven Wave Emission". In: *ApJ* 473, pp. 322–342.

Turner, M. J. L. et al. (Jan. 2001). "The European Photon Imaging Camera on XMM-Newton: The MOS cameras". In: *A&A* 365, pp. L27–L35.

Turolla, R. (2009). "Isolated Neutron Stars: The Challenge of Simplicity". In: *Neutron stars and pulsars*. Ed. by W. Becker. Vol. 357. Astrophysics and Space Science Proceedings. Springer Heidelberg, pp. 141–163. DOI: 10.1007/978-3-540-76965-1_7.

Turolla, R., S. Zane, and A. L. Watts (2015). "Magnetars: the physics behind observations. A review". In: *Reports on Progress in Physics* 78, p. 116901. URL: http://stacks.iop.org/0034-4885/78/i=11/a=116901.

Ubertini, P. et al. (2003). "IBIS: The Imager on-board INTEGRAL". In: *A&A* 411.1, pp. L131–L139. DOI: 10.1051/0004-6361:20031224. URL: https://doi.org/10.1051/0004-6361:20031224.

Urošević, Dejan (Sept. 2020). "Determining the evolutionary status of supernova remnants". In: *Nature Astronomy* 4, pp. 910–912. DOI: 10.1038/s41550-020-01228-5.

van Paradijs, J., R. E. Taam, and E. P. J. van den Heuvel (July 1995). "On the nature of the 'anomalous' 6-s X-ray pulsars". In: *A&A* 299, p. L41.

van Straten, W. and M. Bailes (Jan. 2011). "DSPSR: Digital Signal Processing Software for Pulsar Astronomy". In: *Publ. Astron. Soc. Australia* 28.1, pp. 1–14. DOI: 10.1071/AS10021. arXiv: 1008.3973 [astro-ph.IM].

Verner, D. A. et al. (July 1996). "Atomic Data for Astrophysics. II. New Analytic FITS for Photoionization Cross Sections of Atoms and Ions". In: *ApJ* 465, p. 487.

Vink, Jacco (Dec. 2012). "Supernova remnants: the X-ray perspective". In: *A&ARv* 20, 49, p. 49. DOI: 10.1007/s00159-011-0049-1. arXiv: 1112.0576 [astro-ph.HE].

Wadiasingh, Zorawar et al. (Feb. 2018). "Resonant Inverse Compton Scattering Spectra from Highly Magnetized Neutron Stars". In: *ApJ* 854.2, 98, p. 98. DOI: 10.3847/1538-4357/aaa460. arXiv: 1712.09643 [astro-ph.HE].

Webb, N. A. et al. (Sept. 2020). "The XMM-Newton serendipitous survey. IX. The fourth XMM-Newton serendipitous source catalogue". In: *A&A* 641, A136, A136. DOI: 10.1051/0004-6361/201937353. arXiv: 2007.02899 [astro-ph.HE].

Weisskopf, M. C. et al. (July 2000). "Chandra X-ray Observatory (CXO): overview". In: *X-Ray Optics, Instruments, and Missions III. Edited by Truemper, J. E. and Aschenbach, B. Proceedings of the SPIE. SPIE, Bellingham WA*. Vol. 4012. Society of Photo-Optical Instrumentation Engineers (SPIE) Conference Series, pp. 2–16.

Whitney, Alan et al. (Dec. 2010). "VLBI Data Interchange Format (VDIF)". In: *Sixth International VLBI Service for Geodesy and Astronomy. Proceedings from the 2010 General Meeting*. Ed. by R. Navarro et al., pp. 192–196.

Wilms, J., A. Allen, and R. McCray (Oct. 2000). "On the Absorption of X-Rays in the Interstellar Medium". In: *ApJ* 542, pp. 914–924.

Winkler, C. et al. (Nov. 2003). "The INTEGRAL mission". In: *A&A* 411, pp. L1–L6.

XMM-Newton Users Handbook (July 2023). Issue 2.21. European Space Agency. ESA: XMM-Newton SOC. URL: https://xmm-tools.cosmos.esa.int/external/xmm_user_support/documentation/uhb/.

Younes, G. et al. (Oct. 2017). "X-Ray and Radio Observations of the Magnetar SGR J1935+2154 during Its 2014, 2015, and 2016 Outbursts". In: *ApJ* 847, 85, p. 85.

Younes, G. et al. (Dec. 2022a). "GBM detection of a faint magnetar-like burst temporally coincident with a CHIME/FRB radio burst". In: *The Astronomer's Telegram* 15794, p. 1.

Younes, G. et al. (Mar. 2023). "Magnetar spin-down glitch clearing the way for FRB-like bursts and a pulsed radio episode". In: *Nature Astronomy* 7, pp. 339–350. DOI: 10.1038/s41550-022-01865-y. arXiv: 2210.11518 [astro-ph.HE].

Younes, George et al. (Dec. 2020). "NICER View of the 2020 Burst Storm and Persistent Emission of SGR 1935+2154". In: *ApJ* 904.2, L21, p. L21. DOI: 10.3847/2041-8213/abc94c. arXiv: 2009.07886 [astro-ph.HE].

Younes, George et al. (Oct. 2022b). "NICER detection of over 100 bursts and enhanced persistent emission from SGR 1935+2154". In: *The Astronomer's Telegram* 15674, p. 1.

Yuan, Weimin et al. (2022). "The Einstein probe mission". In: *Handbook of X-ray and Gamma-ray Astrophysics*. Springer, pp. 1–30.

Zhou, Ping et al. (Dec. 2020). "Revisiting the Distance, Environment, and Supernova Properties of SNR G57.2+0.8 that Hosts SGR 1935+2154". In: *ApJ* 905.2, 99, p. 99. DOI: 10.3847/1538-4357/abc34a. arXiv: 2005.03517 [astro-ph.HE].

Zhu, Weiwei et al. (Oct. 2020). "FAST detection of radio bursts and pulsed emission from SGR J1935+2154". In: *The Astronomer's Telegram* 14084, p. 1.